Glacier - climate modeling in Las Leñas, Central Andes of Argentina

Master's Thesis

Faculty of Science

University of Bern

presented by

Philippe Wäger

2009

Supervisor:

Prof. Dr. Heinz Veit
Institute of Geography and Oeschger Centre for Climate Change Research

Advisor:

Dr. Christoph Kull
Institute of Geography and Organ consultatif sur les changements climatiques OcCC

Abstract

Studies investigating late Pleistocene glaciations in the Chilean Lake District (~40-43°S) and in Patagonia have been carried out for several decades and have led to a well established glacial chronology. Knowledge about the timing of late Pleistocene glaciations in the arid Central Andes (~15-30°S) and the mechanisms triggering them has also strongly increased in the past years, although it still remains limited compared to regions in the Northern Hemisphere. The Southern Central Andes between 31-40°S are only poorly investigated so far, which is mainly due to the remoteness of the formerly glaciated valleys and poor age control.

The present study is located in Las Leñas at 35°S, where late Pleistocene glaciation has left impressive and quite well preserved moraines. A glacier-climate model (Kull 1999) was applied to investigate the climate conditions that have triggered this local last glacial maximum (LLGM) advance. The model used was originally built to investigate glacio-climatological conditions in a summer precipitation regime, and all previous studies working with it were located in the arid Central Andes between ~17-30°S. Regarding the methodology applied, the present study has established the southernmost study site so far, and the first lying in midlatitudes with dominant and regular winter precipitation from the Westerlies. However, only slight adjustments turned out to be necessary to fit the model from Kull (1999) to a regular winter precipitation regime. The model reliably reproduced modern glacio-climatological conditions, and therefore, it was found to be also suitable to investigate paleo glacio-climatological conditions in the study area.

The modeling results are robust even when important input parameters are strongly varied. The theoretically possible climate conditions that could have triggered the advance range from extremely cold and dry to temperate and extremely humid. However, by evaluating the glacier geometry and by consulting reconstructed late Pleistocene climate conditions from other proxies in the region of the study area, a rather narrow range could be defined, delineating the most probable precipitation / temperature combinations. This range implies that the LLGM in Las Leñas was triggered in a cold-humid climate. For the scenario with best guess input parameters, the most probable climate conditions range from a temperature depression of 8°C in combination with a precipitation increase of 500mm, to a temperature depression of 5°C in combination with a precipitation increase of 1840mm.

From the modeling perspective, it can not be excluded that the precipitation increase could also have been caused by increased summer precipitation. However, all evidence, emerging from the exposition of the catchment, the glacier geometry and many proxies in Central Chile, points to intensified Westerlies causing more winter precipitation in the study area during late Pleistocene times.

The reconstructed cold-humid paleoclimate in this study points to an LLGM advance in Las Leñas during full glacial times, but ultimate constraints about the exact timing during the last glacial cycle are not possible. Still, an LLGM advance during Marine isotope stage 4 (MIS4, ~65 ka BP) is less probable due to the relative freshness of the moraines. Several periods during MIS2 (LGM) and MIS3 would fulfill both a strong temperature depression and humid conditions in Central Chile. However, the regional glacier chronologies available and especially the humid conditions reported for Central Chile provide more arguments for an advance prior to the LGM, around ~40-28 ka BP during MIS3, but this needs confirmation. The ^{10}Be surface exposure dates of the boulders, that were sampled during the field campaign in December 2008, will shortly be available and are expected to bring the timing issue forward.

A pre-LGM advance in Las Leñas would be in agreement with most of the few glacier chronologies available so far in the Southern Central Andes between 31-39°S, and would highlight the sensitivity of the late Pleistocene glaciers to precipitation changes.

Contents

List of Figures

List of Tables

Abbreviations

AAR	Accumulation area ratio
ACR	Antarctic cold reversal
AML	Arc macro language
asl	Above sea level
cal ka BP	Calibrated 1000 years before 1950
Co.	Cerro
db/dH	Mass balance gradient in the ablation area
DDF	Degree-day-factor
DJF	December, January, February
DEM	Digital elevation model
DOE	Daansgard-Oeschger events
dP	Precipitation change
dT	Temperature change
e.g.	for example (*lat. exempli gratia*)
ELA	Equilibrium line altitude
ELA_2500	Mapping scenario with the ELA at the MELM
ELA_3000	Mapping scenario with the ELA at 3000m asl
EN	El Niño
ENSO	El Niño Southern Oscillation
GCM	General circulation model
GHCN	Global Historical Climatology Network
GLCF	Global Land Cover Facility
GIS	Geographic information system
hPa	Hectopascal
i.e.	that means (*lat. id est*)
IGRA	Integrated global radiosonde archive
ISD	Interannual standard deviation
ITCZ	Inter-tropical convergence zone
JJA	June, July, August
ka BP	1000 years before 1950

kPa	Kilopascal
LGM	Last glacial maximum
LLGM	Local last glacial maximum
LN	La Niña
Ma	Million years
MAAT	Mean annual air temperature
MAM	March, April, May
MELM	Maximum elevation of lateral moraines
MEG	Median elevation of glaciers
MIS	Marine isotope stage
MODIS	Moderate resolution imaging spectroradiometer
MSWE	Maximum snow water equivalent
NCDC	National climatic data center
NISD	Normalized interannual standard deviation
NOAA	National oceanic and atmospheric administration
pELA	Paleo equilibrium line altitude
P_ELA	Precipitation at the equilibrium line altitude
PSI	Southern Patagonia icefield
SACZ	South Atlantic convergence zone
SALLJ	South American low-level jet
SASM	South American summer monsoon
SED	Surface exposure dating
SLP	Sea level pressure
SO	Southern Oscillation
SON	September, October, November
SPCZ	South Pacific convergence zone
SST	Sea surface temperatures
SWE	Snow water equivalent
T_ELA	Temperature at the equilibrium line altitude
THAR	Toe to headwall ratio
TM	Terminal moraine
TOA	Top of atmosphere
USGS	United States geological survey
Vn.	Volcano
WE	Water equivalent

1 Introduction and Motivation

The glacier-climate model from Kull (1999) was built to investigate modern and late Pleistocene glacio-climatological conditions in the subtropical arid Central Andes of South America. In the past ten years, it has been successfully applied to several locations between 17-30°S. The present study is located further south and applies Kull's model to a paleoglacier in Las Leñas (35°S), a ski resort in the Southern Central Andes of Argentina (Figure 1).

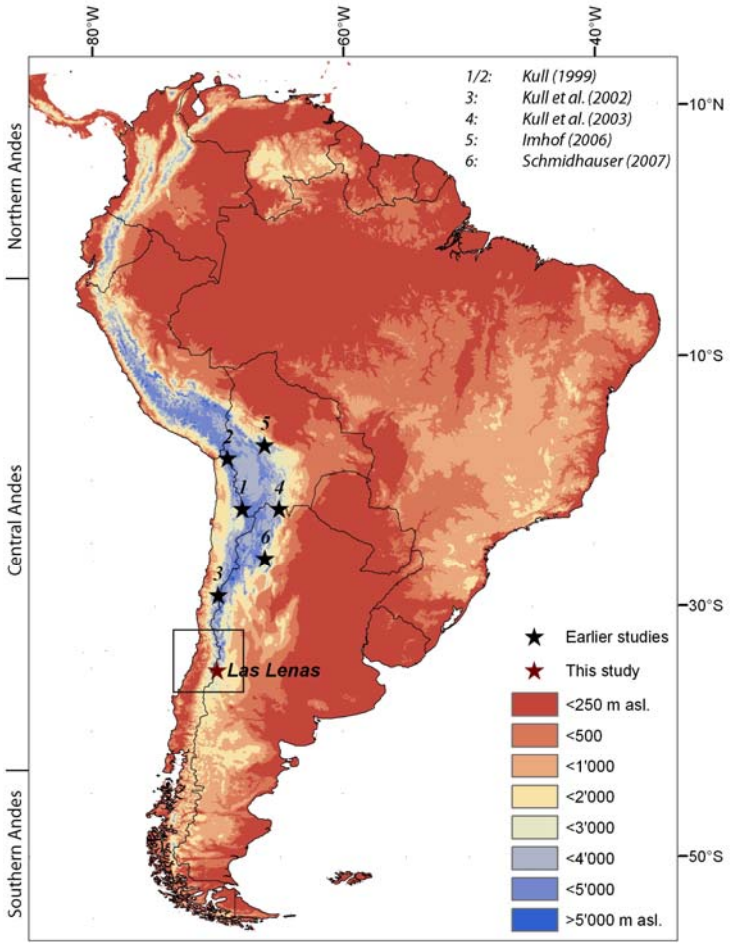

Figure 1: *Location of the present study (red star) and past studies (black stars and numbers). The classification into Northern, Central and Southern Andes bases on Orme (2007a). The black rectangle shows the extent of Figure 3.*

Originally, the glacier-climate model from Kull (1999, hereafter simply called glacier-climate model or model) was based on the assumption that an increase in precipitation during the late Pleistocene resulted from intensified convective summer precipitation. Furthermore, the mass balance terms in the model are calculated by empirical-statistical relationships that were established in regions of the arid Central Andes where summer precipitation prevails.

Nevertheless, one study has already been carried out in Northern Chile (29-30°S), where modern climate is arid to semiarid and dominated by winter precipitation (Kull et al. 2002). There, the model turned out to be also suitable to be applied to the conditions in a winter precipitation regime. However, the location of the present study is considerably further south than the southernmost study so far. Las Leñas lies in a transition region from semiarid to humid climates, which is characterized by a strong meridional precipitation gradient.

This study aims at increasing knowledge about the climate conditions during the local last glacial maximum (LLGM) in Las Leñas. This is particularly interesting because only few glacier chronologies have been established in this region (chapter 2.4.2). Following Zech et al. (2008), it is hypothesized that the LLGM advance in Las Leñas occurred around 35 ka BP and was triggered by a humidity pulse from intensified Westerlies, and by generally low temperatures during the last glacial.

The principal **research questions** of the present study are

1. Does the glacier-climate model fit to reconstruct modern and late Pleistocene glacio-climatological conditions in the semiarid to humid winter precipitation dominated climate of Las Leñas? Are adaptations necessary, and are they possible at all?

2. If the model is found to be suitable: What were the climate conditions during the LLGM advance in Las Leñas? Was the advance temperature- or precipitation-driven? What is the difference to today's climate?

3. What are the paleoclimatic implications of the results? Do the reconstructed climatic conditions support an advance around ~35 ka BP? What are the implications regarding atmospheric circulation patterns?

The present study is structured as follows. After this introduction, the location and the (paleo)climate of the study area are presented. In chapter 3, the reader is given a glaciological background, before the methods used are outlined in chapter 4. The results are shown in chapter 5 and discussed in chapter 6. The conclusions and outlook (chapter 7) complete the present study. References and Appendices are provided in the chapters 8 and 9.

2 Location and climate of the study area

2.1 Location

The modern Andes extend over 8500km from 12°N - 56°S and vary in width from 250 - 750km. They are a superb example of a mountain chain raised by plate subduction (Figure 2). The massive uplift in the Andean orogenic system in the past 30Ma is the result of the collision of the South American continental plate which has - moving west at 25-35mm/a - overriden the Nazca oceanic plate as it subducts eastward into the Peru-Chile Trench at 50-85mm/a. Mountain building and magmatism are thus responding to a net convergence of ~75-120mm/a. However, the magnitude and timing of this subduction has varied from north to south and from east to west, leading to anomalies in the elevation and in the trend of the modern Andes (Orme 2007a). For paleogeoecological studies, it is important to approximately know uplift rates in the corresponding study area. Saillard et al. (2009) found a mean uplift rate of ~0.6-0.7 m/ka since MIS 17 (~690 ka BP) along the Andean margin in Chile (31°S). Assuming that the LLGM in the study area occurred in the late Pleistocene around 35 ka BP, the total uplift since then is minor and is not further considered in the present study.

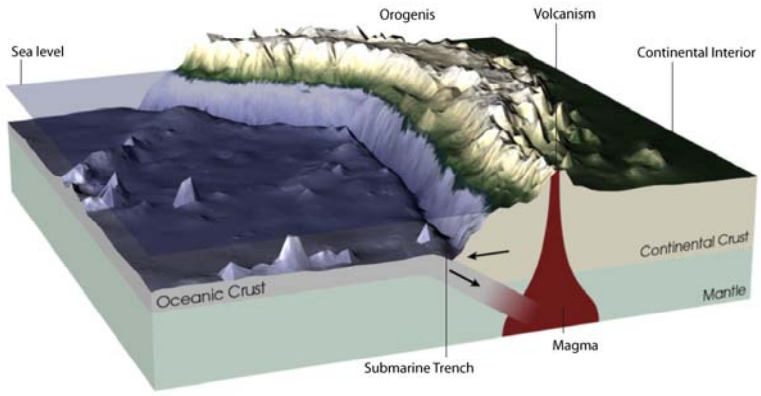

***Figure 2**: Schematic process of subduction. When an oceanic and a continental plate converge, the heavier oceanic plate is moved under the lighter continental one. Subduction is typically accompanied by the formation of a submarine trench, orogenis, and, if subduct angles are > ~25-30°, extensive volcanism. NASA Visible Earth picture, modified after Press & Siever (1995).*

According to Orme (2007a), the Andes can be structurally divided into three segments: The Northern, Central and Southern Andes (see also Figure 1). The Central Andes are further divided into the 2000km long Northern Central Andes, trending NW-SE from 5-18°S, and the 3200km long Southern Central Andes, trending N-S from 18-46°S. Las Leñas is located in the southern part of the Southern Central Andes at 35°S. Many peaks in the Southern Central Andes surpass 6000m asl, culminating in the Cerro Aconcagua (6959m asl) at 32°40'S. To the south, the maximum altitude of the mountain range decreases to 6000m asl at 33°40'S (at Cerro Marmolejo, the world's southernmost peak surpassing 6000m asl) and to only ~4000m asl at 35°S (see also Figure 15). The decreasing altitude of the Andes gradually allows the penetration of moist westerly winds from the Pacific, which influences precipitation patterns in the windward and leeward slopes of the Andes (see also chapter 2.2.2). Las Leñas lies on the leeward Argentinian slope at 35°S in the Province of Mendoza (Figure 3), about 30km east of the main ridge forming the national border with Chile.

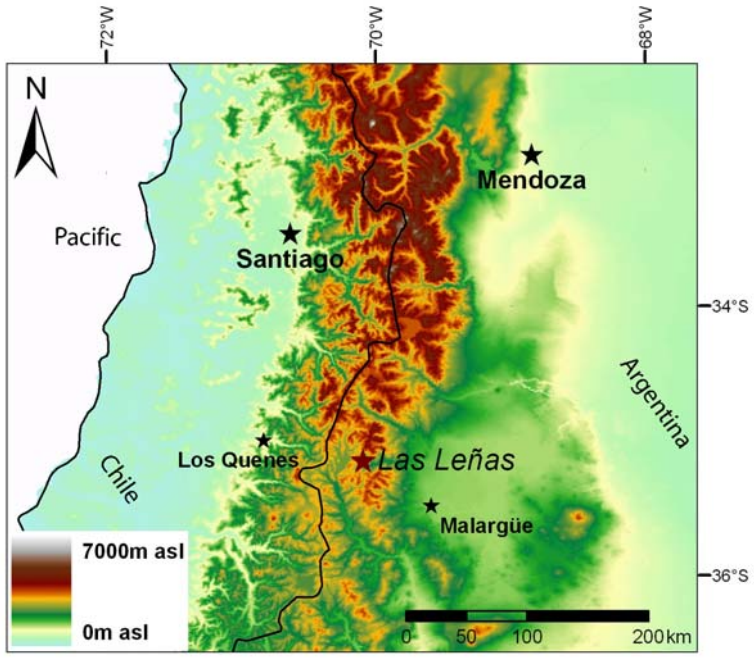

Figure 3: *Map of the Southern Central Andes between ~33 - 36°S with the location of the present study (red star). Las Leñas lies about 30km east of the main ridge forming the Chile-Argentina border (black line) and 70km northwest of Malargüe at 35°S.*

There is evidence for a massive former glaciation in Las Leñas mainly indicated by huge lateral moraines coming out from a today unglaciated valley which reaches up to altitudes of almost 3800m asl (Figure 4). Before 1983, when the ski resort was built, no modern infrastructure existed in the whole valley. Today, Las Leñas boasts more than 3000 beds (http://www.laslenas.com, Access

25.9.2009). The construction of hotels, streets, skilifts and ski pistes has changed the landscape and thereby also altered the geomorphologic evidence for the glaciation. There are tracks running on both lateral moraines, and parts of the left lateral moraine have been removed, which makes the mapping of the maximum former extent more complicate. In the whole valley, the impressive moraines are a rare feature. Only a few km northeast of Las Leñas, around Co. Las Leñas, another pair of lateral moraines is preserved at an altitude of 2600-2900m asl. In addition, cirques indicate that the topmost elevations of smaller and lower catchments were also formerly glaciated.

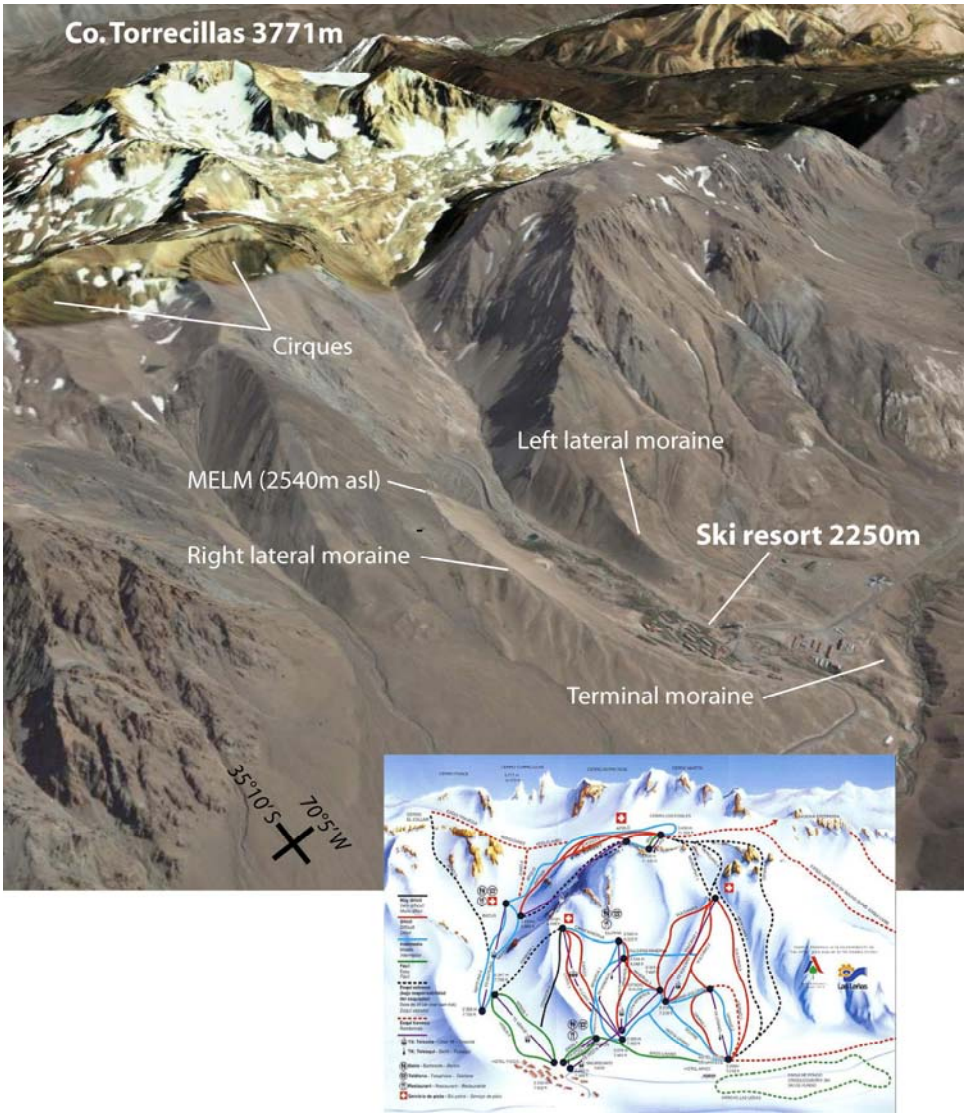

Figure 4: *Google Earth composite terrain picture of the study area and the ski slope plan of Las Leñas. The lateral moraines and end moraines indicate a massive former glaciation. The lateral moraines are even recognizable on the ski slope plan. The maximum elevation of lateral moraines (MELM) is at only 2540m asl. The lateral moraines point to a single catchment.*

2.2 Modern climate

First, an overview of South American climate is given, focusing on precipitation patterns and their intraseasonal and interannual variability (chapter 2.2.1). The large scale patterns are discussed on a more regional scale for the Central Andes (chapter 2.2.2), where also the precipitation regime in Las Leñas is characterized.

2.2.1 South America

Due to its location, meridional and latitudinal extent, topography and exposure to different atmospheric circulation systems, South America exhibits a large variety of climates (Figure 5), ranging from equatorial fully humid to desert and polar tundra climate (Kottek et al. 2006). Three quarters of the continent lie within (sub-)tropical latitudes and within the influence of the Inter-tropical convergence zone (ITCZ) and related circulation systems. Due to the location of the Andes close to the western edge of South America, the bulk of this area is influenced by the Atlantic, and only a narrow coastal area by the Pacific. In contrast to the very wet conditions due to deep convection over Amazonia, very arid conditions prevail from near the Equator to beyond the Tropic of Capricorn. The southernmost part of the continent is characterized by a narrow windward coastal strip and a leeward semidesert in the Andean rainshadow (Orme 2007b).

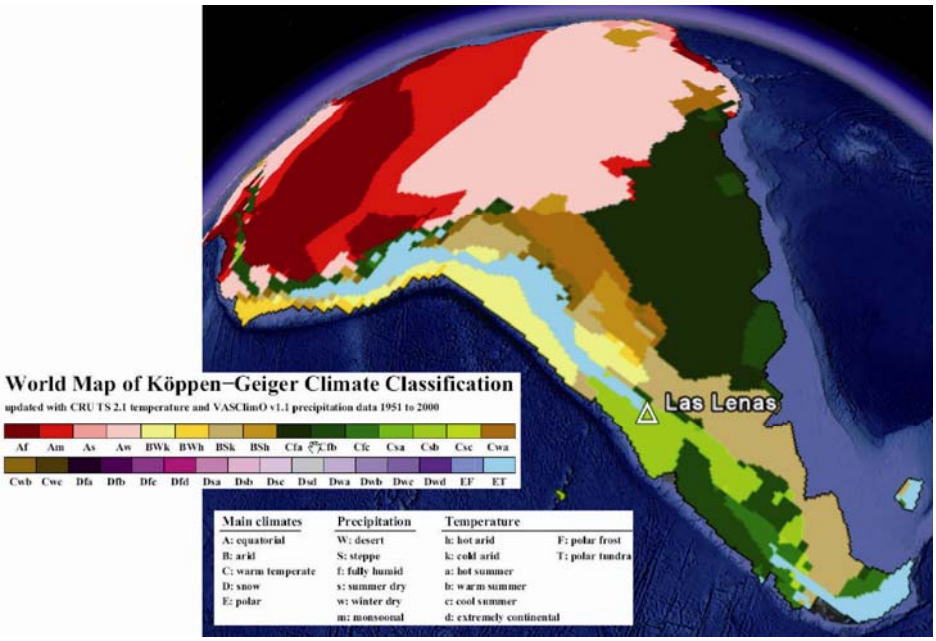

Figure 5: *Google Earth picture from South America with the Köppen-Geiger climate classification overlying (Kottek et al. 2006), showing the large variety of climates on the continent.*

2.2.1.1 Atmospheric circulation and precipitation

Annual mean precipitation, sea-level-pressure (SLP) and low-level winds over South America are shown in Figure 6. Three regions with evidently high precipitation can be distinguished. The ITCZ on the northern part of the continent (1) is a major feature of the global circulation, and its year-round position slightly north of the equator is ultimately related to the global land-sea distribution and orientation of the coastlines. Rainfall in the ITCZ is produced by deep moist convection. Over the continent, rainfall amounts are lower than over the ocean, but still high enough to sustain the largest rainforest in the world in the Amazon basin. The ascent over the ITCZ, the upper-level poleward flow, the subsidence in the subtropics and the low-level trade winds together form the Hadley Cell. Rainfall over the Central part of the continent is also abundant along the South Atlantic Convergence Zone (SACZ) (2). The SACZ is a local maximum in cloudiness and precipitation, occuring in a NW-SE oriented band from SE-Brazil to the South Atlantic, and results from the convergence of the Northeasterlies and the midlatitude Westerlies. The extratropical frontal systems from the westerly belt (3) produce precipitation in the South Pacific Convergence Zone (SPCZ) along the Western margin of the continent south of ~30°S (Garreaud & Aceituno 2007).

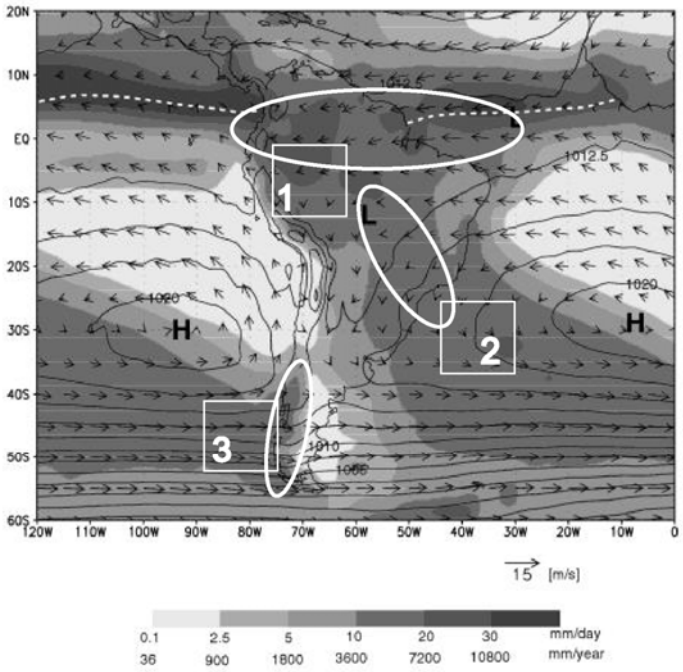

Figure 6: *Annual mean rainfall over South America. Also SLP (contour intervals 2.5hPa) and low-level winds with the annual mean position of the ITCZ (dashed white line) and approximate centers of the subtropical anticyclones (H) and continental low (L) are shown. The numbers 1-3 refer to the regions with high precipitation described in the text. After Garreaud & Aceituno (2007).*

2.2.1.2 Interseasonal variability of precipitation

There are strong interseasonal differences in precipitation on the continent. Seasonal rainfall and upper-level (200hPa) winds are shown in Figure 7 for austral winter (a), spring (b), summer (c) and autumn (d). The area around the ITCZ affected by deep convection changes significantly during the year, leading to strong seasonality in rainfall over the tropics and subtropics. In winter, when the ITCZ is at its northernmost position, precipitation is most abundant over northern South America, whereas the central part of the continent experiences its dry season. In spring, there is a rapid shift of the area of intense convection into the central Amazon basin, which drives the South American summer monsoon (SASM). In summer, convective precipitation reaches its southernmost position, and the so-called Bolivian High becomes established, leading to a convergence region along the coast of Peru and Ecuador and contributing to the summer intensification of the SACZ. Furthermore, a low pressure cell usually forms over the hot and dry Chaco region, which forces the trade winds to a southward flow. When deep convection diminishes over the subtropics by around the end of April, also the SASM collapses. South of ~40°S, precipitation from the Westerly belt prevails year-round. In winter (a), consistent with the equatorward displacement of the maximum tropical-extratropical thermal gradient, the Westerlies move northwards bringing precipitation up to ~30°S (Garreaud & Aceituno 2007).

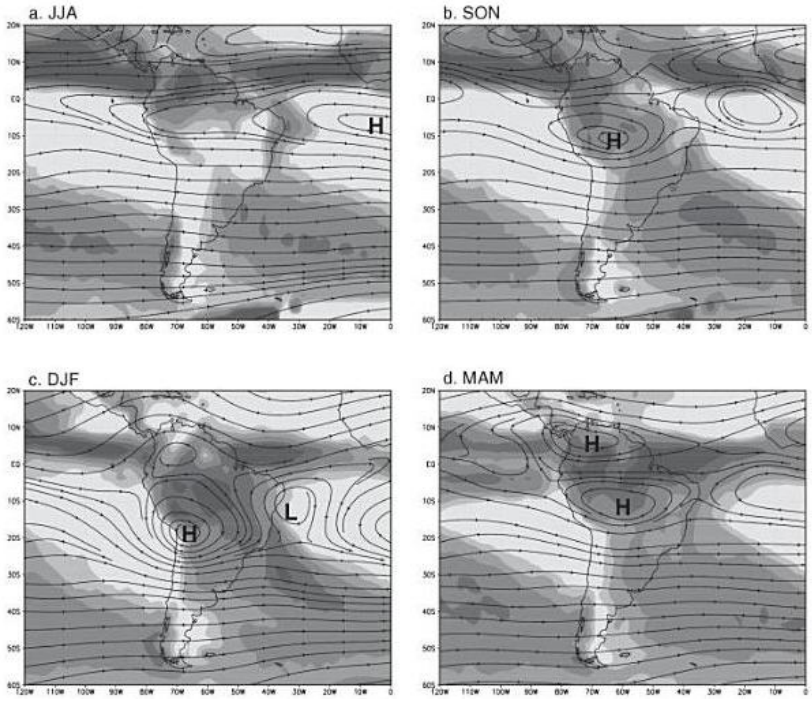

Figure 7: *Seasonal mean rainfall (shading scale as Figure 6) and 200 hPa winds over South America for austral winter (a), spring (b), summer (c) and autumn (d) with approximate centers of upper level anticyclones (H) and the upper level trough over NE Brazil (L) (Garreaud & Aceituno 2007).*

2.2.1.3 Interannual variability of precipitation

Interannual variability of precipitation in South America is strongly linked to the occurrences of El Niño (EN) and La Niña (LN) phenomena during the extreme phases of the Southern Oscillation (SO). The negative phase of the SO typically produces positive sea surface temperatures (SST) in the tropical pacific, while cold conditions prevail during the positive phase of the SO. When strong SST anomalies prevail for several months, an episode of EN (pos. SST, neg. SO) or LN (neg. SST, pos. SO) is defined. The sign and strength of the related anomalies depend on the region and the season, and strongest rainfall anomalies tend to occur during the regional wet seasons (Garreaud & Aceituno 2007). Figure 8 shows the main areas with El Niño Southern Oscillation (ENSO) related changes in rainfall.

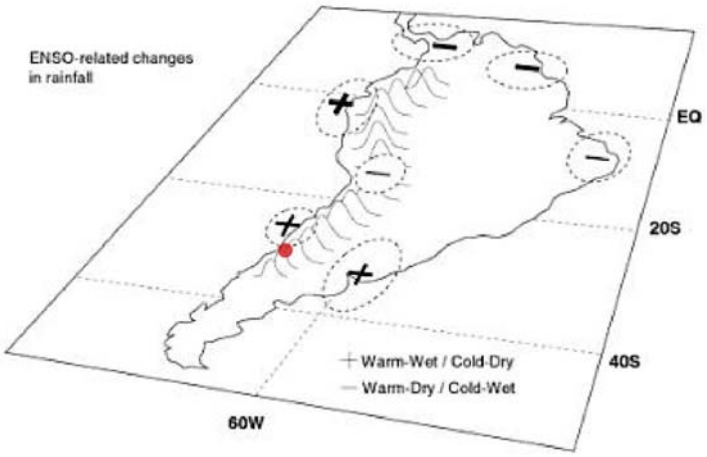

Figure 8: *Main areas with ENSO-related changes in rainfall, approximately outlined by dashed lines. The correlation between tropical pacific SST and rainfall anomalies is indicated by + and – signs, thickness indicates the relative strength of the correlation (Garreaud & Aceituno 2007). Red dot: Las Leñas.*

EN episodes are typically associated with negative precipitation anomalies along tropical South America, and with positive precipitation anomalies in the southeastern part of the continent and Central Chile. During LN events, opposite anomalies are observed in both regions (Garreaud et al. 2008). The tendency for positive precipitation anomalies in Central Chile is significant between 33 – 39°S. On the western side of the Altiplano, a weak tendency for negative precipitation anomalies during the wet season is documented. However, one has to keep in mind that the relationships between ENSO and regional rainfall and temperature are obtained from a short period of data records (~40a). The strength of these relationships might vary considerably on longer timescales (Garreaud & Aceituno 2007).

2.2.2 Central Andes

2.2.2.1 Atmospheric circulation and precipitation

The Central Andes mark a transition zone between tropical circulation in the north and extratropical circulation in the south (e.g. Kull et al. 2008). Total annual precipitation over southern South America is shown in Figure 9. The tropical circulation is responsible for precipitation in austral summer on the eastern slope of the Central Andes. Being channelled between the Andes and the Brazilian Plateau, the northerly flow often exhibits a low-level jet structure (SALLJ) (Saulo et al. 2000, Marengo et al. 2004) with its core at about 1km asl. The transported moisture feeds summertime convective storms as far south as 35°S. The westerly belt brings precipitation on the western margin of the Andes south of 30°S. (Garreaud et al. 2008). The humid western margin south of ~40°S is evident as well as the arid conditions on the Western margin north of ~30°S.

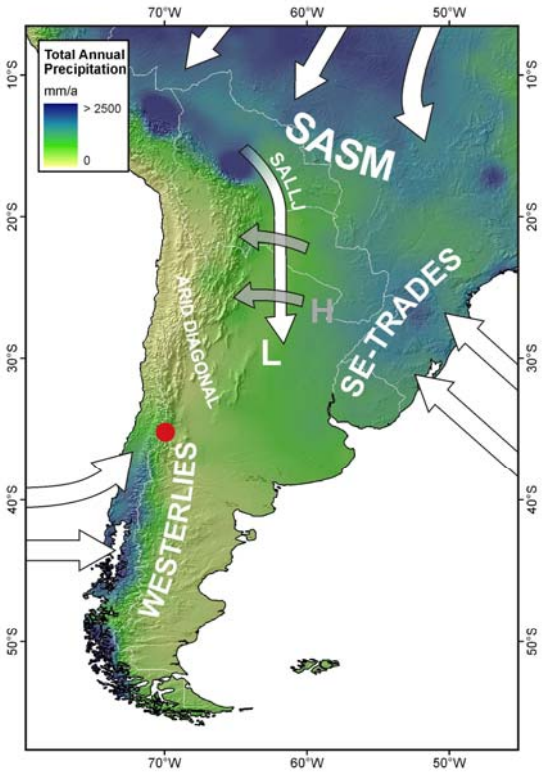

Figure 9: *Total annual precipitation in southern South America with the main wind flow directions responsible for the transport of humidity. The L stands for the summer Chaco Low, the H for the Bolivian High and the red dot indicates the location of Las Leñas. Precipitation data from New et al. (2002). Figure courtesy of J.-H. May.*

Precipitation over southern South America exhibits a strong zonal asymmetry, with very wet conditions to the west and very dry conditions to the east of the Andes. Between 18-29°S, the so-called Arid Diagonal crosses the Andes from NW to SE (Figure 9), tracing the rain shadow of the high mountain ridges to the prevailing airflow. Its core of maximal aridity is located between ~25-27°S, where modern annual precipitation is only ~100mm (Ammann et al. 2001). The hyper-aridity of the Peruvian and Atacama deserts results from the combined presence of the Humboldt Current, bringing cold Antarctic waters northward along the west coast, and the high Andean Cordillera to the East. The cold surface water temperatures pull moisture out of air masses before they reach land, while the high mountains separate the coastal area from any influence of the subtropical convective events. In addition, onshore winds from the Humboldt Current meet a strong zone of atmospheric subsidence formed by the stable South Pacific Anticyclone, producing a temperature inversion along the coast. The result is a mild and uniform climatic zone and the formation of thick stratus clouds, especially in winter, extending up to ~1000m asl (Figure 10). This fog produces the only moisture inputs along the coastal area, determining the extent of faunal and floral elements below its upper limit (Rundel et al. 2007).

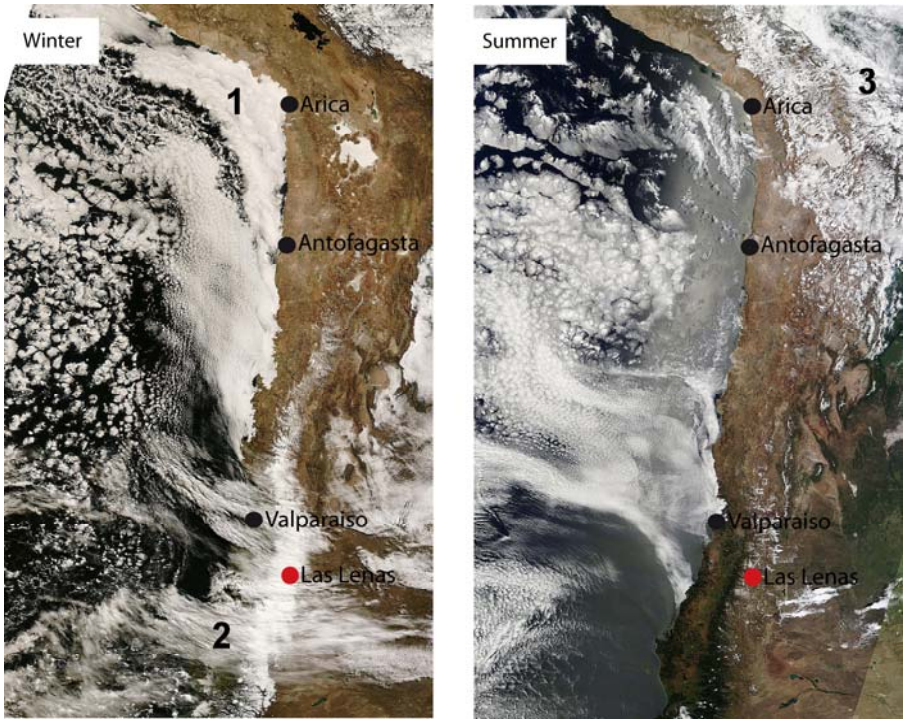

Figure 10: *Characteristic seasonal weather patterns over southern South America as seen in MODIS satellite pictures. (Left) The winter picture (31.12.2008), showing (1) extensive stratus and fog off the Peruvian and Atacama deserts, (2) the passage of cold fronts from Westerlies around the region of Las Leñas, and extensive snow cover in high altitudes. (Right) The summer picture (19.7.2008), with (3) scattered clouds on the Altiplano and the Western Cordillera, and general low snow cover.*

2.2.2.2 Intraseasonal variability of precipitation

Simplified seasonal circulation patterns and different air masses around the Central Andes at the latitudes of the Altiplano are shown in Figure 11. In wet austral summer (top), the moisture is transported from the Amazonian Lowlands to the eastern slope of the Central Andes, where it is forced to rise. In dry austral winter (bottom), westerly flow prevails (Garreaud et al. 2003).

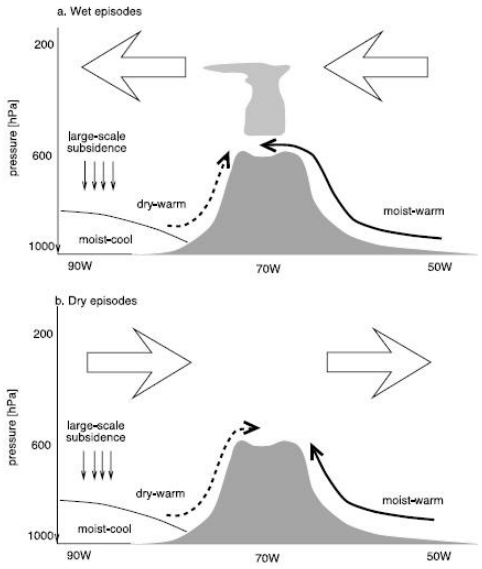

Figure 11: *Schematic representation of the circulation patterns and different air masses around the Central Andes in a vertical-longitude section at the latitudes of the Altiplano in (a) rainy summer and (b) dry winter episodes. Large open arrows indicate the sense of the upper-level large-scale flow. Solid (dashed) curves represent the transport of moist (dry) air by the regional circulation over the Andean slopes. Thin vertical arrows represent the large-scale subsidence over the subtropical SE Pacific that maintains the strong trade inversion (solid line) (Garreaud et al. 2003).*

Seasonality of the tracks and intensity of the Southern Westerlies is controlled by the strength and altitudinal position of the subtropical anticyclone in the Southeast Pacific and the circum-Antarctic low pressure belt. During austral winter (Figure 12 right), the jet stream of the Westerly belt moves into subtropical latitudes, and the related rainfall reaches a northern limit of ~30°S (Garreaud et al. 2008). Further north, up to about 27°S, only occasional winter rain events occur caused by mid-latitude storm tracks reaching very far north (Vuille & Ammann 1997). During austral spring, the core of the Westerlies moves 5-10° poleward to reach its southernmost position in austral summer (Figure 12 left) (Stuut et al. 2006). South of 40°S, low-level westerly flow prevails year round (Garreaud et al. 2008).

Figure 12: *Simplified sketch of seasonal latitudinal shifts of the Southern Westerlies. Average precipitation values are given for austral summer (DJF) and winter (JJA) (Stuut et al. 2006). Red dot: Las Leñas.*

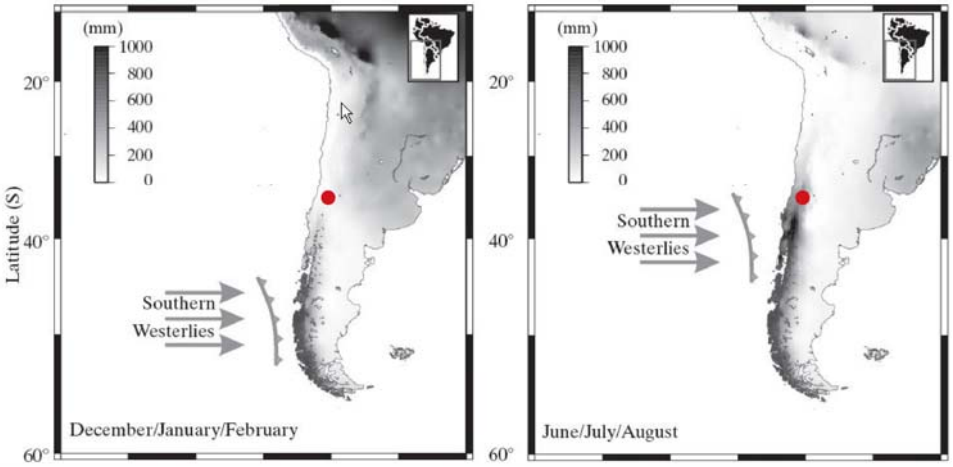

2.2.2.3 Interannual variability of precipitation

Interannual variability of precipitation in Central Chile is strongly determined by the ENSO phenomenon (Figure 8). The tendency for positive precipitation anomalies in Central Chile is significant between 33 - 36°S in austral winter. From 36 - 39°S, the signal is strongest during spring. The normalized interannual standard deviation (NISD) of annual mean precipitation is shown for southern South America (Figure 13). The NISD values decrease with increasing annual mean precipitation from ~35% at 30°S to ~10% around 40°S (Garreaud et al. 2008). Masioskas et al. (2006) found that high snow accumulation in the Central Andes of Chile and Argentina from 1951-2005 was generally concurrent with El Niño events in the tropical Pacific, but only 5 of the 10 driest years coincided with La Niña events.

2.2.2.4 Characterization of the precipitation regime in Las Leñas

The analysis of local climate provides the climatic input parameters for the glacier-climate model and, hence, is an essential part of this work. The methodology is outlined in chapter 4.3, while the results are shown in chapter 5.2. Nevertheless, after showing continental and regional precipitation patterns, it is appropriate to also characterize the local precipitation regime in Las Leñas. Being located only ~30km east of the main Andean ridge at 35°S latitude, moisture reaching Las Leñas is generally advected from western directions, and its precipitation regime is best compared with the one in Central Chile. Central Chile from ~31 - 37°S has a mediterranean-type climate, with less than 5% of rainfall

during summer, and the region is characterized by a large meridional gradient of rainfall. Annual mean values at low elevations are ~200mm at 31°S and rise up to ~2000mm at 41°S. Because the moist Pacific air-masses are orographically lifted, annual mean precipitation is higher in the Andes than in low elevations at the same latitude. As a consequence, Central Chilean climatic zones experience a northward displacement in the mountains (Stuut et al. 2006). However, on the leeward slope of the Andes, where this study is located, precipitation quickly decreases leading to a strong longitudinal precipitation gradient. The meridional gradient of precipitation is an expression of the seasonality of precipitation, which, according to Valero-Garcés et al. (2005), changes most rapidly around 34°S. South of 34°S, winter precipitation is dominant and regular, while north of 34°S, it occurs episodically.

In summary, winter precipitation in Las Leñas must be lower than on the Chilean slope of the Andes at the same latitude, but eventually as high as at the Chilean coast at the same latitude. Due to the similarities to Central Chile, also the interannual variability in precipitation (mainly caused by ENSO) is strong in Las Leñas (Figure 13). On the other hand, it is probable that Las Leñas gets more convective summer precipitation from the NE than Central Chile, but summer precipitation is certainly lower than winter precipitation.

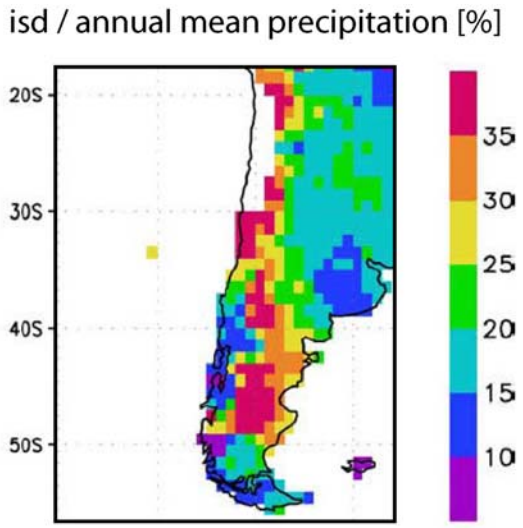

Figure 13: *Interannual standard deviation (ISD) normalized at the annual mean precipitation in southern South America. No values are shown where annual mean precipitation is below 50mm. Figure modified from Garreaud et al. (2008).*

2.3 Equilibrium line and snow line altitudes

The permanent snow line or equilibrium line altitude (ELA) is where accumulation equals ablation. As accumulation and ablation depend on climate, also the ELA does (chapter 3.1). In wet areas, the high accumulation depresses the altitude of the ELA (ELA < summer 0°C isotherm), in dry areas the ablation processes (sublimation) can compensate for low annual accumulation even above the 0°C level (ELA > summer 0°C isotherm) In South America, the ELA is just below the 0°C level in the wet inner tropics, approaches the summer 0°C isotherm with decreasing humidity towards the outer tropics, rises far above it in the extremely dry subtropics of southern Bolivia and Chile and drops far below it in the wet extratropical southern Andes (Kaser & Osmaston 2002) (Figure 14).

Figure 14: *The position of the ELA and the summer 0°C isotherm in a meridional section across the Andes (Kaser & Osmaston 2002).*

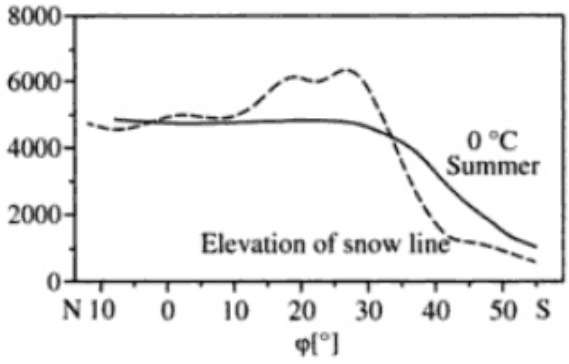

2.3.1 Central Andes between 27-36°S

Modern glaciers do not exist in the Andes of the Atacama desert between 18°S (Vn. Sajama) and 27°S (Co. Tres Cruzes) despite of elevations up to 6700m, which is clearly above the modern continuous permafrost belt (Messerli et al. 1993). This can be explained with the concept of thermal readiness (Messerli 1973), implying that glaciation can also be limited by insufficient precipitation, not only by too high temperatures. Indeed, the presence of isolated glaciers south of 27°S and the ELA depression from 5900m asl at 27°S to 5300m asl at 30°S is an expression of the southward increase of precipitation (Kull et al. 2002). A N-S profile of modern climate and glaciation in the Central Andes between 27 - 36°S from Brenning (2005) is shown in Figure 15. South of 27°S, glaciation increases as a result of meridional changes in precipitation and temperature, and the ELA decreases to ~5300m asl

at 30°S and to ~3200m at 35°S. At 35°S, the ELA meets the 0°C level. This is true for the Western range (ELA-W in Figure 15). An ELA in the Eastern range (ELA-E) only exists between ~30-34°S and is systematically higher for the Eastern compared to the Western range, which can be attributed to the longitudinal changes in precipitation. (Brenning 2005).

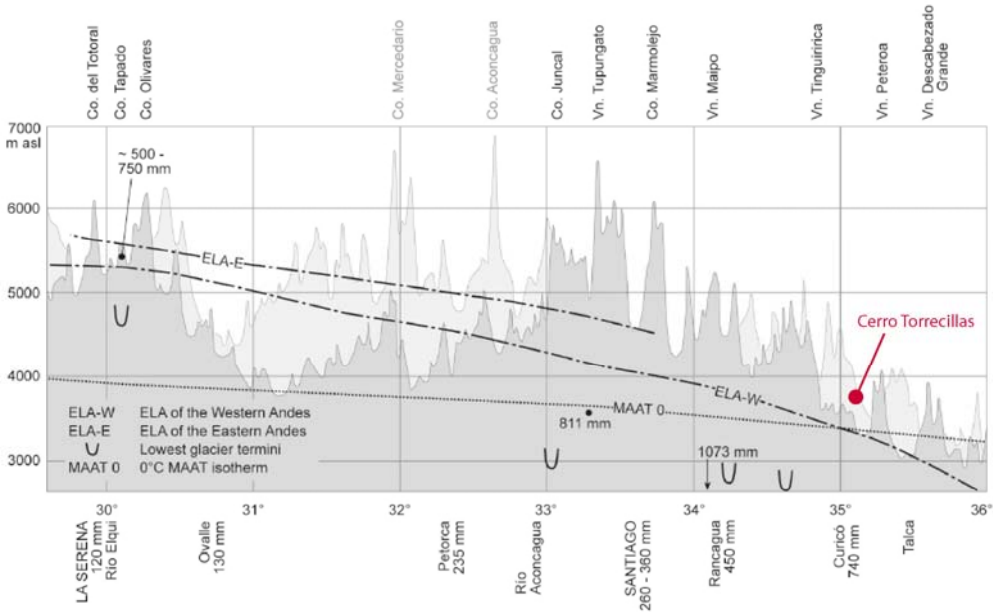

Figure 15: *A N-S profile of modern climate and glaciation in Central Chile as seen from the Pacific. The black and gray relief outlines represent maximum elevations in the Chilean and Argentinian Andes, respectively. Figure modified after Brenning (2005).*

2.3.2 Around Las Leñas

Las Leñas is located in the Eastern Andes at 35°S, where no ELA exists according to Figure 15. The ELA pattern in the region of the Central Andes between 34°35'S and 35°20'S is studied in more detail in Figure 16. In the Western range, the ELA is ~3350m asl at Glaciar El Penon and Azufre. It exhibits a distinct N-S gradient rising northwards up to ~3950m asl after only 60km. Interestingly, the ELA does not continue to rise from there on northward, but remains constant at ~3500-3800m asl for another 60km up to ~34°20, which is not indicated in Figure 15. However, the E-W gradient is even stronger. Despite of reaching approximately the same elevation as the Western range, only a few small glaciers exist in the Eastern range, which reflects the longitutinal precipitation gradients. At Co. Paraguay (~4500m), 18km NNE of Las Leñas, three small glaciers exist with ELAs at ~3950-4150m asl. Three glaciers are also found at Co. Risco Plateado (~5000m), 28km NNE of Las Leñas, with ELAs at ~3950-4300m asl.

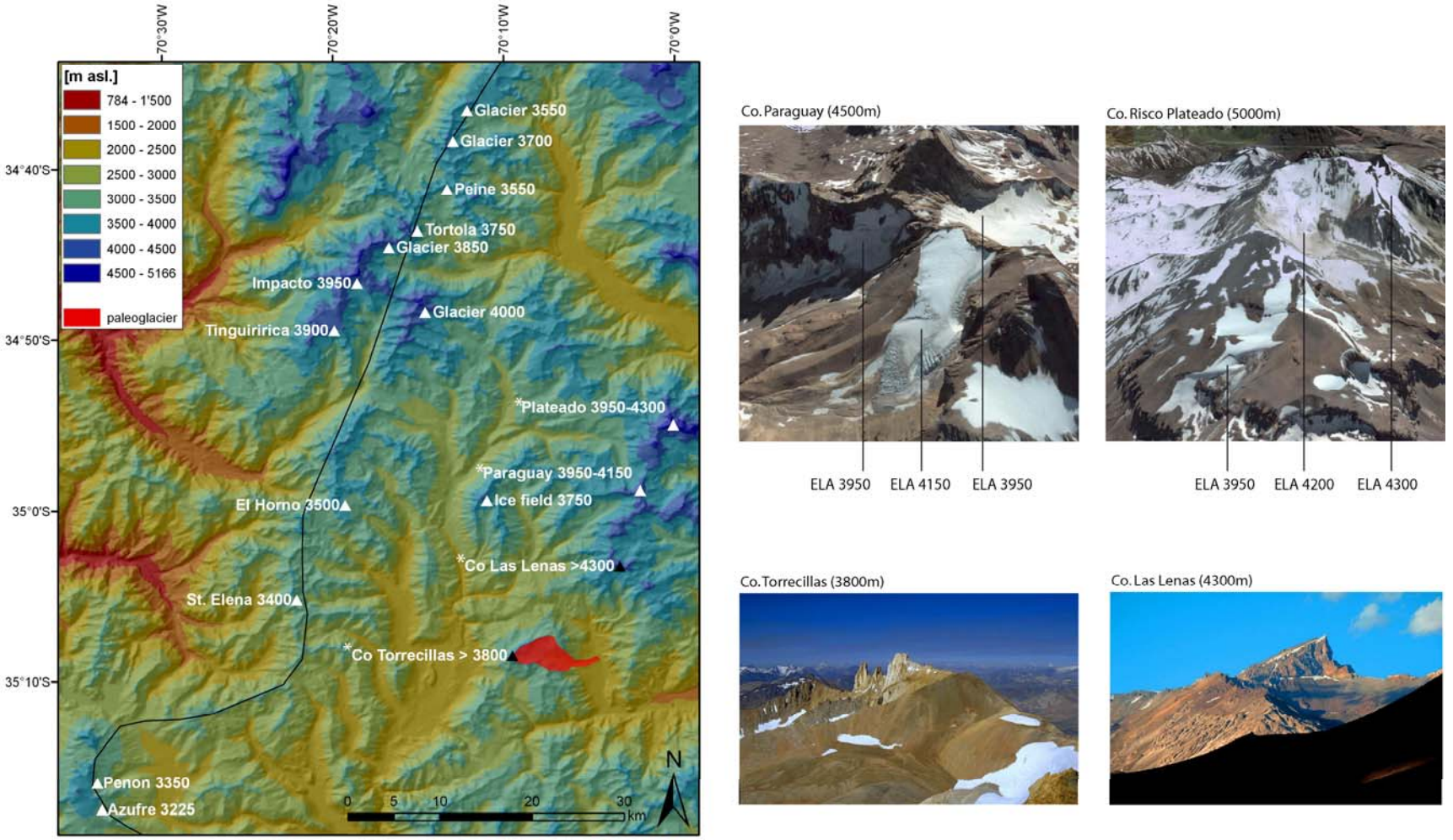

Figure 16: *Left: ELA pattern around the Chile-Argentina border (black line) in the surroundings of the study area. Red: the maximum extent of the studied paleoglacier. Modern glaciation is indicated with white triangles, named after the most prominent peak in the catchment and the corresponding local ELA [m asl]. Unglaciated Co. Torrecillas and Co. Las Leñas are indicated with black triangles. Peaks with a white asterisk are shown in more detail on the right. Right: Photos from Co. Torrecillas and Co. Las Leñas taken on 7.2.2002 (Brenneis 2002) and Google Earth pictures showing modern glaciers (and the corresponding ELA) on Co. Risco Plateado and Co. Paraguay.*

The catchments of all glaciers found in the Central Andes around the study area exhibit an east- to southward exposition. In addition, the catchments of the few glaciers existing in the Eastern range feature relatively steep bed slopes. Obviously, topography is crucial for the existence of modern glaciers around the study area.

First, topography determines local incoming shortwave radiation driving ablation directly (sublimation) and indirectly (melt) (see also chapter 4.1.2), and southward exposed catchments get least shortwave radiation. Second, topography defines the exposure of the terrain to the main wind direction. For the upper Atuel river basin (between 34°20' - 35°20'S), it has been reported that the eastern watershed (of the Western Andes) is more glaciated than the western one, which is due to the redeposition of snow from the action of winds predominantly from the southwest (Cobos & Boninsegna 1983). This is supported by the predominant expositions of the glaciers described above. The catchments that are most favourably for glaciation are southeastward exposed, benefiting from both low incoming shortwave radiation as well as from the redeposition of snow. Hence, the ELAs indicated in Figure 16 reflect local ELAs being only valid for the corresponding glaciation existing in a specific topographical setting.

For the modeling, it is important to approximately know the modern ELA in the study area. Being mainly east-exposed and shadowed especially in the mid part, also the topography of the catchment of Las Leñas paleoglacier would generally favour glacier formation. However, no modern glaciation is found in the catchment area of Las Leñas paleoglacier (maximum altitude ~3800m asl), and the whole Las Leñas valley (maximum altitude ~4300m asl) is currently ice-free. As can be seen in Figure 16, at beginning of February, there are a few small snow fields left around Cerro Torrecillas. The south slopes of Cerro Las Leñas, 11km NNE of Las Leñas, are almost snow-free. It has to be kept in mind (1) that beginning of February is not the end of the ablation season and (2) snow cover exhibits a strong interannual variability resulting from the interannual variability of winter precipitation.

Nevertheless, the occurrence of snowfields in February indicate that modern ELA is probably not much higher than the highest elevation of the catchment (~3800m asl). If also supposing e S-N gradient of ELA as found in the Western Andes, the ELA in the studied should not be higher than the ELA at Co. Risco Plateado and Co. Paraguay, who furthermore are located a bit more towards the east. Therefore the modern ELA in the study area can be expected to be at ~3900 - 4100m asl.

2.4 Late Pleistocene climate in the Central Andes

The marine isotope age 2 (MIS2) or Last glacial maximum (LGM) is generally accepted as representing the coldest part of the last glaciation (e.g. Suggate & Almond 2005). Mix et al. (2001) prefer a range for the LGM of 23-19 or 24-18 ka BP. MIS3 is a ~40 ka long period between the first (MIS4, ~65 ka BP) and the last (MIS2) maxima of the last glacial cycle. MIS3 was marked by fluctuating climate and large-scale deglaciation in Europe and Central Asia, intermixed with Heinrich and Dansgaard/Oeschger events (DOE) in the North Atlantic (Arnold et al. 2002). This chapter and the present study in general focuses on the time period of ~40 ka BP until the end of the Pleistocene at ~11 ka BP, when the Holocene started.

The Central Andes have become a key site for the study of climatic changes during late Pleistocene and Holocene times. The location between the tropical and extratropical circulation makes it ideal to study changes in large-scale atmospheric circulation patterns (e.g. Kull et al. 2002). While no modern glaciers exist between 18-27°S (chapter 2.3.1), moraines north and south of the Arid Diagonal (Figure 9) indicate increased precipitation in the late Pleistocene. Only in the core of the Arid diagonal (25-27°S), no glacial deposits have been found, and extreme limitations in humidity must have prevailed also during glacial times (Jenny & Kammer 1996).

Chronologies have shown that glaciers along a N-S transect from 15-40°S did not advance synchronously. As temperature changes are assumed to occur on a hemispheric or at least regional scale, different timings of the advances must reflect changes in precipitation (Zech et al. 2008).

Due to the lack of suitable organic material for ^{14}C dating, absolute age control on glacier chronologies in the Central Andes north of ~40°S has virtually been absent until the advent of surface exposure dating (SED) (Harrison 2004). In general, SED has helped to broaden knowledge about timing of late Pleistocene glaciations in the Central Andes, but methodological uncertainties mainly arising from the reference production rate of the cosmogenic nuclides can exceed 10% (Zech et al. resubmitted). Hence, there is a need for local calibration sites.

In this chapter, the late Pleistocene glacier chronologies established in several regions of the Central Andes between 17-31°S, and in the region of the present study, the Southern Central Andes between 31-43°S are reviewed. Dates are indicated in ka BP. If the literature provided ^{14}C dates, they were calibrated using an online calculator (Calpal 2007), and these dates are indicated in cal ka BP. The resulting paleoclimatic implications are discussed regarding the atmospheric circulation patterns, and the late Pleistocene climate conditions in the study area. Finally, the regional glacier chronologies are put in a global context.

2.4.1 Central Andes from 17 – 31°S

Western Cordillera (18 – 22°S)

The application of a glacier-climate model to paleoglaciers in Choquielimpie (~18°S) and El Tatio (~22°S) suggests strong humidity control (Kull & Grosjean 2000). A substantial increase in tropical summer precipitation and a moderate temperature depression of ~3-4°C was needed to allow the advances. The temperature depression is partly explained by increased cloud cover and thus related to the precipitation increase (Kull et al. 2002). These climate conditions are attributed to the Lateglacial. On the other hand, climate during LGM was probably too dry to allow substantial advances (Kull et al. 2008).

Eastern Cordillera (17 – 25°S)

Modeled glacio-climatological conditions in Cochabamba (17°S) indicate a strong temperature reduction (~6°C) and a slight precipitation increase during the LLGM in Valle Wara Wara (Imhof 2006). These conditions were first attributed to LGM times, but a recent SED study date the same extent to ~14 ka BP (Zech et al. resubmitted). Lateglacial advances (~11-13 ka BP) are also documented for nearby Valle Suturi, Valle Huara Loma and Valle San Francisco (Zech et al. 2007b). In these three valleys, however, Zech et al. (2007b) also dated advances during the LGM (22-25 ka BP), whose extents partly do not differ much from the lateglacial ones. This highlights the complex pattern of glacier chronologies in this region, which has also been recognized by Imhof (2006). The discrepancy to nearby SED studies reporting an early LLGM at ~34 ka BP and readvances at ~21 ka (Farber et al. 2005, Smith et al. 2005) is proposed to be caused by methodological uncertainties. By recalculating these ages using different scaling systems, Zech et al. (2007b) obtained ages of ~25-20 and ~13-11 ka BP, and therefore a regional quite homogeneous pattern. Provided that the scaling system used by Zech et al. (2007b) proves to be more accurate, the LLGM in these parts of Bolivia and Peru were temperature-sensitive and should have occurred roughly in-phase with the LGM. Evidence for advances during the LGM also arises from a modeling study in NW-Argentina (22°S), where a massive temperature reduction of ~4.5-8°C and enhanced precipitation have triggered the advances (Kull et al. 2003). Actually, SED from the same advance and advances in nearby Tres Lagunas point to a timing at ~22-25 ka BP (Zech et al. resubmitted). Kull et al. (2008) conclude that advances occurred during LGM and were temperature-driven where enough moisture was available. The lateglacial advances were triggered by a humidity pulse allowing the glaciers to advance despite of increasing temperatures. This is in agreement with paleosol-sequences along the Andean piedmont in Bolivian Chaco (~18°S) (May et al. 2008), indicating dry conditions with restricted pedogenesis before ~18 cal ka BP and wetter conditions in the Lateglacial.

Altiplanos and NW Argentina (20 – 26°S)

Glacier-climate modeling in the Sierra del Quilmes in NW-Argentina (~26°S) (Schmidhauser 2007) suggests a lateglacial advance triggered by substantial humidity enhancement. Indeed, a recent SED study (Zech et al. resubmitted) obtained ages of ~13 ka BP for the same advance and ages of ~25 (~LGM) and 34 ka BP (pre-LGM) for more extensive earlier ones. The lateglacial and pre-LGM advances are in agreement with the traditional assumption, that the Altiplano experienced massive wet phases, the Minchin phase (in pre-LGM) and the Tauca (Lateglacial) phases (Clapperton et al. 1997, Clayton & Clapperton 1997). However, there is no general agreement about the timing of these phases. Placzek et al. (2006) found three transgression phases in the Bolivian Basin at 18-22°S, Ouki (120-98 ka BP), Tauca (18-14 ka BP) and Coipasa (13-11 ka BP), but do not support the existence of the Minchin phase. Nevertheless, the lateglacial Tauca and Coipasa phases are evident in many archives, e.g. in stalagmites from southeast Brazil (Cruz et al. 2005), in lake sediments in Laguna Miscanti in northern Chile (Grosjean et al. 2001) or in lake level fluctuations in the Chilean Altiplano (Geyh et al. 1999). While Baker et al. (2001) propose a wet LGM from sediment cores from Lake Titicaca, others argue that the SASM was not strong enough to provide enough moisture because of a weakened tropical circulation (Placzek et al. 2006, Kull et al. 2008). Still, according to Placzek et al. (2006), climate during LGM was more humid than today, which allowed the LGM advances in the windward Eastern Cordilleras, but not in the leeward Altiplano. Zech et al. (2008) propose that the LLGM advances on the Bolivian Altiplano, NW Argentina and the Chilean plateau, but also in the Western Cordillera and Eastern Cordilleras, and even in northern Chile, were precipitation-driven and are correlated to the lake transgression phases on the Altiplano.

Northern Chile around ~30°S

Glacier climate modeling in the Encierro valley (29°S) suggests that a temperature reduction of 4-6°C in combination with an increase in precipitation by ~500mm was responsible for the most prominent LLGM advances. These conditions were tentatively attributed to the LGM (Kull et al. 2002), but a recent SED study (Zech et al. 2006) proposes a lateglacial timing (~14 ka BP). A bit further south in the Cordon de Doña Rosa (31°S), glacier advances were also dated to the Lateglacial (~14-11 ka BP) and, more extensive, to the pre-LGM (~39 ka BP) (Zech et al. 2007a). Zech et al. (2008) attribute the pre-LGM advances to increased winter precipitation, but propose that the lateglacial advances in this region were possibly synchronous with the lateglacial advances north of the Arid Diagonal and triggered by the same mechanisms, i.e. increased summer precipitation. Indeed, Kull et al. (2002) were not able to draw conclusions about the seasonality of precipitation during the LLGM in the Encierro valley.

2.4.2 Southern Central Andes from 31 – 43°S

Knowledge about the timing of the late Pleistocene glaciations in the region between ~31-40°S, where the present study is located, is very limited. This is mainly due to the remoteness of the formerly glaciated valleys and poor age control (e.g. Heusser 2003). In the Mendoza valley (~32°S) in Argentina, three late Pleistocene advances were recognized and named after their tills, the Penitentes, Horcones and Almacenes till. Minimum ages of ~24, ~23, ~38 ka BP (Espizua 1993) and ~31 ka BP (Espizua 1999) for the Penitentes and a minimum age of ~15 ka BP (Espizua 1999) for the Horcones advance could be obtained. It has been suggested that the Penitentes advance occurred prior to the LGM, the Horcones advance roughly in-line with the LGM, and the Almacenes advance during the Lateglacial (Espizua 2004).

In the Valle Rio Grande (34-35°S), very close to the location of the present study, a glacial chronology has been proposed with advances named Valle Hermoso I, II and III (Espizua 2004). However, direct minimum ages could only be obtained for the Hermoso II advance (~14 and ~16 ka BP). In addition, a nearby moraine was minimum-dated to ~10.5 ka BP and tentatively correlated to the Hermoso III advance. With respect to the present study, it is worth noting that this moraine, called Torrecillas, was produced by a glacier flowing northward of Co. Torrecillas, which is also the highest elevation of the eastward exposed catchment investigated in this study. This moraine could not be visited during fieldwork. Espizua (2004) speculated that the Hermoso I advance could be attributed to early Wisconsinan times (~MIS4), the Hermoso II advance to the global LGM, and the Hermoso III advance to lateglacial times, and that the Hermoso I, II and III advances could probably be correlated with the Penitentes, Almacenes and Horcones drifts in the Mendoza valley. In view of their proximity to the present study, two neoglacial advances shall also referred to. Espizua (2005) established a Holocene glacial chronology at the Baños del Azufre and Peñon. A minimum age of 4.4 ka BP was obtained for the most extensive neoglacial advance at glaciar el Peñon, where the ELA was depressed by ≤200m compared to today. However, Rodbell et al. (2009) adverts that without maximum-limiting age constraints, it is conceivable that these moraines were also deposited during the Lateglacial. Furthermore, a massive neoglacial advance at 4 ka BP in the Valle Atuel at Lago Sosneado, reaching down to ~2000m asl was proposed by Garleff & Stingl (1984). The corresponding ELA depression was ~600-800m compared to today. However, the location was revisited and the deposits were attributed to post-glacial volcanogenic debris slides (Gosse & Evenson 1994). This triggered a controversy (Garleff & Stingl 1994) which still persists (Grosjean et al. 2007). Provided that not only the mapped maximum extents, but also the datings of these two neoglacial advances are accurate, two very different kind of glaciations should have occurred during more or less the same time. Being only 70km NE of Glaciar El Peñon, the glaciation in the Valle Atuel, with a much bigger catchment, would

represent a massive advance producing terminal moraines at roughly the same elevation as the Hermoso I and II advance, which were attributed to MIS4 and MIS2 times (Espizua 2004).

For Laguna del Maule in Chile (36°S), there is evidence for an early LLGM with ice retreat starting between ~25.6-23.3 ka (Singer et al. 2000). ^{10}Be SED from the Valle Rucachoroi in Argentina (39°S) indicate an early LLGM at ~35ka BP, a deglaciation at ~15ka BP, and minor lateglacial readvances at ~12ka BP (Zech et al. 2008).

The Chilean Lake district (~40-43°S) is the northernmost region with a broad glacial geomorphology and enough organic material to allow extensive ^{14}C dating. Advances were dated to 25-23 and 19-14 cal ka BP at ~40°S by Bentley (1997), and to ~35, 31, 28, 25, 18 and 17 cal ka BP at ~41°S by Lowell et al. (1995). Denton et al. (1999b) propose that the most extensive advances in the Northern Chilean Lake district (~40-41.5°S) were probably reached in early LGM times at ~27 ka cal BP, but clearly later (~18 cal ka BP) in the Southern Chilean Lake district (~41.5-43°S). The maximum advances prior to the LGM suggest that the advances in the Northern Chilean Lake District were precipitation-driven. However, the Fundo Nueva Braunau (~40°S) pollen record indicates also colder temperatures after ~34 cal ka BP and very cold temperatures around ~27 cal ka BP (Heusser et al. 2000).

In a summary, Zech et al. (2008) propose that glaciers from ~30-40°S reached their LLGM extents around ~35-40 ka BP, and therefore before the global LGM. Because they are not synchronous with the lowest temperatures, these advances were sensitive to precipitation changes, which are attributed to changes in the westerly circulation. South of ~40°S, precipitation was high enough during LGM to permit the maximum advances during the temperature minimum.

2.4.3 Paleoclimatic implications

2.4.3.1 Tropical Easterlies

The lateglacial advances north and east of the Arid Diagonal, i.e. in the semiarid Eastern and Western Cordilleras, the Altiplanos and in NW-Argentina, were precipitation-driven, and the humidity pulse is attributed to an intensification of the tropical circulation (Zech et al. 2008). Kull et al. (2008, and references therein) give a résumé about the mechanisms that can lead to an intensification of the tropical circulation. They highlight the teleconnections to the Northern Hemisphere, a likely intensification and southward shift of the ITCZ bringing humidity to the Amazon basin, from where enhanced wind anomalies transport humidity to the Altiplano by a strong Bolivian High at a southward position. Indeed, humid conditions on the Altiplano during the Lateglacial are reported from many proxies (e.g. Clapperton et al. 1997, Clayton & Clapperton 1997, Geyh et al. 1999,

Grosjean et al. 2001, Placzek et al. 2006), and enhanced precipitation from the tropical circulation around 17-11 ka BP is also found in the Atacama desert (25°S) (Maldonado et al. 2005). Ammann et al. (2001) proposed that the timing of the late Pleistocene advances north and south of the Arid Diagonal might have been asynchronous, with the late Pleistocene glaciation south of ~27°S being influenced by past variations of the Westerlies. However, the documented lateglacial advances at ~30° roughly coincide with lake transgression phases on the Bolivian Altiplano. Zech et al. (2008) suggest that they were possibly synchronous with the glacial advances north of the Arid Diagonal and hence also a result of an intensification of the tropical circulation, which probably brought moisture further south during the Lateglacial. In fact, more humid conditions on the Chilean Altiplano have caused lake level highstands as far south as 28°S (Grosjean et al. 2001), and still today, the high mountain regions at the Andean divide at ~30°S are reached by summer precipitation as seen on the Co. Tapado (Kull et al. 2002). Obviously, in this region, a complex interplay of summer (tropical) and winter (extratropical) circulation was responsible for the lateglacial advances.

2.4.3.2 Extratropical Westerlies

The absence of LGM moraines in northern Chile around 30°S indicates that precipitation was limited at that time. Zech et al. (2008) suggest that the pre-LGM advances from 30-40°S were triggered by enhanced precipitation due to an intensification and/or northward shift of the westerly belt. Indeed, many proxies indicate humid conditions in Central Chile in late Pleistocene times, and partly also during the LGM (chapter 2.4.3.3). This signifies that the view of an LGM too dry to trigger glacial advances between 30°S and 40°S as proposed by Zech et al. (2008) is still controversial. The scientific debate on the latitudinal position and the intensity of the westerly belt during the LGM started already more than 20 years ago. Generally, two different hypothesis exist to explain increased moisture in Central Chile during the late Pleistocene, and they resulted from two different interpretations of palynological studies. To explain humid conditions as shown in his studies in Central Chile, Heusser (1983, 1990) proposed an equatorward shift of at least 5° and an intensification of the mid-latitude Southern Hemisphere Westerlies during the LGM and the Lateglacial. In contrast, Markgraf (1989) and Markgraf et al. (1992) postulated a poleward shift of the westerly belt and attributed the humid conditions to increased effective moisture due to lower temperatures. The debate was enriched in recent years by the application of general circulation models (GCMs) to investigate the role of the Westerlies during the late Pleistocene. The findings of Wyrwoll et al. (2000) and Valdes (2000) point to a general intensification and a zonal mean poleward displacement of the southern hemisphere LGM winter storm tracks. While the temperature cooling exhibits a consistent picture, the models show greater uncertainty for precipitation. The recent study by Rojas et al. (2009) found no definitive

latitudinal shift in westerly circulation, but increased winter storm activity in midlatitudes (25-45°S), and a general precipitation decrease south of 40°S.

Discussing the role of the Westerlies, it is interesting to note that the northern limit of late Pleistocene glaciation did not significantly exceed the present boundary at 27°S, which means that the northern boundary of the westerly belt did not shift towards lower latitudes. It has been proposed that it remained very stable in its current position, but was temporally intensified and exhibited much steeper meridional gradients (Wyrwoll et al. 2000, Kull et al. 2002).

2.4.3.3 Paleoclimate conditions in the broader study area

Temperature

The implication of the fossil pollen record at Laguna de Tagua Tagua (~34°S) is a summer cooling of at least 7°C during the LGM (Heusser 2003). However, the author also highlights that climate conditions between the Rio Maule and Valdivia (~36-40°S) might have been less restrictive. This region presents the highest number of arboral species and the largest number of endemics in Chile. Richness of species is believed to be the result of relatively stable Quaternary conditions, which are not supported by a 7°C drop in summer temperature as reconstructed at Tagua Tagua. ^{14}C dated pollen in the Northern Chilean Lake District (40°S) suggest a mean annual temperature depression of 6-7°C from ~24-18 cal ka BP (Moreno 1997). For the Chilean Lake District (40-43°S), Heusser (1999) found an LGM depression of summer temperatures by 6-8°C. For southern South America, the modeled LGM cooling is in the order of 8-10°C (Rojas et al. 2009).

The warming of the last termination (of >5°C) in the Chilean Lake district occurred at ~18-17 ka BP and the lateglacial cooling (of ≤3°C) at ~13-11.5 ka BP (e.g. Ariztegui et al. 1997, Heusser et al. 1999, Moreno et al. 1999, Moreno et al. 2001, Hajdas et al. 2003, De Batist et al. 2008).

If existing at all, regional temperature depressions reconstructed for pre-LGM times are not concise. Heusser (1999) found low temperatures for >~54 cal ka BP (possibly during MIS4), reported cold and humid conditions for MIS3 and a cooling after ~50 cal ka BP. Temperature reconstructions going further back than the LGM are mainly derived from the analysis of isotopic composition in ice cores in Antarctica or Greenland (Figure 17). In general, temperatures were low both in Greenland and Antarctica during the last glacial period from ~110-20 ka BP. The glacial climate in Greenland is characterized by a much higher amplitude of temperature due to the Daansgard-Oeschger events (DOE), which are rapid shifts from cold stadial to warmer interstadial conditions. It has long been unclear whether the DOE have counterparts in the Antarctic, however, the amplitude of the Antarctic warm events has recently be found to be dependent on the duration of the concurrent stadial in the

north (EPICA community members 2006). In Antarctica, the last glacial cycle exhibits much smaller amplitudes of temperature (~1-3°C) than the north. Temperatures were lowest during MIS2 (global LGM) and MIS4. Also MIS3 was generally low, but showed several of the described warm events occurring at ~35, 42, 50 and 58 ka BP (Blunier et al. 1998, Indermühle et al. 2000). After MIS2, temperature rose strongly until the Antarctic Cooling Reversal (ACR), whose cooling, however, was far from reaching the MIS2 level. Values from Antarctica and Greenland can certainly not be transferred to the Central Andes without adaptation. However, provided that these records should reflect global climate on both hemispheres, they allow to qualitatively assess the pre-LGM cooling in the Central Andes relative to the LGM. From Figure 17, we conclude that temperature depressions during MIS4 was comparable to MIS2, and that also MIS3 was cold, except for the interstadial conditions on both hemispheres triggered by the DOE in the north.

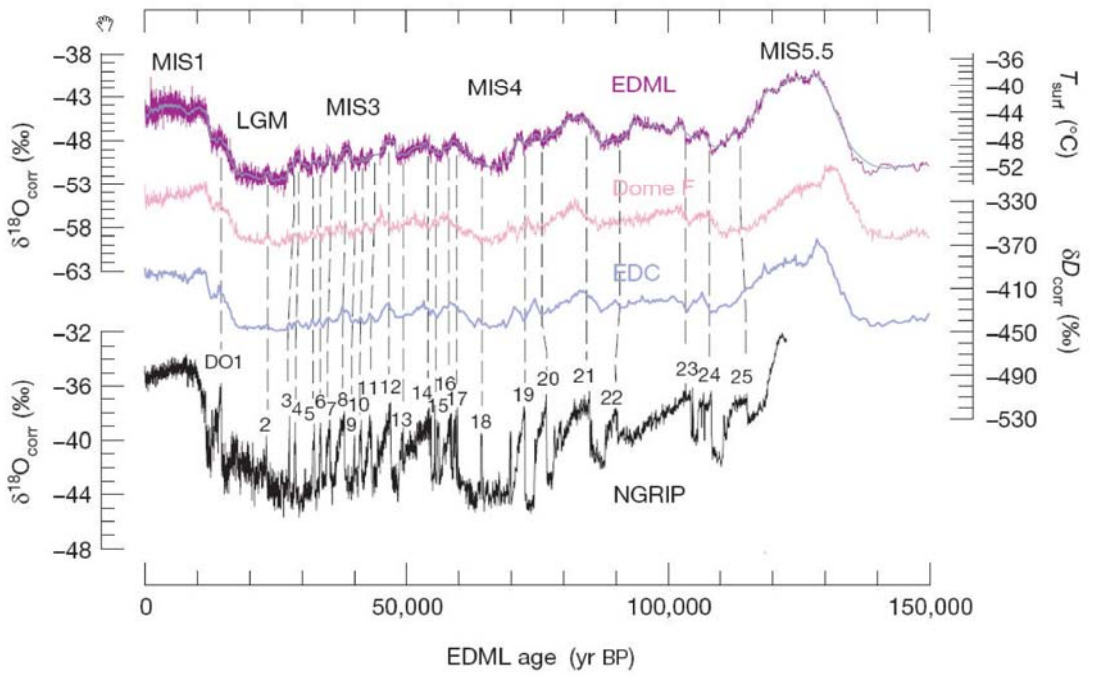

Figure 17: *The last glacial cycle as seen in isotope records from ice cores in the Antarctic and Greenland. The purple (EPICA community members 2006), pink (Watanabe et al. 2003) and blue (EPICA community members 2004) curve represent isotope records from the Antarctic, the black curve on the bottom is an isotope record from Greenland (North Greenland Ice Core Project members 2004). DOE as seen in the Greenland record are numbered and correlated with trends in the Antarctic. Figure modified after EPICA community members (2006).*

Precipitation and humidity

Several proxies in Central Chile point to generally increased humidity during glacial times. In the Southern Atacama desert (25°S), more winter precipitation is reported for >52, 40-33, 24-17 ka BP, more precipitation during both season from 17-14 ka BP and more summer precipitation from 14-11 ka BP (Maldonado et al. 2005). A deep-sea sediment core at 27°S offshore northern Chile shows humid conditions from 50-39 and 31-17 ka BP (culminating at 27 ka BP), but arid conditions from 39-31 ka BP (Stuut & Lamy 2004). Relict soils along the Chilean piedmont in the semi-arid Norte Chico (27-33°S) point to soil formation from 44-27 ka BP (Veit 2008). A marine core at 30°S in the Pacific off Chile suggests humid conditions from 33-19 ka BP and from 17-16 ka BP (Kaiser et al. 2008), and a core at 33°S (Lamy et al. 1999) point to generally cold-humid climates from 28-18 ka BP with a cold-semiarid interval between 26-22 ka BP. The implication of the fossil pollen record at Laguna de Tagua Tagua (~34°S) is an annual precipitation during the LGM about 1200mm greater than present, resulting in 2000mm at 200m asl (Heusser 2003). A more recent Laguna Tagua Tagua record points to a generally humid late Pleistocene from 40-21.5 ka BP, especially from 40-28 ka BP, and, to a lesser extent for 19.5-17 and 13.5-11.5 ka BP. These humid conditions were most probably not only caused by the reduced evaporation at lower temperatures, but by enhanced precipitation due to intensified Westerlies (Valero-Garcés et al. 2005). Further to the South, in the Northern Chilean Lake district at 40°S, Moreno et al. (1999) report twice the modern annual precipitation from ~24-16 cal ka BP. The LGM simulation of the Southern Westerlies in southern South America (Rojas et al. 2009) points to increased storm activity in winter in midlatitudes (25-45°S). In summary, there is a general agreement about humid conditions during the late Pleistocene, but the exact timings of humid phases differ among the studies. It is also important to note that the early and mid Holocene were the most arid periods in Central Chile in the last 46 ka BP (Valero-Garcés et al. 2005).

2.4.3.4 The global context

"Establishing leads and lags between the northern and southern hemispheres and between southern mid-latitudes and Antarctica is key to an appreciation of the mechanisms and resilience of global climate" (Sugden et al. 2005).

Glacier chronologies can provide information about paleoclimatic conditions during the advance phase. By comparing glacier advances in different regions, continents and on both Hemispheres, it is possible to investigate the triggers of the advances. Often, glacier chronologies are compared to the paleoclimatic reconstructions from deep ice cores drilled in polar regions. According to Sugden et al. (2005), the interplay between the Northern and the Southern Hemispheres are of particular interest. While some researchers suggest that the Antarctic pattern is typical for the Southern Hemisphere,

others believe that the Antarctic is isolated, with the rest of the Southern Hemisphere warming and cooling in synchrony with the Northern Hemisphere (Lynch-Stieglitz 2004).

As an example, glacier fluctuations in southernmost South America from 46-55°S are attributed to reflect a northern Hemisphere signal as they reached their LLGM at 25-23 ka BP (Sugden et al. 2005). From their datings at Lago Buenos Aires (46.5°S) indicating maximum extents in-line with the LGM, Douglass et al. (2006) pointed out that the chronology of the Patagonian Ice Cap is comparable to many records in the Northern Hemisphere. McCulloch et al. (2005) suppose a Northern Hemispheric signal for the LGM advances in the Magellan Strait (~53-55°S). According to Sugden et al. (2005), the implication is that climate during the LGM was generally synchronous at the global scale, and that at orbital time scales, the northern signal dominates any southern one.

On the other hand, Vandergoes et al. (2005) report from a pollen record in New Zealand (43°S) an early onset of cooling occurring well before MIS2. They highlight that local insolation variation in the mid-latitudes of the Southern Hemisphere is almost completely out of phase with insolation variation at the high northern latitudes. As a consequence, the authors conclude that global signals of climate change are modulated or even driven by local insolation effects in the south. Suggate & Almond (2005) also report an early onset of glaciation in New Zealand and refer to the Vostok ice core showing maximum cold from 26-18 ka BP (Petit et al. 1999). An early onset of glaciation in the Southern Hemisphere would also be in agreement with dates from the Northern Chilean Lake district (Denton et al. 1999a). Suggate & Almond (2005) also highlight that between ~34-18 ka BP, their glaciers investigated in New Zealand, but also the glaciers in the Northern Chilean Lake district, provided moraines that did not vary greatly in extent within each region.

An impressive example of hemispheric synchrony is reported for the last termination. A general near-synchronous interhemispheric termination of the LGM at ~17 ka BP in the midlatitudes of the Southern Hemisphere was suggested by Schaefer et al. (2006). At that time, no substantial warming was indicated in the isotopic record from Greenland, whereas isotopes implied that temperatures started to rise in Antarctica (Figure 18). The lateglacial advance (~14 ka BP) at Lago Buenos Aires described by Douglass et al. (2006), reaching 95% of the LGM extent, is supposed to be “distinctively Antarctic in nature”. This argument arises, because the timing is contemporaneous with the ACR, and precedes the Younger Dryas on the Northern Hemisphere. The existence of a Southern Hemisphere Lateglacial cold reversal preceding the Younger Dryas by ~500 years is also supported by other proxies in the region of the study area, e.g. the lacustrine record of Lago Puyelhue at 40°S (De Batist et al. 2008).

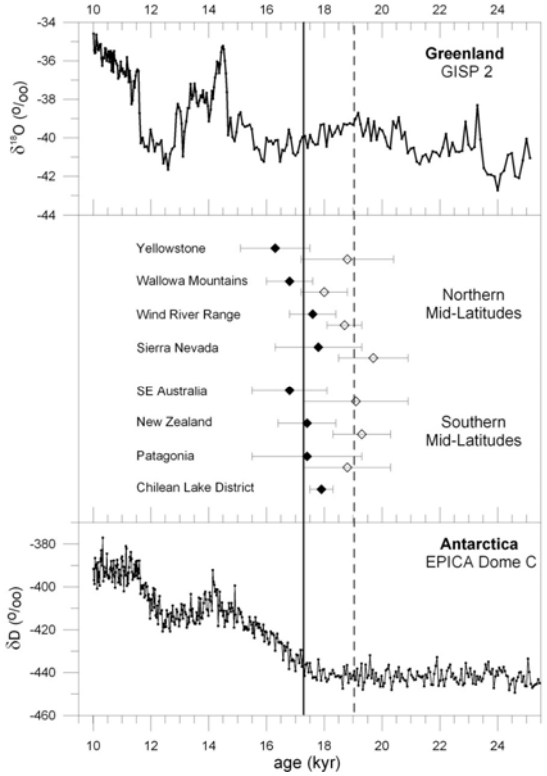

Figure 18: *Comparison of the onset of the midlatitude glacier LGM termination with polar ice core records. Plotted for each moraine record are (i) the mean age (solid diamonds) and (ii) the oldest ^{10}Be boulder age of each moraine set (open diamonds). The solid vertical line shows the mean of all individual mean ages, and the dotted vertical line the mean of all oldest ages (Schaefer et al. 2006, and references therein).*

Douglass et al. (2006) highlight climatic asynchrony across southern South America from the LGM to lateglacial times (23-14 ka BP). They found that the timing of maximum ice extent and onset of deglaciation at Lago Buenos Aires (46.5°S) occurred ~4 ka later than in the northern parts of the Chilean Lake District (~40-41.5S), but were synchronous with glacier advances or still stands in the Strait of Magellan (~52°S). The authors relate this regional asynchrony to the strength and position of the Southern Westerlies. Mc Culloch et al. (2000) suggested that a sudden rise in temperature at ~17.5-17.1 cal ka BP initiated deglaciation over 16° of latitude (~40 to 55°S) and that a second step of warming in the Chilean Lake District at ~15.7-15.4 cal ka BP let temperature rise close to modern values, hence highlighting regional synchronous behaviour. In a recent modeling study however, Rojas et al. (2009) found a climate boundary between the mid- and high-latitudes of the Southern Hemisphere at ~45°S to 50°S during the LGM. The authors speculated that this might reflect the Antarctic versus "a rest of the world" paleoclimate pattern during the LGM.

3 Glaciological background

In this chapter, the reader is given a glaciological background, which is necessary for understanding the glacier-climate model. First, glaciers and the most important terms are defined. The mass balance, ultimately controlling the existence of glaciers, is described in chapter 3.1 and glacier flow, powered by gravitational acceleration, in chapter 3.2. Finally, the possibilities for using glaciers as climate proxies are outlined (chapter 3.3). The content of this chapter bases on Häberli et al. (2005) if no further references are indicated.

Accumulation is the sum of all processes leading to a mass increase of the glacier, mainly precipitation (as snow), avalanches and snowdrift. Ablation on the other hand represents the sum of all processes leading to a mass decrease of the glacier, i.e. melt and run-off, sublimation, wind erosion or calving. The equilibrium line altitude (ELA), the sum of all points where accumulation equals ablation, separates the accumulation and the ablation area. A schematic glacier is shown in Figure 19.

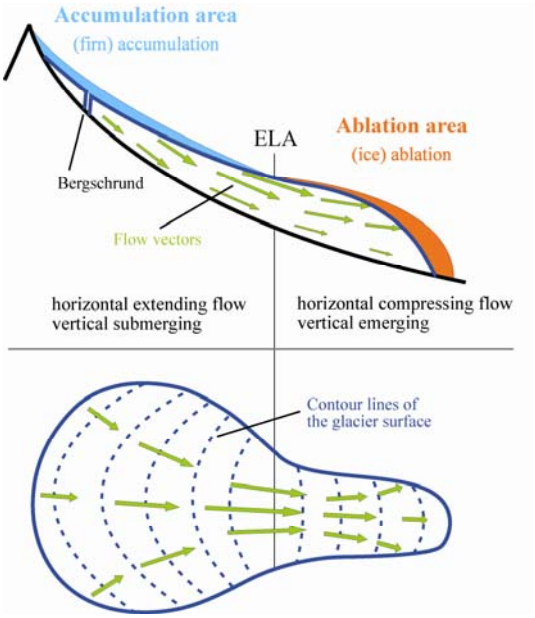

Figure 19: *Longitudinal section (top) and ground view (bottom) of a schematic glacier with the most important terms and ice flow vectors. Modified after Imhof (2006).*

3.1 Mass balance

Mass flow at the glacier surface is controlled by the energy flows between snow / firn / ice and the atmosphere. In their sum, these flows represent the energy balance, which controls the mass balance as well as the temperature of the glacier. During he time interval $t_i - t_0$, the specific mass balance *b* at any point of the glacier depends on the specific accumulation *c* and ablation *a*:

$$b = c + a = \int_{t_0}^{t_i} b \; dt \qquad \text{Equation 1}$$

$$c = \int_{t_0}^{t_i} c \; dt \qquad \text{Equation 2}$$

$$a = \int_{t_0}^{t_i} a \; dt \qquad \text{Equation 3}$$

By integrating all specific mass balances *b* over the whole glacier surface area *S*, the total mass balance *B* of a glacier is determined as

$$B = \int_{S} b \; dS \qquad \text{Equation 4}$$

Mass balance is the direct response of a glacier to the prevailing climate conditions. Therefore, it is of particular interest. Mass balance can approximatively be measured by the following methods:

1. The direct glaciological measurement bases on the measurement of the net balance at a representative set of point on the glacier by using ablation stakes and accumulation pits. The total mass balance of the glacier is interpolated from the single values.

2. With the photogrammetric method, the glacier surface is measured. The glacier area, thickness and volume changes are determined between different points in time.

3. With the hydrologic method, mass balance can be calculated as the left over when detracting runoff and sublimation from precipitation (mass balance = precipitation – runoff – sublimation).

4. Index methods: If the position of the ELA is known, the accumulation area ratio (AAR) can be calculated. A rule of thumb for glaciers in midlatitudes is that the AAR is ~0.67 in equilibrium state. However, the AAR results from the vertical glacier mass balance, which depends on climate. Cold and moderately dry climates produce long glacier tongues and low AAR values, while warm and humid climates produce short glacier tongues and high AAR values (Kaser & Georges 1999).

Obviously, these methods differ strongly in complexity, accuracy and also applicability. The first three methods are only possible on modern, still existing glaciers. On the other hand, the index method is also possible for paleoglaciers – if it is possible to determine the paleo equilibrium line altitude (pELA) (chapter 3.3). A glacier is in equilibrium (or steady) state if its total mass balance is zero. A mass surplus is converted by glacier flow (chapter 3.2) into length changes of the glacier.

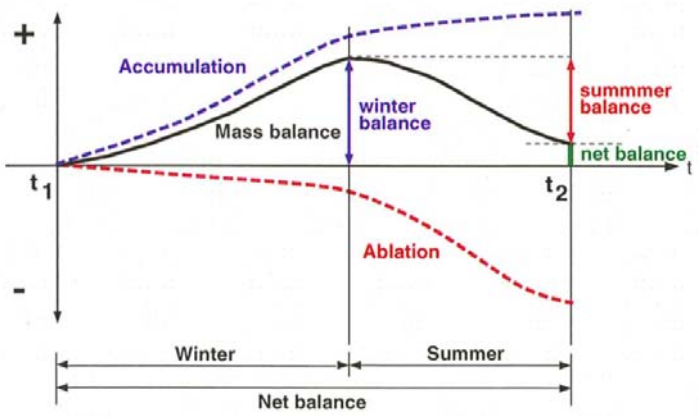

Figure 20: *Definition of (seasonal) mass balance terms for a given point on the glacier surface during one balance year. The net balance is the difference between summer and winter balance (Huss 2009).*

Mass balance exhibits a seasonality (Figure 20) following the seasonality of local climate. Annual mass balance corresponds to one balance year, starting with the accumulation season and ending with the end of the ablation season, usually with the first major snowfall. Mass balance depends on climate, and as climate conditions change with increasing altitude, also the mass balance does. With increasing altitude, temperature drops resulting in (1) less ablation by melt and (2) a higher fraction of snow at the total precipitation. Furthermore, precipitation often exhibits a positive lapse rate due to orographic uplift. The vertical mass balance gradient is defined as the variation of the specific mass balance with altitude (e.g. Kaser & Osmaston 2002). Vertical mass balance profiles show a decreasing negative net balance up to the ELA. The specific net balance is 0 at the ELA, and net balance is positive above the ELA.

The climate prevailing at the ELA is considered to be just sufficient to allow the existence of glaciers. Several studies have tried to characterize the climate at the ELA. Based on statistical analysis of a large dataset, Ohmura et al. (1992) established a polynominal regression function linking precipitation at the ELA to the mean summer temperature at the ELA. The cryosphere model from Häberli et al. (2005) shows a simplified relationship between the occurrence of glaciers (and permafrost, not further considered here) according to the climate conditions at the ELA (Figure 21). At the ELA, accumulation by snowfall meets ablation by melt, which is mainly driven by air temperature. Where precipitation (P) is high, e.g. in maritime climates, temperature (T) at the ELA is high, because high ablation rates by melt can be compensated with high accumulation rates. Where precipitation is low, e.g. in continental climates, temperature at the ELA is low, because the low ablation rates are already compensated by low accumulation rates. Mass turnover, expressed by the mass balance gradient in the ablation area (db/dH) is high in warm and humid climates and low in cold and dry climates. If changing climate conditions affect both temperature and precipitation, the cryosphere model must be adjusted in both vertical and horizontal directions. While sublimation in the alps is very limited, it can reach up to 70% of total ablation in the subtropics. Hence, the cryosphere model cannot be transferred to the subtropics without adaptation.

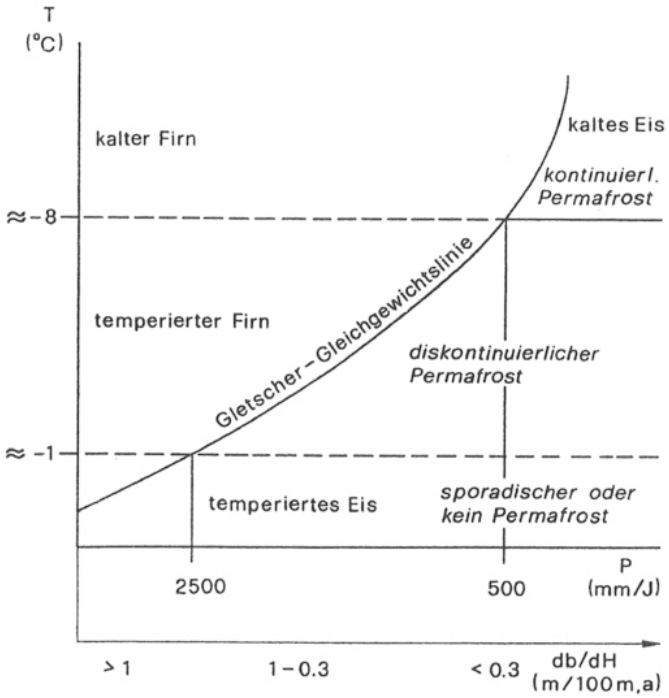

Figure 21: *A simple cryosphere model showing the relationship between climate conditions (precipitation P and temperature T at the ELA; mass balance gradient in the ablation area db/dH) and the occurrence of glaciers and permafrost (Häberli et al. 2005).*

3.2 Ice flow

The occurrence of ice below the ELA can only be explained by glacier flow transporting mass surplus from the accumulation to the ablation area (Figure 19). Ice deformation and basal sliding are the dominant flow processes. Morphologic features such as crevasses or moraines can only be understood with flow. For a glacier in equilibrium state (with total mass balance of 0), the flow Q through a cross section and the mean flow velocity u over the area F of a cross section is

$$Q = uF = \int_{H_a} bs \, dH = -\int_{H_b} bs \, dH \qquad \text{Equation 5}$$

with H_a and H_b = altitudinal areas above and below the cross section, b = specific mass balance and s = area fraction of the glacier. In flow direction, Q and u increase towards the ELA (extending flow) and decrease in the ablation area (compressing flow). These long profile deformations cause a compensation by cross contractions in the accumulation and cross extensions in the ablation area, expressed by convergence (accumulation) and divergence (ablation area) of the flow lines respectively. Therefore, transverse crevasses are mainly found in the accumulation area and longitudinal crevasses in the ablation area. The vertical flow components compensate accumulation (as submergence) and ablation (as emergence) (Figure 19). Total flow velocity at the glacier surface u_s is composed of basal flow velocity u_b and the flow velocity of internal deformation u_d:

$$u_s = u_b + u_d \qquad \text{Equation 6}$$

3.2.1 Internal Deformation

Under constant stress, the deformation velocity of ice is also constant. In Glen's flow law, which essentially is an empirical fit to laboratory and field data for the loading conditions and stresses encountered in glaciers (Paterson 1994), the deformation velocity $\dot{\varepsilon}$ is described as

$$\dot{\varepsilon} = A\sigma^n \qquad \text{Equation 7}$$

with σ = stress, A and n *(≈ 3)* = parameters of the flow law. The Parameter A depends on several factors (e.g. ice temperature, liquid water content, crystal orientation, impurity content), and its values found by different experimenters vary considerably (Paterson 1994). Paterson (1994) recommends

values for A at different temperatures (0°C to -50°C) and n = 3. His values decrease non-linearly by more than one order of magnitude when decreasing ice temperature from 0°C to -10°C.

Assuming that glaciers are not controlled by stress, but controlled by deformation resulting in a basal shear stress, equation 7 can be transformed and basal shear stress τ can be described as

$$\tau = \left[\frac{\dot{\varepsilon}}{A}\right]^{1/n} \quad \text{or} \qquad \text{Equation 8}$$

$$\tau = F\rho g H \sin\alpha, \qquad where\ H \sin\alpha \approx const. \qquad \text{Equation 9}$$

with F = shape factor reflecting lateral friction, ρ = ice density, g = acceleration of gravity, H = ice thickness and α = surface slope. F [values between 0 and 1] depends on the geometry of the channel.

Under the assumption of ideal plasticity where τ is constant, also H*sin α is constant. Hence, glaciers are thin in the steep parts and thick on flat terrain. τ is low for small and continental glaciers with low mass turnover, and high for large and maritime glaciers with high mass turnover. Typical τ values are ~50-100 kPa for alpine glaciers (with α = 5° and H = 100m) and ~100-150 kPa for ice sheets (with α = 0.5° and H = 2000m).

3.2.2 Basal Sliding

The occurrence of basal sliding depends on the ice temperatures at the glacier bed. The pressure of the overlying ice decreases the melting point of ice at the glacier bed. Only for temperate glaciers, the resulting ice temperatures at the glacier bed are around the pressure melting point, producing a thin melt water film. If only a few mm thick, this film already allows basal sliding. At cold glaciers, no water film is produced because ice temperatures at the glacier bed are below the pressure melting point. Hence, the glacier is frozen to its bed, and no basal sliding is possible. Basal sliding is more efficient the lower the friction at the glacier bed is. The thicker and closer the melt water film, the higher is the flow velocity of basal sliding. Hence, the flow velocity of basal sliding exhibits seasonal differences, with the highest values in summer, especially at noon. Heavy precipitation events (rain) can also influence basal sliding, whereas stone particles slowdown basal sliding by increasing friction (Winkler 2009). Due to limited melt water, u_b is almost negligible for cold glaciers. For temperate glaciers, the fraction of basal sliding to total flow velocity (u_b / u_s) varies considerably, but the long-

term and large-scale mean is ~0.5. For numerical modeling studies, basal flow velocity u_b is often described as

$$u_b = B\frac{\tau^m}{(P_i - P_w)^p}, \qquad \text{Equation 10}$$

with τ = basal shear stress, $P_i - P_w$ = difference between ice and water pressure and *B,m and p* = constants. However, it is difficult to measure the term $P_i - P_w$ for modern glaciers and obviously impossible for paleoglaciers. Hence, in the present study, a less sophisticated approach is used (chapter 4.1.3).

3.3 Glaciers as climate proxies

"Large parts of the earth's surface have been influenced by glaciers, and they still form polar regions and high mountain areas. Glaciers are dynamic, and climate controls their continuous changing. Hence, they are ideal proxies of climate change during the past and present" (Winkler 2009).

Glaciers and ice caps provide among the most visible indications of the effects of climate change. A change in climate will affect the magnitude of the accumulation and ablation terms and the length of the mass balance seasons (chapter 3.1). By glacier flow (chapter 3.2), the glacier will then change its extent towards a size that makes the total mass balance zero. However, climate variability and the time lag of the glacier response determine that a static equilibrium is never attained (Lemke et al. 2007). The time lag, the response time, depends on several factors such as the size of the glacier, ice flow velocity or surface gradients, and differs strongly among glaciers (Winkler 2009).

Records of recent glacier length changes go back to 1600 and contain the low-frequency climate change of the past centuries (WGMS(ICSI-IAHS) various years-a). Measurements of mass balance are few and started only to the mid-20th century (WGMS(ICSI-IAHS) various years-b). The major recent development in using glaciers or ice sheets as paleoclimate proxies has been the information obtained from ice cores from high mountain glaciers or polar ice sheets (Paterson 1994). In the topmost layers of these cores, annual accumulation layers are clearly recognizable and show interannual variability of precipitation. However, for deeper parts of the core, the individual layers are usually not apparent (Benn & Evans 1998). The isotopic composition of oxygen and hydrogen in the ice reflect the temperature at which condensation occurred in the past. In ice cores, the variation of isotopic concentration with depth can be interpreted as variations of temperature. Air bubbles in the ice contain

samples of the atmospheres at the time they were formed. The records of variations of greenhouse gases such as carbon dioxide (CO_2) or Methane (CH_4) are of particular interest (Benn & Evans 1998).

Also glaciers who do not exist any more under modern climate conditions can provide information about paleoclimate conditions – if they have left traces in the landscape (e.g. Benn & Evans 1998). Especially in arid climates, an only small humidity increase leads to significant changes of processes and forms associated to the water balance, soils and vegetation. In the arid Central Andes (18-29°S), these traces of former climates are well preserved due to the limited shaping power under modern climate conditions (Jenny & Kammer 1996). These traces allow a detailed reconstruction of the former glacier extents (Kull 1999).

Modeling studies that try to redraw observed recent glacier fluctuations are driven by (instrumentally) recorded or reconstructed climate data. Modeling studies trying to estimate future glacier behaviour work with projections of the future changes of climate parameters. The process chain of such studies is shown in Figure 22. When reconstructing paleoclimate conditions from observed glaciations, one has to proceed the other way round (Paterson 1994). Geomorphologic evidence of past glaciations was produced by fluctuations of glaciers. They are an expression of former mass balance changes (given the age of past glaciations, the response time is mostly neglected), who were driven by climate changes.

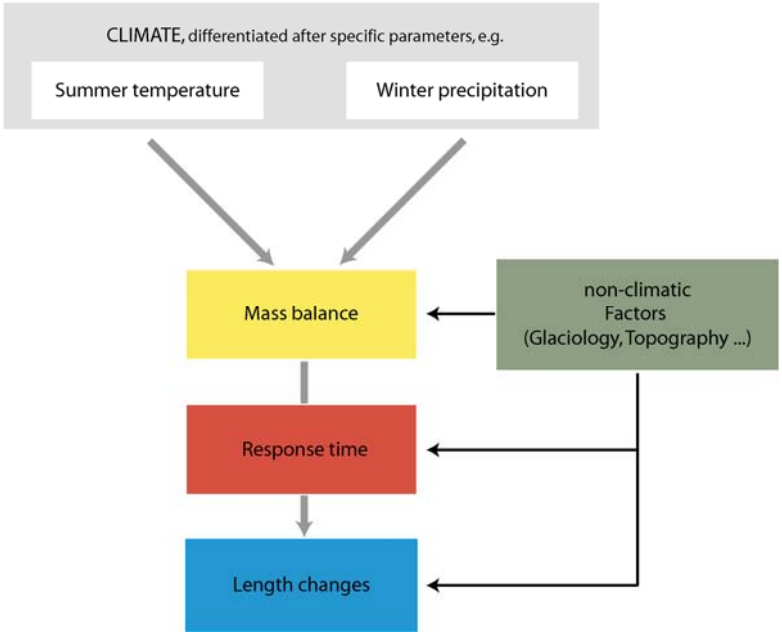

Figure 22: *The influence of climate conditions on glacier mass balance and length changes, and also the way how modern glacier-climate studies proceed. Modified after Winkler (2009).*

Glaciomorphologic features are classified into erosional and sedimental forms. While erosional forms and processes dominate in the accumulation area, sedimentation occurs mainly in the ablation area. In general, the most striking traces are produced by temperate glaciers during advances phases, while cold glaciers leave less traces and, consequently, are often underestimated (Häberli 2004). The most important sedimental landforms are moraines, and lateral and terminal moraines are particularly important for reconstructing former glaciations. Also the glacial trimline is an easy-to-distinguish feature, indicating the position of the former glacier surface (Winkler 2009).

Information about climate conditions during the advance phase are recorded in the length, the form, ice thickness, the paleo equilibrium line altitude (pELA) and the AAR. ELA depressions are often used to calculate temperature depressions by simply applying standard atmospheric lapse rates, but also precipitation must be considered, especially in arid climates (e.g. Klein et al. 1999). Nevertheless, the reconstruction of the pELA is an integral part of any paleoglacier reconstruction, because (1) the climate at the ELA is of particular interest and (2) knowledge of the ELA allows to calculate the AAR, which also contains climatic information.

Several methods exist for reconstructing the former ELA (e.g. Nesje 1992, Paterson 1994, Winkler 2009); all methods need more or less information about the former ice extent. The AAR method calculates the ELA from a standard AAR value (chapter 3.1). Thereby, the climatic information contained in the AAR is obviously not considered. The toe-to-headwall-ratio (THAR) or the median elevation of glaciers (MEG) methods are only recommended for small glaciers. In the present study, the maximum elevation of lateral moraines (MELM) is used to calculate the former ELA. This method refers to the ice flow vectors, who diverge only below the ELA, and therefore, only produce lateral moraines below the ELA.

It is important to note that every glacier advance overrides the traces of former, less extensive ones. Finally, only the maximum extent of a glacier, and possible minor readvances during a general retreat phase, are preserved. When reconstructing climate conditions from former glacier extents, one has to be aware that the climate during the advance represents extreme climate conditions and not mean values. Reconstructed paleoclimate conditions can be compared to other proxies, and one can try to attribute them to specific timings. However, direct dating of glacier advances is important, and the combination of datings and reconstructing climate conditions has proofed to be very fertile. The dating techniques applied depend on the climate conditions. Usually, organic material for ^{14}C (radiocarbon) dating is very scarce in arid climates. Despite of methodological uncertainties (e.g. Zech et al. resubmitted) surface exposure dating (SED) of cosmogenic nuclides has worldwide been increasingly applied in the past years and proven to be a powerful tool providing absolute age control (e.g. Zech et al. 2007a). SED is also applicable in arid climate, but requires silicate-containing stones

.

4 Methods

Modern and paleo glacio-climatological conditions are reconstructed by using the glacier-climate model from Kull (1999). It is fed by several topographic and climatic input parameters that are created by reconstructing the paleoglacier (4.2) and by analyzing modern local climate (4.3).

4.1 Glacier-climate model

The model was developed in order to reconstruct late Pleistocene climate from observed glacier extents in regions of the Central Andes with prevailing summer precipitation. In the past 10 years, it has been successfully applied to several study sites on the western (Kull 1999, Kull & Grosjean 2000, Kull et al. 2002) and eastern (Kull et al. 2003, Imhof 2006, Schmidhauser 2007, Kull et al. 2008) slope of the subtropical Central Andes (Figure 1). In contrast to glacier-climate models in mid-latitudes or polar regions, this model also accounts for sublimation in the mass balance calculations, which is essential in the (sub)tropics. Based on Kull (1999) and Kull and Grosjean (2000) where it is described in detail, the underlying assumptions of the model, its components and the modeling procedure are presented in the following. Finally, also the necessary adaptations to a winter precipitation regime are outlined (chapter 4.1.6).

The model consists of a climate, a mass balance and a dynamical ice flow model. It bases on two assumptions: (1) an increase in precipitation during late Pleistocene times was due to strenghtened summer precipitation; (2) modern transfer-functions between climate and ablation and climate and accumulation are applicable also for late Pleistocene times (actualistic principle). Input parameters are:

1. a detailed mapping of the late Pleistocene glaciation
2. a description of modern climate through diurnal and annual cycles, amplitudes and lapse rates of several climatic parameters
3. empirical-statistical models describing the mass balance terms sublimation, melt and accumulation based on the climatic input parameters
4. dynamic ice flow calculations through two known cross-sections in the ablation area.

4.1.1 Climate model

In the climate model, daily and annual cycles of all climate parameters are mathematically described by sinusoidal functions (Table 1). The main control parameters are temperature, precipitation and cloudiness. Daily convection leads to cloud cover in the afternoon in summer. The temperature maximum is reached at 15:00 and the convection maximum at 18:30 local time (Ammann 1996). By analyzing station data, Kull (1999) defined correction terms for temperature, considering a temperature drop if the sky is cloudy and if precipitation occurs. Summer precipitation from daily convection is linked to summer cloudiness by an empirical-statistical relationship (Ammann 1996). In winter, precipitation is not linked to cloudiness, because the westerly fronts arrive at any time and do not follow a daily cycle.

CLIMATE:		
Temperature	$T_{t,h}$[°C]:	$T_{t,h} = Ym + Ya(\cos\ d) + (Da + C^*)\cos\ t + grad_h + P^*$
Cloudiness	$Cs_{t,h}$[%]: (summer)	$Cs_{t,h} = Ym + Ya(\cos d_s) + Da(\cos t_s) + grad_h$; 0<Cs<100
	$Cw_{t,h}$[%]: (winter)	$Cw_{t,h} = Wm + Wa(\sin d_w) + grad_h$; 0<Cw<100
Precipitation	$Ps_{t,h}$[mm]: (summer)	$Ps_{t,h} = 0.161 Cs_{t,h}^{\ 2} + 0.81 Cs_{t,h} + grad_h$
	$Pw_{t,h}$[mm]: (winter)	$Pw_{t,h} = Wm(Cw_{t,h} Wm^{-1}) + grad_h$
Rel. humidity	$RH_{t,h}$[%]:	$RH_{t,h} = Cs_{t,h} + Cw_{t,h} + grad_h$
Wind speed	$W_{d,h}$[m s^{-1}]:	$W_{d,h} = Ym + Ya(\sin d) + grad_h$
Global radiation	G[W m^{-2}]:	$G = 1.05 * (1 - kC) * S_0 * E_0 * \cos\xi * \left[\frac{0.907}{(\sin H)^{0.018}}\right]^{\frac{T}{\sin H}}$
Deg. -day-fac.	$DDF_{d,h}$[mm °C^{-1} d^{-1}]:	$DDF_{d,h} = Ym + Ya(\cos d)\cos h + grad_h \sin h$

CORRECTIONS:		
Temperature:	P*: Correction term due to precipitation,	T = -4°C if P > 0.
	C*: Correction term due to cloudiness,	Da=-0.03°C if C=100%

Da: daily amplitude	Ya: annual amplitude	Ym: annual mean value
$grad_h$: lapse rate (h/100m)	t_s: hours in summer	P*: precipitation corr.
k: empirical coefficient	C: Cloudiness (in tenth parts)	d_w: days in winter (Apr-Sep) [f(t)]
Wm: winter mean value	t: hours	d_s : days in summer (Oct-Mar) [f(t)]
Wa: winter amplitude	h: altitude	d: days [f(t)]
S_0: solar constant (1370Wm^{-2})	E_0: Excentricity correction factor	ζ: zenith angle of the sun to an inclined surface
T: Linke turbidity factor	H: zenith angle of the sun	

Table 1: *Parametrization as used in the model for the daily and annual cycles and amplitudes of climate parameters (Kull et al. 2008).*

4.1.2 Mass balance model

The modeled climate parameters are used to calculate mass balance for every hour and every altitudinal segment (Table 2). Ablation by sublimation is linked by an empirical-statistical model to the climate parameters wind, global shortwave radiation, and vapour pressure deficit (Vuille 1996). In February 1999, Kull (1999) measured sublimation rates of ~2-3 mm water equivalents (WE) per day on Co. Tapado (~30°S) with a lysimeter, and found, that Vuille's model, established at ~24°S, could also be successfully applied to the winter precipitation conditions around 30°S. Ablation by melt is linked by a linear model to the degree-day factor (DDF) (Vuille 1996). Kull (1999) interpolated a DDF-function based on winter values from Vuille (1996), summer values from the Zongo glacier in Bolivia (16°S) and literature review. Temperature determines whether precipitation falls as rain or snow, and thus controls the accumulation process on the glacier. Below 2°C, any precipitation (100%) is considered as accumulation, whereas above 4°C, accumulation is 0%. Between 2 and 4°C, the fraction of precipitation counting as snow (and therefore as accumulation) is linearly interpolated. Specific annual mass balance for any altitudinal segment is finally calculated by adding up sublimation, melt and accumulation.

MASS BALANCE:		
Sublimation	$subl_{d,h} = -1.33 + 0.12(W_{d,h}) + 0.24\,(Dd_{d,h}) + 0.27(G_{d,h})$	[mm d^{-1}]
	with: $W_{d,h}$: max. hourly wind velocity (daily average)	[m s^{-1}]
	$Dd_{d,h}$: mean daily vapour pressure deficit	[hPa d^{-1}]
	$G_{d,h}$: daily global radiation energy	[W m^{-2}]
Melt	$melt_{d,h} = 0.97 + DDF_{d,h}\,(Tg_{t,h})$; for Tg>0	[mm d^{-1}]
	with: $Tg_{t,h}$: hourly means of the positive temperatures per day	[°C]
	$DDF_{d,h}$: degree-day-factor, *f*(albedo, snow density, climate)	[mm $°C^{-1}$ d^{-1}]
Accumulation	$acc_{d,h} = \frac{1}{24}\sum_{t=24d}^{24+24d}\begin{pmatrix} P_{t,h}; & if\ T_{t,h} < 2 \\ \left(\frac{4-T_{t,h}}{2}\right)P_{t,h}; & if\ 2 \le T_{t,h} \le 4 \\ 0\ otherwise & \end{pmatrix}$	[mm d^{-1}]
	with: $P_{t,h}$: hourly precipitation	[mm]
	$T_{t,h}$: hourly mean temperature	[°C]
Specific annual mass balance	$b_h = \sum_d -(subl_{d,h} + melt_{d,h}) + acc_{d,h}$	[mm a^{-1}]

Table 2: *Empirical-statistical models for the mass balance modeling (Kull 1999, Kull & Grosjean 2000).*

4.1.3 Dynamical ice flow model

The calculation of dynamical ice flux bases on detailed 3D-mapping of at least two cross sections in the ablation area. Mass flux through these cross sections is calculated after Oerlemans (1997) and Budd (1969) by the use of the following equations (Kull 1999): The form correction factor F is

$$F = \frac{Q}{H * B} \qquad \text{Equation 11}$$

with Q = cross section area [m2], H = ice thickness [m], B = hydraulic radius [m], g = acceleration due to gravity [9.807 ms^{-2}], ρ = ice density [900 kgm^{-3}], α = bed slope [°]. F allows to calculate mean basal shear stress τ after equation 9. τ is needed to calculate basal flow velocity u_b and the mean velocity of internal deformation u_{md}, which together result in the mean flow velocity u_m through the cross section:

$$u_b = \frac{f_s * \tau^3}{H} \qquad \text{Equation 12}$$

$$u_{md} = f_d * H * \tau^3 \qquad \text{Equation 13}$$

$$u_m = u_b + u_{md} = f_d * H * \tau^3 + \frac{f_s * \tau^3}{H} \qquad \text{Equation 14}$$

with f_s = standard flow parameter of basal sliding [$5.7*10^{-20} Pa^{-3} m^2 s^{-1}$], f_d = standard flow parameter of internal deformation [$1.9*10^{-24} Pa^{-3} s^{-1}$]. Finally, the cross section mass influx M [kgs^{-1}] is calculated by multiplying the mean flow velocity through the cross section u_m with the cross section area Q:

$$M = u_m * Q * \rho \qquad \text{Equation 15.}$$

.

4.1.4 Steady-state conditions

The aim of the model is the reconstruction of paleoclimatic conditions enabling the glacier to be in equilibrium with climate in the observed geometric extent as outlined in chapter 3.3. In the model, two conditions must be fulfilled for a glacier in steady-state:

1. Mean annual mean mass balance over the whole glacier surface is zero:

$$0 = \sum_{\Delta h} \left(b_h * A_h \right) \qquad \text{Equation 16}$$

with Δh = altitudinal segments of the reconstructed glacier surface; b_h = specific mass balance of an altitudinal segment and A_h = area of an altitudinal segment.

2. The annual flux M through a given cross section (here at 2500m asl) in the ablation area corresponds to the annual mass balance of the glacier below this cross section.

$$DMM_{2500} = \sum_{\Delta h=0}^{2500} \left(b_h * A_h \right) + M_{2500} = 0 \qquad \text{Equation 17}$$

with DMM_{2500} = the difference between mass influx at 2500m asl and the total mass balance below 2500m asl.

Condition 1 is the prerequisite for a modeling in 2D, which only considers the area of the glacier. Several precipitation/temperature (P/T) combinations provide a numerical solution for a modeling in 2D. Condition 2 must be fulfilled for at least two cross section in the ablation area to allow a modeling in 3D, which also considers the ice volume and dynamical ice flux. Theoretically, only one P/T combination fulfills condition 2.

4.1.5 Modeling process

The flow chart of the glacier-climate model is shown in Figure 23. Climatic parameters are calculated on an hourly basis for all the altitudinal segments (equidistance of 100m) by applying altitudinal gradients. They are used to calculate the mass balance terms melt, sublimation and accumulation with the same temporal and spatial resolution. By iteratively changing the main control parameters (temperature, precipitation and cloudiness), several P/T solutions are found for a 2D modeling. If the glacier geometry allows a 3D modeling, only one single P/T solution results.

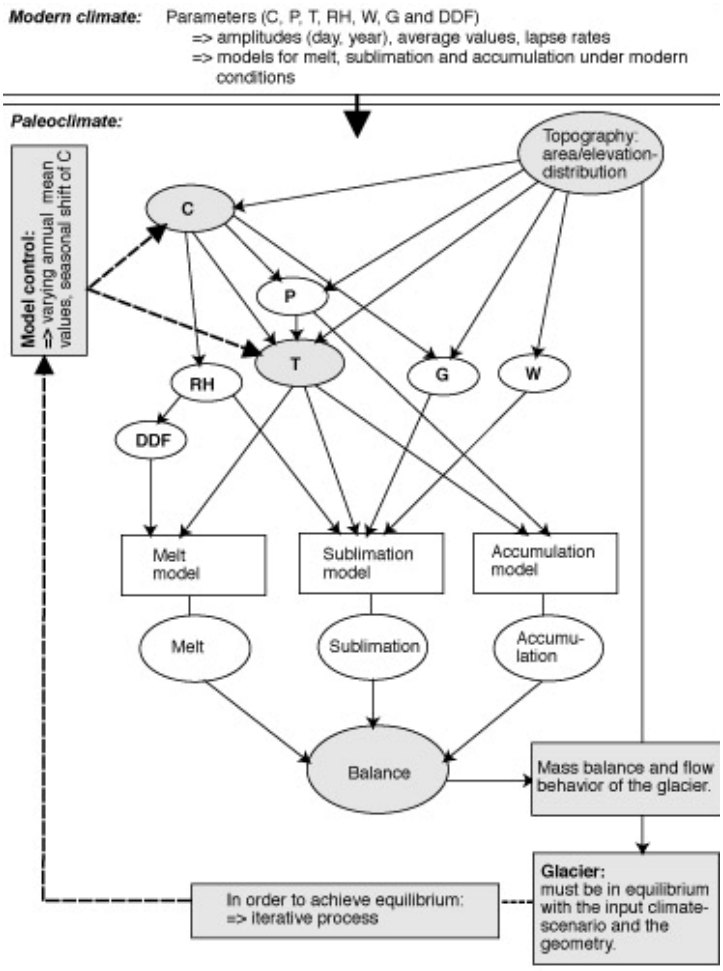

Figure 23: *Flow-Chart of the glacier-climate model (Kull et al. 2003). The climate parameters are C (cloudiness), T (temperature), P (precipitation), RH (relative humidity), G (global radiation) and W (wind). The parameters C and T influence the other climatic factors (P, RH, G) and, ultimately, the climate in the study area. The mass balance terms are calculated as shown in Table 2. Modelled mass balance parameters are compared with field observations. C and T are tuned iteratively to obtain optimum agreement between modeled and in the field measured values (Kull et al. 2008).*

4.1.6 Adapting the model to a winter precipitation regime

The empirical-statistical relationship linking summer precipitation to cloudiness was developed in the arid Central Andes where summer precipitation prevails. This is also the case for the empirical-statistical models describing the mass balance terms melt, sublimation and accumulation. One of the main tasks of this study is to find out if the glacier-climate model fits to investigate glacio-climatological conditions in the semiarid to humid winter precipitation regime of the study area. This was finally tested by applying the model to modern conditions in the study area, and no new empirical-statistical models were developed. However, some adaptations to a winter precipitation regime are made in the climate model, affecting the correction terms for temperature due to precipitation and cloudiness cooling (Table 1). These adaptations are necessary according to the way how winter precipitation and cloudiness are parametrized in the model.

In the model, convective summer precipitation only occurs when cloudiness has reached 100%. On the other hand, winter precipitation is not linked to cloudiness. Total amount of winter precipitation is manually entered, and winter cloudiness is only used to disperse total winter precipitation over the whole winter season. Hence, frontal winter precipitation in the model is not described by several strong frontal precipitation events as it is the case today in the region of the study area today (e.g. Viale & Norte 2009). According to this parametrization, winter precipitation and cloudiness exhibit positive values for all time steps in the winter season.

In the climate model, a correction term for temperature is used compromising a precipitation cooling (of 4°C as soon as precipitation occurs) and a cloudiness cooling (the daily amplitude of temperature is lowered by 3°C if cloudiness reaches 100%). These correction terms apply only in summer, where convective cloudiness and precipitation damp incoming solar radiation during daytime, leading to a temperature drop. Having parametrized winter precipitation as described above, it is implicitly assumed that winter precipitation and cloudiness equally occur during both day- and nighttime. However, a cloudiness cooling makes only sense during daytime, where cloudiness has a cooling effect on temperature. During nighttime, cloudiness lowers longwave irradiation resulting in a relative warming effect. Hence, in the present study, the correction term for cloudiness was omitted for the winter season, and also the correction term for precipitation was not considered: Because precipitation values are above 0 for the whole winter season, the application of the correction for precipitation cooling would cause a systematical decrease of winter temperatures. It is argued here that the temperature drops during precipitation events is already considered in the seasonal temperature data. In summer, the correction terms were used. However, the precipitation cooling of 4°C was concluded to be too high in Las Leñas, where daily amplitude of temperature is clearly lower than in the subtropics where the terms were established by Kull and Grosjean (2000). Hence, a correction term for

the precipitation cooling of only 2°C instead of 4°C was applied. By analyzing the previous studies working with the glacier-climate model, it has become obvious, that the correction terms for cloudiness and precipitation were also used in the winter months in all past studies. Indeed, no significant consequences on the modeling outcome resulted, because almost all of the studies were located in a summer precipitation regime, where winter cloudiness and precipitation was negligible. Only for the study Northern Chile ~30°S (Kull et al. 2002), a remodeling without using the temperature corrections terms in winter could be interesting.

Obviously, the conventional parametrization of winter cloudiness and precipitation is a strong simplification. In reality, the bulk of total winter precipitation is the result of some intense snowfall events each lasting for some hours to a few days (e.g. Viale & Norte 2009). Indeed, daily MODIS satellite pictures from June to September 2008 (total 121 days) showed clear-sky conditions on 49 days, a partially cloudy sky on 33 days and a cloudy sky on 38 days (Figure 24 and Figure 25). It would be technically possible to parametrize winter precipitation and cloudiness in the model in a more sophisticated way, by composing total winter precipitation of several frontal precipitation events. The intensity and duration of these events could be randomly defined and the events could be randomly distributed over the winter season. By applying such a parametrization, the impact of interannual variability on mass balance could be investigated. In the study area, this would be particularly interesting to study the effects of El Niño and La Niña events.

However, in the present study, the conventional parametrization was maintained for the following reasons: (1) We are not interested in the interannual variability of mass balance, but in the long-term equilibrium state. Such a long-term equilibrium state is the response to mean climate conditions, prevailing over several decades. (2) The parametrization of single precipitation events requires detailed data about the seasonal spreading of occurrence, duration and intensity of such events, which is difficult to obtain.

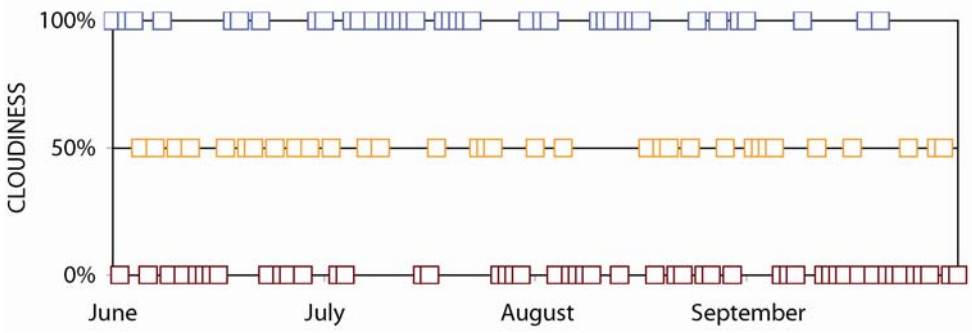

Figure 24: *The distribution of cloudy (100%), partially cloudy (50%) and clear-sky conditions in Las Leñas as classified by considering daily MODIS pictures (see also Figure 25).*

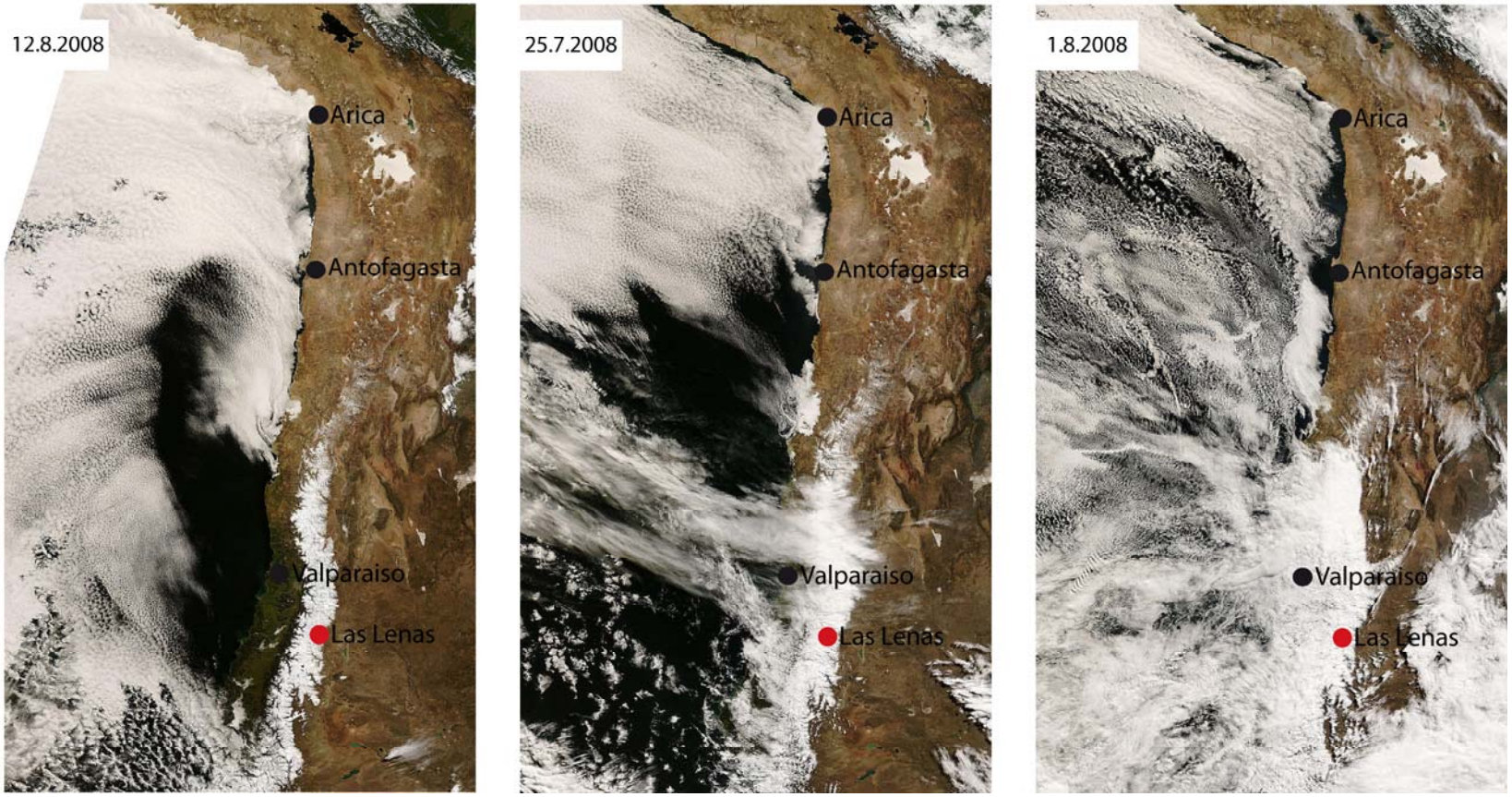

Figure 25: *Three MODIS satellite pictures from the Central Andes during austral winter showing clear-sky (left), partially cloudy (center) and cloudy (right) conditions in Las Leñas. This illustrates that the parametrization of winter cloudiness (and precipitation) in the model is a strong simplification.*

4.2. Reconstructing the paleoglacier

The glacier-climate model is fed by the following topographic input parameters: (1) The area/elevation distribution of the glacier, divided up in altitudinal segments of 100m equidistance for a modeling in 2D and (2) at least two cross sections in the ablation area for a modeling in 3D. First, the maximum glacier extent is mapped in 2D (4.2.1). The analysis of cross sections in the ablation area (4.2.2) allows the calculation of basal shear stress τ, which is necessary for the reconstruction of the former glacier surface (4.2.3)

4.2.1 Mapping of the maximum extents

The former glacier extent was reconstructed by applying the following criteria: (1) If existing, terminal moraines indicate the glacier tongue; (2) lateral moraines define the ablation area; (3) the maximum elevation of lateral moraines (MELM) indicates the paleo equilibrium-line-altitude (pELA); (4) the accumulation area is defined by the hydrologic catchment. Most probably, not the whole hydrologic catchment was covered by ice. Especially steep rock walls were likely to be ice free, which is known from modern glaciers in mountain regions. However, as these steep parts contribute to the accumulation by snow avalanches they are also counted to the accumulation area.

The mapping was performed in the Geographic Information System (GIS) ArcMAP, and mainly bases on fieldwork (carried out in December 2008), remote sensing data and digital elevation models (DEM). A summary of the imagery data used in this study is given in Table 3.

Data	Use	Resolution	Source
Google Earth (orthorectified)	Mapping, elevation data	~ 5m	Google Earth
MODIS Terra true color	Seasonality of precipitation, estimation of winter cloudiness	250m	NASA
SRTM (orthorectified DEM)	Elevation data, Hydrology tools, Base for the reconstructing of the former glacier surface	90m	USGS
GTOPO30 (orthorectified DEM)	Visualisation	~ 1km	USGS

Table 3: *Summary of the imagery data used for the mapping and in the present study in general.*

The ablation area was measured with a GPS, and the tracks were digitalized in Google Earth. Conversion from a shapefile and georeferencing was performed in GlobalMapper. Together with the

DEM, the shapefile was uploaded in ArcMAP. The hydrologic catchment, delineating the accumulation area, was defined as follows: First, sinks in the surface of the DEM were filled. Then, the flow direction was calculated for the flow out of every grid cell. There are eight valid output directions relating to the eight adjacent cells into which flow could travel. This finally allowed to evaluate the flow accumulation around the ELA defining the potential accumulation area.

4.2.2 Cross sections in the ablation area

Cross sections in the ablation area are needed for two reasons: (1) The calculation of τ in the ablation area is needed for the reconstruction of the former glacier surface. For calculating τ, the topographic terms ice thickness, cross section area and the hydraulic radius of the cross section and the bed slope angle must be known (equations 9 and 10). (2) A detailed analysis of at least two cross sections in the ablation area are needed for the 3D-Modeling. However, only glaciers fulfilling all the criteria summarized in Table 4 are theoretically suited for a 3D analysis. These criteria were evaluated in the field and three cross sections in the ablation area were recorded with a GPS.

criterion	importance
1. A general simple topography in the ablation area with relatively constant bed slope angles and no strong changes in flow direction	assumption of standard flow velocity parameters
2. End moraine stages, which can be clearly assigned to specific lateral moraine stages	guarantees the modelling of the correct moraine stage
3. Sharp lateral moraines accurately indicating the former ice height	calculation of ice thickness
4. Morphologic phenomena pointing to the former ice base (such as detersion of bedrock, erosion of the ground moraine)	calculation of ice thickness

Table 4: *Criteria regarding the suitability of a glacier for a 3D modeling.*

Glacial valleys tend to have a parabolic shape that is efficient for the evacuation of varying volumes of ice (Sugden & John 1976). As a result of gravitative mass movements over thousands of years and the deposition of ground moraine material, today's cross sections rarely show this parabolic shape and hence, do not reflect exactly the former cross profile, which was also the case in the present study. Thus, the recorded cross profiles were fit in a parabolic shape. Furthermore, a parabolic superelevation (of 5%) was considered, because glaciers in the ablation area characteristically exhibit a convex surface (e.g. Sailer et al. 1999, Häberli et al. 2005).

4.2.3 Reconstruction of the former glacier surface

The reconstruction of the former glacier surface allows to assess ice thickness and total ice volume of the glacier. The final goal is to get the necessary topographic input parameter for the glacier-climate model, the area/elevation-distribution. Furthermore, the reconstructed glacier surface is also used for modeling shortwave global radiation.

There are several ways of reconstructing former glacier surfaces. A completely manual reconstruction is always subjective and depends on the scientist's experience. On the other hand, dynamic ice flow models are usually based on specific mass balance profiles which are rare for modern glaciers, and obviously do not exist for paleoglaciers. τ - models are simple and work without mass balance gradient data.

Here, a combination of a manual reconstruction and a τ - model based reconstruction was chosen. In the ablation area below the MELM, the former ice surface was manually reconstructed because the lateral moraines indicate the lateral height of the former ice surface quite accurately. The convex shape of the glacier surface in the ablation area was also considered (see previous chapter). Because the reconstruction of the ice surface is more difficult in the accumulation area above the MELM due to the lack of geomorphologic evidence and a generally more complex topography, the τ - model from Sailer et al. (1999) was applied there. This GIS-based model formulated in the ArcInfo computer language AML (Arc Macro Language) was developed for reconstructing Younger Dryas glaciers in the Ferwall group in Western Austria. It bases on empirical-statistical models, and on the idea of a constant τ throughout the glacier. The application of the model is restricted to glaciers with a simple bed topography, e.g. without abrupt changes in slope, and a geometrically simple catchment area. Basic input parameters are a DEM, outlines of the glacier cirque area and τ. Based on Sailer et al. (1999), the basic features of the model are presented in the following.

Regression analysis from data of the Gepatschferner (Austria) showed a statistical relation between the surface slope α and the bed slope β of the glacier (all angles in degrees):

$$\alpha - \beta = \delta s = 4.34 - 0.82 * \beta \qquad \text{Equation 18}$$

with a correlation coefficient of -0.83. This was found statistically sufficient, because the largest deviations occur where bed slope is steep and, therefore, ice thickness is small. By solving Equation 17 for α and inserting it into the equation 9, ice thickness H can be calculated as

$$H = \frac{\tau}{\rho * g * \sin(\beta + \delta s)}$$ Equation 19

under the assumption of a constant τ. H is calculated for every cell and added to the basic DEM to obtain the glacier surface height *H*. However, in GIS, ice thickness can not be added vertically to a raster grid, and, therefore, the calculated ice thickness *h* must be divided by $cos\,\beta$. This correction is especially important where slope angles are >45°. In the present study, this is only the case at the boundaries of the glacier area and therefore, this correction factor was not considered here. According to Imhof (2006), Sailer estimated that the quality and resolution of the DEM, and the manual correction after the model run, influence the result at least in the same order as does the correction of H itself.

The resulting raster grid with the glacier surface height H shows a very detailed pattern which has to be smoothed. In ArcMAP, smoothing of raster grids is done with the focalmean-function, and the including of quadrats with different numbers of surrounding cells was tested. Finally, smoothing was performed first by the mean value of the 5 * 5 surrounding cells (450m * 450m) and then by the mean value of the 3 * 3 surrounding cells (270m * 270m). The resulting contours of the reconstructed surface height were smoothed, but still remained detailed. A slight manual correction of the contours was necessary close to the border of the catchment, where they were disturbed.

4.3 Deriving local climate parameters

The analysis of modern local climate conditions is needed to generate the necessary climatic model input parameters (Table 1). The parameters precipitation, cloudiness, temperature, wind, relative humidity and degree-day-factor are assessed by using statistical methods and by reviewing the literature (chapter 4.3.1). Global shortwave radiation is modeled (chapter 4.3.2).

4.3.1 Statistical analysis and literature review

In general, climatic data in the Central Andes is much less abundant than in e.g. in the Alps. Even if available, data must always be questioned critically for several reasons: The equipment used differs, the climate at the location of a meteorological station is only an approximation to the "true" climate of the area due to local effects, and the way of processing raw data is often not documented and can contain errors.

Climatic data from high-altitude stations in the Central Andes around the study area is scarce and – even if existing – turned out to be difficult to obtain. The data from stations of the Servicio Meteorologico Nacional de Argentina (SMNA) are accessible, but almost all of them were recorded in the lowlands. The same is true for Chile. High-altitude stations often belong to private companies or other public authorities. The Departamento General de Irrigacion in Mendoza operates several meteorological stations in the Central Andes, partly not far from Las Leñas, but data could not be obtained even upon repeated request. The private company running Las Leñas ski resort maintains several meteorological stations which are also used for avalanche forecasts. According to Ms. Amalia Ramires from the International Center for Earth Sciences ICES in Malargüe, negociations with the operator were underway to make the precious data accessible to science and also to the national weather service of Argentina (personal communication in December 2008). She also established contact to M. Torres who works for the ski resort in Las Leñas. Because of intern directives, he could not deliver the data we asked for. The only little information obtained was (all for 2240m asl, original wording):

1. annual mean precipitation is 250mm in water and 7m in snow
2. snowfall record is 12.60m (in 2005)
3. the main precipitation period is from autumn to spring
4. most important precipitation events usually occur in July and August

5. annual mean relative humidity is 15-40%, 50% from autumn to spring and 20-25% in summer

6. air pressure is 785 mbar when weather is good and 775 mbar when it rains. Sometimes, heavy precipitation events are registered with ~15cm snow per hour, who bring air pressure down to 755-760 mbar.

Obviously, this information gives only a rough clue about the climatic conditions on-site. Other station data (Appendix I) and data from the literature had to be considered. A lot of station data from Chile and Argentina could be obtained from Raphael Neukom (GIUB, personal communication in 2008). Data from high-altitude stations in the Andina mine in Chile (33°S) was kindly provided from Martin Zimmerli (Sensalpin GmbH, personal communication in 2008). Because of the limited availability, this study uses a combination of as much different kinds of information as possible to approximate *true* climate. Note that not all the data listed in Appendix I were used to create the input parameters for the model. Some were only used to recognize regional patterns.

Precipitation

The only station data that could be obtained was located too far away to reflect local precipitation amounts around the study area. It was only used to qualitatively approach the precipitation regime in Las Leñas. Therefore, information about annual and seasonal mean precipitation and distribution from Jorge Torres (see above) was combined with data from the literature and station data.

Cloudiness

In the glacier-climate model, summer cloudiness emerges from the parametrization of summer precipitation. Data for winter cloudiness was not available. Therefore, winter cloudiness was defined based on the following information and assumptions: (1) Cloudiness is higher in winter than in summer, because most precipitation falls as snow in winter; (2) Mean winter cloudiness was roughly estimated by analyzing daily MODIS satellite pictures from the Central Andes (Figure 24 and Figure 25); (3) The transition from daily mean summer cloudiness to daily mean winter cloudiness was set as continuous as possible.

Temperature

In the region of the study area, temperature exhibits a much lower meridional and longitudinal gradient than precipitation. The closest temperature data available is from Malargüe on the Argentinian slope of the Andes. All these stations show a similar seasonal cycle. Annual mean

temperature and amplitude in Las Leñas was extrapolated from Malargüe by applying a vertical temperature gradient that was calculated from NCDC data from Santo Domingo (Chile, 33°S). The resulting seasonality of temperature was improved by considering published data. For investigating the daily amplitude of temperature, data with high temporal resolution (30min intervals) from four stations (CAND1-4) was analyzed. Only data from wind protected snow station CAND2 was used, where daily cycles are best pronounced.

Wind

The data from wind station CAND4 was estimated to be most reliable due to its wind exposure. The annual mean and amplitude was extrapolated to the base height of the study area by applying the lapse rate from Kull (1999).

Relative Humidity

Annual mean and annual amplitude of relative humidity depends on cloudiness (Table 1) and, hence, had not to be analyzed. The lapse rate of relative humidity was taken from (Kull 1999).

Degree-day-factor (DDF)

The DDF is used to model ablation by melt in the mass balance model (see chapter 4.1.2). The DDF relates the amount of ice (or snow) melt to the sum of positive air temperatures in a time interval (e.g. Hock 2003). It depends on ice (snow) characteristics, climate and season (e.g. Kull 1999) and varies considerably. Hence, when describing melt by a degree-day model, it is important to work with DDF values reflecting local conditions.

No DDF values from the Central Andes around the study area were found, and measuring own values was not possible. Some values are published for Patagonia (Hock 2003, Schneider et al. 2007, Buttstädt et al. 2009) with values ranging from 7.1 to 9.4. For his studies in the north Chilean Andes, Kull (1999) interpolated a DDF-function depending on time and altitude, which is calibrated for the dry cold winter conditions on the southern Altiplano (Vuille 1996) and for humid warm summer conditions on Zongo glacier in Bolivia (26°S / 68°W). For their study in the Encierro valley and on the Cerro Tapado in Chile (29°-30°S), Kull and Grosjean (2002) adopted this function also for a climate regime with prevailing winter precipitation. They highlight that the resulting DDF values are low compared to DDF values calculated for mid- and high-latitudes in the Northern Hemisphere, because the sublimation process is separately considered. In the present study, the same DDF-function is used. The values from Kull and Grosjean (2002) are calibrated to the study area in Las Leñas by assuming that the DDF at the modern ELA at Co. Tapado is equal to the DDF at the modern ELA in Las Leñas.

4.3.2 Modeling of global shortwave radiation

Global shortwave radiation is necessary for calculating the sublimation in the mass balance model (Table 2). Global shortwave radiation describes the radiation hitting the earth's surface after passing through the atmosphere (Figure 26). It consists of the direct radiation from the sun and the diffuse radiation from clouds and air particles. The global shortwave radiation at the Earth's surface is only a fraction of the top-of-atmosphere (TOA) shortwave radiation from the sun (e.g. Pidwirny 2006).

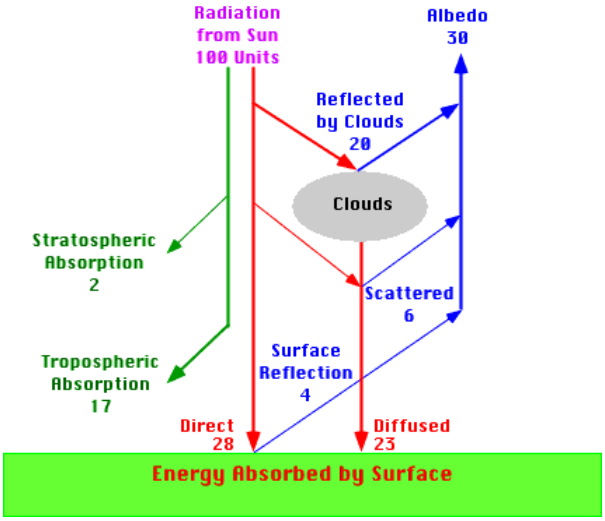

Figure 26: *The global shortwave radiation cascade (Pidwirny 2006).*

In the present study, global shortwave radiation is calculated by adopting the combined radiation - terrain model from Mölg (2002), who applied it to investigate potential monthly radiation in the Rwenzori massif in East Africa. This model was later used to study the contribution of increased incoming shortwave radiation to the 20th century retreat of the Rwenzori glaciers (Mölg et al. 2003). It is written in AML, can be run in a GIS and has successfully been used to calculate global shortwave radiation on former glacier surfaces in the Andes of Cochabamba (Imhof 2006) and Sierra del Quilmes (Schmidhauser 2007). The model considers clear-sky as well as cloudy conditions. For this study, the model had to be adjusted and parametrized to the conditions in the study area. In the following, the model is presented; more details and all the original references can be drawn from Mölg (2002).

4.3.2.1 Parametrization

The basic topographical input parameter for the model is the DEM of the reconstructed former glacier surface. When assessing solar radiation back in time, one has to consider that at the time of the last local glacial maximum the earth's orbit parameters eccentricity *e*, the longitude of the perihelion of the earth's orbit ω and the obliquity of the ecliptic ε were different from today. Blatter et al. (1984) provide values for these three parameters for the period 200 ka BP to 20 ka AP (extract in Table 5). For the modeling of the shortwave global radiation, only the values for 0 (for modern conditions) and for 35 ka BP (for paleo conditions, according to the hypothesis of this study) were used.

ka BP	Eccentricity e	Ecliptic ε	Longitude of the perihelion ω
40	0.013	23.62	178.0
35	0.015	22.75	249.7
30	0.016	22.23	327.2
25	0.018	22.4	48.3
20	0.019	23.11	130.6
15	0.020	23.87	212.7
10	0.019	24.23	294.7
5	0.018	24.03	17.5
0	0.017	23.45	102.0

Table 5: *Earth's orbit input parameters for the solar radiation model. eccentricity (e), ecliptic (ε) and the longitude of the perihelion (ω) for the period 40 to 0 ka BP. Data from Blatter et al. (1984)*

To account for different amounts of cloudiness due to different precipitation regimes, three precipitation scenarios are conceived. Scenario A represents modern precipitation, the scenarios B and C represent a doubling and tripling of modern precipitation. The corresponding cloudiness values are defined in the glacier-climate model, and then implemented into the shortwave radiation model.

* Abbreviations of the parameters according to chapter 4.1.1
+ ann = annual; sum = summer; win = winter

Scenario	P [mm]			C [%]			Parametrization of C *					
	ann +	sum	win	ann	sum	win	Ym	Ya	Wm	Wa	Grad	Da
A	920	220	700	42.9	34.6	51.2	5	5	10	65	0.84	129
B	1620	220	1400	50.0	37.0	59.0	5	5	33	50	0.84	129
C	2320	220	2100	61.0	39.0	69.0	5	5	60	30	0.84	129

Table 6: *Cloudiness scenarios and their parametrization in the glacier-climate model according to the sinusoidal functions shown in Table 1.*

4.3.3.2 The radiation model

Clear-sky direct solar radiation on a planar surface can be written as

$$SW\downarrow(dir,clear) = S_0 E_0 \cos\varsigma\left[0.907/(\sinh)^{0.018}\right]^{T_L/\sinh} \qquad \text{Equation 20}$$

with the solar constant S_0 (1370W/m^2), the eccentricity correction factor E_0, the solar zenith distance angle on any inclined and oriented plane ς, the sun height over a plane for the specific daytime and season h and Linke's turbidity factor T_L. E_0 describes the shape of the earth's orbit around the sun, which is not a perfect circle but elliptical (Iqbal 1983). The orbit's eccentricity (e) can be interpreted as a measure of how much the shape deviates from a circle. A perfect circle has an eccentricity e = 0. Extraterrestrial solar radiation varies due to the earth's elliptical orbit around the sun. At present, it increases by about 7% from July 4 (Aphelion) to January 3 (Perihelion) when the earth is farthest respectively closest to the sun. The eccentricity correction factor E_0 accounts for this variation. It is the square of the ratio of the mean to the true distance of the earth to the sun. E_0 is calculated numerically. First, the mean anomaly M is calculated for any day of the year

$$M = \frac{2\pi}{T_e}/(t - t_0) \qquad \text{Equation 21}$$

with the orbital period of the earth around the sun (365.25 days) T_e, the angular phase shift $(t - t_0)$ with day angle t and the timing of the periapse passage t_0 (point of closest approach to the sun). M relates time (mean anomaly in day angles) to position (eccentric anomaly) for an elliptic orbit and represents the angular displacement (in radians) of the earth travelling at a mean angular rate of $2\pi / T_e$ around the sun. The eccentric anomaly E_n is solved iteratively, starting from $E_0 = M$, using

$$E_n = M + e\sin E_{n-1} \qquad \text{Equation 22}$$

The iteration is applied until the 8th decimal place remains constant. The true anomaly μ related to the eccentric anomaly is

$$\cos\mu = \frac{\cos E - e}{1 - e\cos E} \qquad \text{Equation 23}$$

The eccentricity correction factor E_0 for every day of the year is

$$E_0 = \frac{1}{r(\varphi)} = \frac{1 + e\cos\mu}{a(1 - e^2)} \qquad \text{Equation 24}$$

with a as the semi-major axis of the earth (exhibiting the relative value 1). The eccentricity correction factor representing the seasonal cycle of E_0 is formulated by the sinusoidal function

$$E_0(t) = E_{0mean} + E_{0amp}\cos(t - t_0)$$

where E_{0mean} is the annual mean value, E_{0amp} the annual amplitude of E_0 and $(t - t_0)$ the angular phase shift. The solar zenith angle of the sun ς on any inclined earth surface is

$$\begin{aligned}\cos\varsigma = {} & (\cos\beta\sin\varphi - \cos\varphi\cos\alpha\sin\beta)\sin\delta \\ & + (\sin\varphi\cos\alpha\sin\beta + \cos\beta\cos\varphi)\cos\delta\cos\theta \\ & + \sin\alpha\sin\beta\cos\delta\sin\theta\end{aligned}$$

with the azimuth angle of the plane α, the slope of the plane β, the geographic latitude φ, the hour angle of the sun θ and the solar declination δ. δ is calculated in radians as

$$\delta = (0.006918 - 0.399912\cos t + 0.070257\sin t \qquad \text{Equation 25}$$

with t as the day angle.

The term

$$\left[\frac{0.907}{(\sinh)^{0.018}}\right]^{\frac{T_L}{\sinh}} \qquad \text{Equation 26}$$

describes the atmospheric absorption of the shortwave solar radiation depending on the solar elevation h and atmospheric turbidity T_L. sinh is calculated as

$$\sinh = \sin\delta \sin\varphi + \cos\delta \cos\varphi \cos\omega \qquad \text{Equation 27}$$

The turbidity factor T_L is an indicator for the content of water vapour and haze in the atmosphere, and decreases with increasing height. T_L at sea level is

$$T_L = 1.39 + 0.112 e_0 \cong 1.9 \qquad \text{Equation 28}$$

with the water vapour pressure e_0 over the surface. An altitude correction is needed to take the altitude of the study area into account by applying the simplified barometric formula

$$p(H) = p_0 e^{\frac{-H}{h_s}} \qquad \text{Equation 29}$$

with the mean altitude of the study area H, air pressure at sea level p_0 (1013 hPa) and the scale height h_s (≈ 8000m). Finally, $T_L(H)$ results in 1.3 for the mean altitude of the study area (H = 3000) by applying

$$T_L(H) = 1.9 \frac{p(H)}{p_0} \qquad \text{Equation 30}$$

Diffused solar shortwave radiation under clear-sky conditions $SW\downarrow(diff, clear)$ is not important at high altitudes. Measurements on Mount Kenya showed that the diffuse component only accounts for ca 5%-10% of the total incoming clear-sky shortwave radiation, and at the Quelcaya ice cap in Peru the values are even lower (Hastenrath 1978, 1984). In the present study, $SW\downarrow(dir, clear)$ was considered as 5% of $SW\downarrow(dir, clear)$ leading to the total incoming shortwave radiation under clear-sky conditions

$$SW\downarrow(Clear) = SW\downarrow(dir, clear) + SW\downarrow(diff, clear) \qquad \text{Equation 31}$$

Direct incoming shortwave radiation under cloudy sky is

$$SW\downarrow(Cloud) = SW\downarrow(Clear) * (1 - kC) \qquad \text{Equation 32}$$

with *k* as an empirical constant, which is ~0.68 between 30 - 35°S (Budyko 1974) and the cloudiness in tenths, *C*, which is implemented from Kull's (1999) model.

The modeling calculations are performed from sunrise to sunset with a temporal resolution of 30 min. The time of sunrise and sunset can be expressed as an angle. The hour angle of the sun *at* sunrise ω_s is

$$\omega_s = \cos^{-1}(-\tan\varphi \tan\delta) \qquad \text{Equation 33}$$

the hour angle of the sun *at* sunset is $-\omega_s$.

First, a raster-based shading analysis (shading by the relief) of the DEM is operated. In a second step, $SW\downarrow(dir, clear)$ $SW\downarrow(dir, clear)$ and $SW\downarrow(Cloud)$ are calculated for the non-shaded raster-cells. Only raster-cells with $\cos\varsigma > 0$ are considered in the modeling calculations. Based on the half-hourly values, daily and monthly means of the total daily incoming shortwave radiation can be determined and converted into daily total incoming global radiation in W/m^2 per altitude, which is a parameter needed for the calculation of the sublimation in the glacier-climate model.

5 Results

5.1 Reconstructing the paleoglacier

5.1.1 Maximum extent

Lateral moraines reflecting the glacier extent in the tongue area are only found in the lowest part close to the village, where they are freestanding. When striking the mountain slopes, at an altitude of ~2540m asl, they disappear abruptly. In this study, the maximum elevation of lateral moraines (MELM) was taken as indicator for the pELA. However, it is unlikely that the ELA of Las Leñas paleoglacier was at only 2500m asl, given that the terminal moraines are at ~2200m asl and the highest elevation of the catchment is at ~3770m asl. Evidence that the pELA was most probably above the modern MELM arises also from the paleoglacier at Co. Las Leñas, where lateral moraines are preserved from ~2600-2900m asl. Note that the paleoglacier at Co. Las Leñas exhibit the only moraines of comparable extent in the whole valley. However, it was not used for the modeling, because no terminal moraines are recognizable.

Figure 27: *View of the (orographic) left lateral moraine to the maximal elevation of the orographic right lateral moraine, which is still being eroded (Photo: Wäger 2008).*

During fieldwork it became clear that the moraines further up in the valley must have been eroded, and that erosion is still ongoing today (Figure 27). Hence, the paleo-ELA could not be reliably derived from geomorphologic evidence. To assess the mapping uncertainties, two scenarios were conceived. In the first one, called ELA_2500, the hydrologic catchment was considered as the formerly glaciated area above the MELM. In the second scenario (ELA_3000), the ablation area was manually extended valley upward to an elevation of 3000m asl with respect to the slope of the today ice-free valley. Above this elevation, the hydrologic catchment was considered as the formerly glaciated area. While ELA_2500 most probably overestimates the former accumulation area, leading to very high and unrealistic AAR values (see chapter 5.1.3), ELA_3000 represents a glacier having a very long tongue in the ablation area. The resulting mapped extents for the two scenarios are shown in Figure 28.

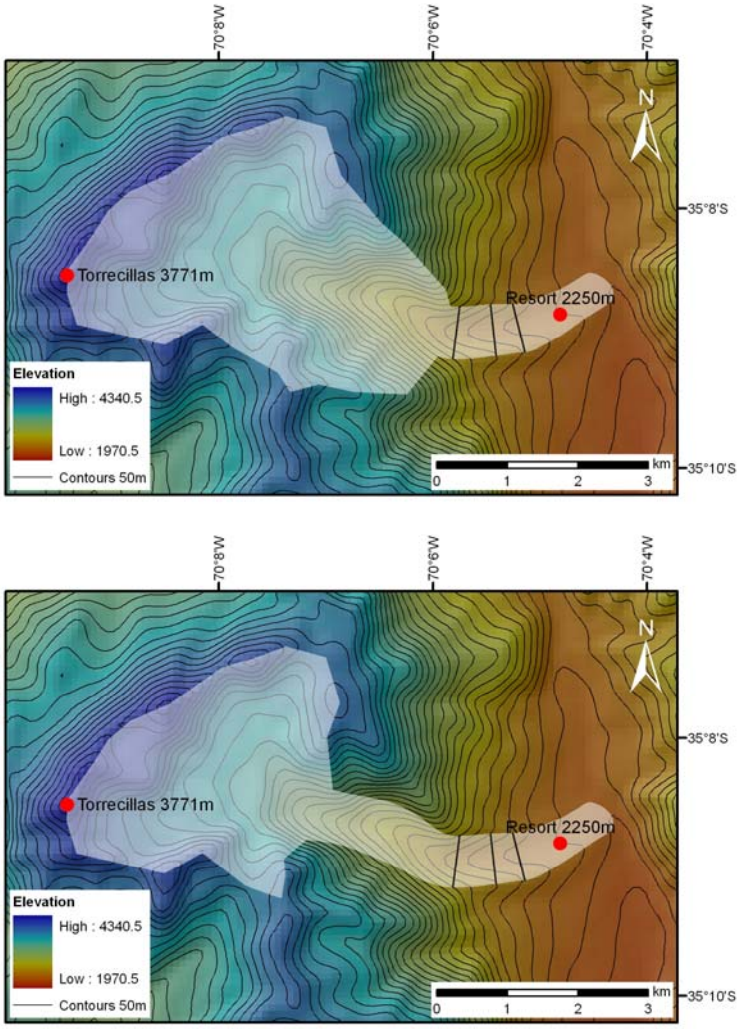

Figure 28: *The former glacier extent mapped according to ELA_2500 (top) and EA_3000 (bottom). The black lines represent the cross sections measured in the ablation area.*

5.1.2 Cross sections in the ablation area

Evaluating the criteria established in Table 4 leads to the conclusion that Las Leñas paleoglacier is not suitable for a 3D modeling. In general, topography in the ablation area is simple with gentle and relatively constant slope angles between 4.5 and 6°. Flow direction only changes slightly and continuously between 2550-2350m asl (criterion 1). In addition, the main end and lateral moraine stages can be assigned to each other with quite high confidence (criterion 2). However, lateral moraines do not exhibit a sharp feature everywhere (criterion 3). Below 2400m asl, the orographic right lateral moraine is rounded. Above 2400m asl, it is still quite sharp even though a track runs on the top (Figure 29 top). The form of the orographic left moraine is even more diluted: Above 2400m asl, it is clearly influenced by slope debris material and merged with the mountain hillside, and between 2300-2400m asl, a ski piste was built on its top. Below 2300m asl, the topmost part of the lateral moraine has been removed by human activity, leaving only a moraine "island" behind between 2250-2270m asl (Figure 29 center). Furthermore, it was not possible to determine the former ice base (criterion 4), because the whole ablation area is covered by ground moraine material. At the maximal erosion depth (~5m) of the small river running between the moraines, no bedrock is visible (Figure 29 bottom). In summary, criteria 1 and 2 can be considered as fulfilled, criterion 3 as only partly fulfilled and criterion 4 as not fulfilled at all, because the former ice thickness could not reliably be reconstructed. It is very likely that erosion has played an important role in shaping the ablation area. Nevertheless, three cross sections in the ablation area at altitudes of 2500, 2400 and 2340m asl were measured during fieldwork. An assumed erosion of the lateral moraines by 5m and a filling of the valley by ground moraine material by 10m was assumed. Table 7 shows the characteristics of the cross section. The τ - values range between 0.45 and 1.04 bar, which fits well to values of alpine valley glaciers ranging from 0.5 – 1.5 bar (Paterson 1994). However, there are large differences between the three different cross profiles. With increasing altitude, the F-factor decreases slightly, but the increase in ice thickness and bed slope finally lead to higher τ - values valley-upward.

Cross Section	Ice thickness [m]	Width [m]	Area [m^2]	Hydraulic radius [m]	Shape Factor [-]	Slope [sin α]	basal shear stress τ [bar]
2500	165	707	77699	791	0.595	0.120	1.04
2400	121	677	54498	726	0.621	0.085	0.56
2340	93	665	41429	695	0.637	0.085	0.45

Table 7: *Characteristics of the three cross sections measured in the ablation area. The location of the cross sections is shown in Figure 28.*

Figure 29: *Photos taken during the field campaign in December 2008.*

TOP: Orographic right lateral moraine. Left: View valley upward at an altitude of ca. 2350m asl. Right: View valley upward at an altitude of ca. 2450m asl.

CENTER: Orographic left lateral moraine. Left: View valley upward at an altitude of ca. 2430m asl Right: Lateral left moraine seen from opposite right moraine. The removed top part of the moraine below 2300m asl is evident.

BOTTOM: The bed of the ablation area. Left: View valley upward at an altitude of ca. 2270m asl. Right: Even where ground moraine is maximally eroded no bedrock is unearthed.

(Photos: Wäger 2008).

5.1.3 Reconstruction of the former glacier surface

Table 7 shows that the basic model assumption of a constant basal shear stress τ throughout the glacier is not fulfilled. This depicts the constraints of the automated model approach to reconstruct the former glacier surface. τ has a proportional effect on the thickness of the reconstructed glaciers with higher values resulting in thicker, and smaller values resulting in thinner glaciers. The semi-automatic reconstruction only accounts for variations in ice thickness due to differences in the bedrock slope, which obviously is a simplification. The advantage of this approach is the augmented objectivity compared to a wholly manual interpolation. However, an evaluation of the precision of the reconstruction is not possible (Imhof 2006, Schmidhauser 2007). The glacier surface for the 2D extents of both mapping scenarios was reconstructed by using the highest τ (1.04) as input parameter for the τ -model, because the cross section 2500 was considered to show the most original form with the highest ice thickness. In Figure 30, the reconstructed glacier surface, ice thickness and the resulting area/elevation distribution of the paleoglacier are shown for both mapping scenarios.

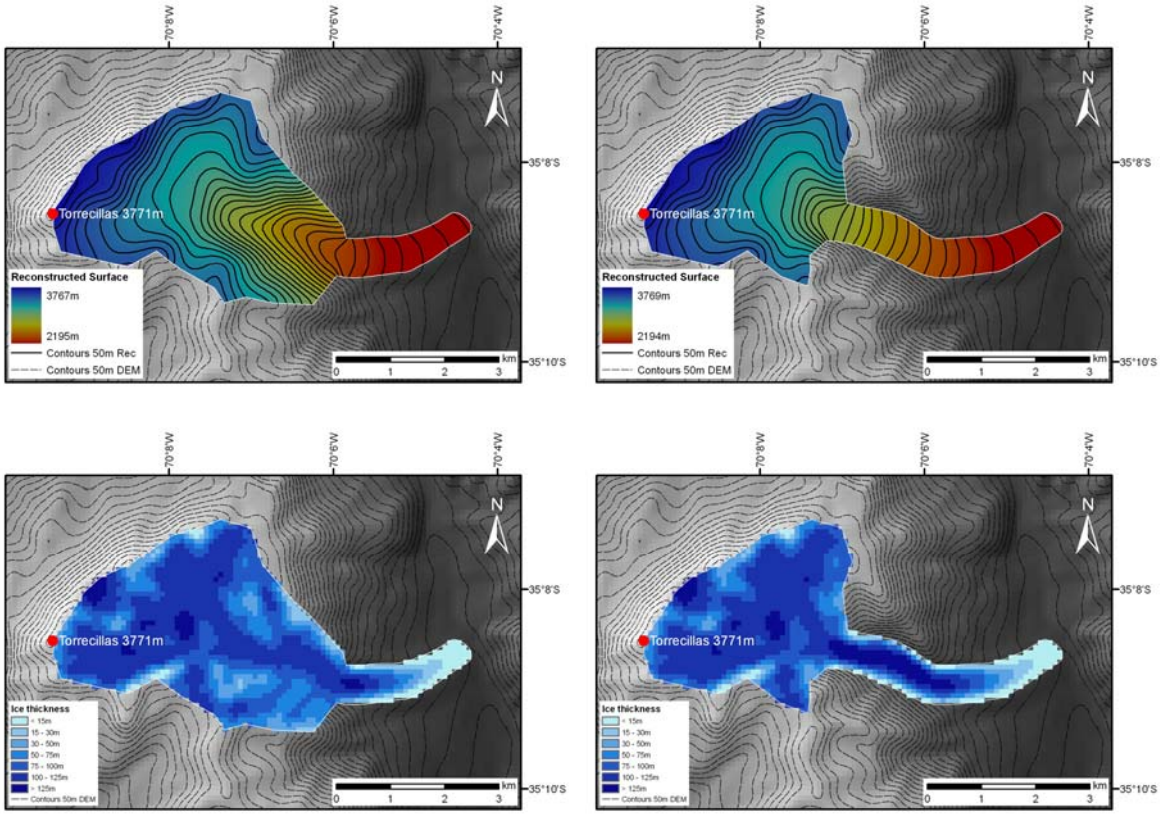

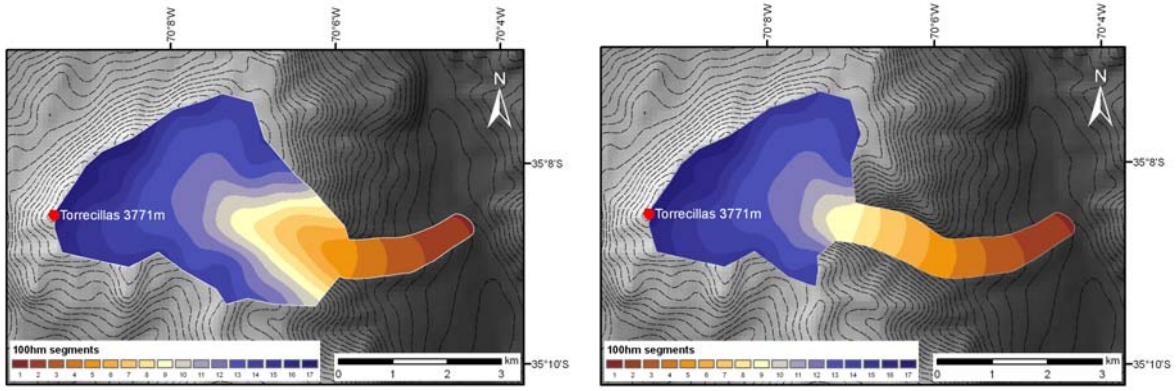

Figure 30. *The results of the reconstruction of the former glacier surface for both mapping scenarios, ELA_2500 (left) and ELA_3000 (right). TOP: The reconstructed former glacier surface. CENTER: Ice thickness. BOTTOM: The area/elevation distribution of the glacier in altitudinal segments of 100m equidistance.*

If compared to unglaciated landscapes, glacier surfaces are generally much smoother, especially in the accumulation area. In fact, the contours of the reconstructed glacier surfaces are smoother than the contours of the basic DEM of today's topography (Figure 30 top). The difference between the reconstructed surface and the basic DEM is the ice thickness (Figure 30 center). As expected, high ice thickness is found on gentle slopes, and low ice thickness where the terrain is steep. Values range from a few meters in the lowermost tongue area and close to the crests of the lateral moraines to more than 150m on flat terrain in the accumulation area. Mean ice thickness is 84m (ELA_2500) and 87m (ELA_3000) respectively. The reconstructed former ice surface was subdivided in altitudinal segments of 100m equidistance (Figure 30 bottom), which are the topographic input parameter for the glacier-climate model. The corresponding hypsometric curve and area per altitudinal segment are shown in Figure 31.

Figure 31: *Hypsometric curve (left) and area per altitudinal segment (right).*

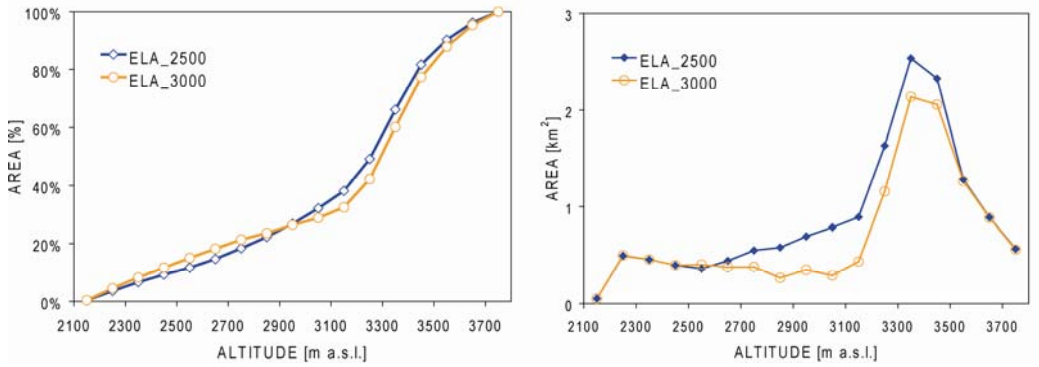

The hypsometric curve is similar for both mapping scenarios, with the bulk of the glacier area lying between ~3200-3700m asl, where the hypsometric curve exhibits a steep slope. The mapped area for both scenarios is almost identical in the lowest and uppermost part of the glacier area, but differs considerably in the medium part the mapped area, leading to a higher total area and a higher AAR for ELA_2500.

The exact values of the area/elevation distributions for both mapping scenarios and the resulting AAR values are summarized in Table 8. The AAR value of 0.91 for ELA_2500 is extremely high, and rather unrealistic. It results from the fact that the MELM is at only 2540m asl. Still, the AAR value of 0.74 for ELA_3000, where the ELA was artificially set to 3000m asl, is higher than the standard values shown in chapter 3.3. This is because the hydrologic catchment was considered as the former glaciated area in the in the accumulation area. Hence, the climatic information contained in the AAR values (3.3) must be critically looked at.

Mapping Scenario		ELA_2500		ELA_3000	
Altitudinal zone	h	Area [km^2]	Area [%]	Area [km^2]	Area [%]
2000 - 2100	0				
2100 - 2200	1	0.051	0%	0.051	0%
2200 - 2300	2	0.495	4%	0.497	5%
2300 - 2400	3	0.455	7%	0.454	8%
2400 - 2500	4	0.396	9%	0.396	12%
2500 - 2600	5	0.360	12%	0.402	15%
2600 - 2700	6	0.441	15%	0.375	18%
2700 - 2800	7	0.549	18%	0.377	21%
2800 - 2900	8	0.579	22%	0.265	24%
2900 - 3000	9	0.694	27%	0.348	26%
3000 - 3100	10	0.788	32%	0.289	29%
3100 - 3200	11	0.893	38%	0.432	33%
3200 - 3300	12	1.634	49%	1.159	42%
3300 - 3400	13	2.539	66%	2.138	60%
3400 - 3500	14	2.330	82%	2.057	77%
3500 - 3600	15	1.283	90%	1.267	88%
3600 - 3700	16	0.890	96%	0.887	95%
3700 - 3800	17	0.565	100%	0.558	100%
Total area		14.940		11.955	
Abl Area		1.397		3.166	
Acc Area		13.543		8.789	
AAR		0.91		0.74	

Table 8: *Area/elevation distribution and the AAR of the paleoglacier in Las Leñas for both mapping scenarios, ELA_2500 and ELA_3000.*

5.2 Modern local climate

The best guess climatic input parameters produced are shown in Table 9. In the following subchapters, the results of the calculation of the parameters precipitation, temperature and global shortwave radiation are presented in more detail. The climatic input paramters exhibit uncertainties that are difficult to quantify. However, the absolute modern values of the main control parameters (temperature and precipitation) are primarily used to assess the difference to the modeled paleoclimate conditions. This relativizes the importance of the absolute modern values.

Table 9: *Best guess modern climatic conditions in the study area at 2050m asl.*

	P [mm]		C [%]		T [°C]	W [m s^{-1}]	RH [%]	G [W m^{-2}]	DDF [-]
	sum	win	sum	win					
Ym (annual mean)	220	700	35	51	8.13	5.84	71	modelled	5.5
Ya (annual amplitude)	45	80	7	33	15.83	3.55	67		2.5
Da (daily amplitude)	not def[2]	-	not def[2]	-	11.43[2]	-	-		-
Grad (Lapse rate) [1]	9	3	0.84	0.84	-0.63	0.08	0.09		-0.09

[1] the lapse rates for precipitation, cloudiness, wind, relative humidity and the DDF were adopted from Kull (2002)
[2] Sinusoidal amplitude with max. convection and precipitation at 18:30 and max. temperature at 15:00 local time
Abbreviations of the parameters according to chapter 4.1.1 / table 1. Sum=summer; Win=winter

5.2.1 Precipitation

The bulk of annual precipitation in Las Leñas falls as snow in winter, and the mean (1952-2005) maximum snow water equivalent (MSWE) in Valle Hermoso is 805mm at 2275m asl (Masiokas et al. 2006). According to Espizua and Pitte (2009), annual precipitation at the Valle Hermoso meteorological station (35°S-70°12'W; 2294m asl) is about 940mm. In Las Leñas at 2240m asl, annual precipitation is 250mm (in water), and annual snowfall is 7m (personal communication from Jorge Torres, Las Leñas). Assuming a typical snow water equivalent (SWE) of 1mm per 1cm of snow, total precipitation accounts to 950mm, which is very close to the records from Valle Hermoso. However, technical limitations to precipitation measurements (instruments, extrapolation etc) must be kept in mind. For almost the whole Swiss Alps, effective precipitation differs by about 25% from the interpolated precipitation amount, for summer and for winter (Sevruk 1985, 2004). Figure 32 shows monthly mean precipitation for windward Los Queñes (CL) and leeward Malargüe (ARG). The longitudinal precipitation gradient, caused by the Andes, becomes obvious. At Los Queñes (annual

mean 1400mm), far more than 80% of the annual precipitation falls from Mai to September defining the main precipitation season. April and October/November can be seen as transition periods, whereas from December to March, precipitation is almost negligible. In Malargüe, total precipitation (350mm) is much lower and seasonality much less pronounced, with winter precipitation only slightly exceeding summer precipitation.

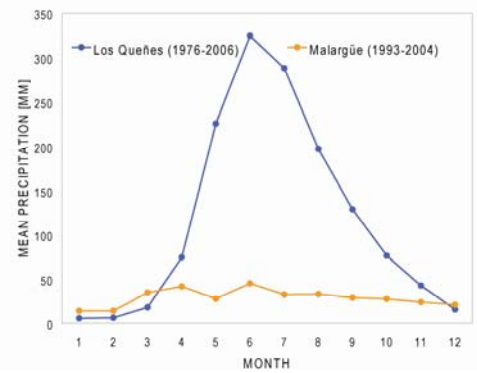

Figure 32: *Monthly mean precipitation for Los Queñes (800m asl) in Chile (windward) and for Malargüe (1416m asl) in Argentina (leeward). See Figure 1 for the location of the two stations.*

According to Jorge Torres (personal communication in 2008), precipitation in Las Leñas usually peaks in July/August. This is also supported from MODIS satellite pictures showing most regular front passages in the study area from May to September. In the model, precipitation in Las Leñas was defined as follows: Winter precipitation from the Westerlies falls from mid-April to mid-October, Summer precipitation from November to March. Both precipitation regimes are represented by sinusoidal functions with a much higher amount in winter (Figure 33).

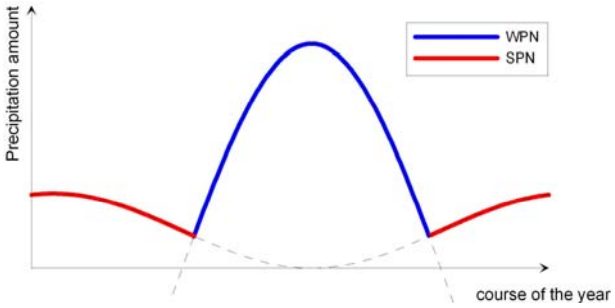

Figure 33: *Conceptual model for the representation of seasonality by sinusoidal functions for both precipitation types. Winter precipitation (WPN) with a maximum in mid-July, summer precipitation (SPN) with a maximum in mid-January.*

5.2.2 Temperature

From NCDC radiosonde measurements in Santo Domingo at the Chilean coast (33°40'S, 71°40'W), a mean temperature lapse rate of -0.63°C/100m was calculated. It shows only very slight seasonality as all monthly values range between -0.6 and -0.64°C. These values are very close to the values for the standard atmosphere of -0.65°C (e.g. Whiteman 2000) and the -0.7°C calculated from Brenning (2005) for the Andes of Santiago.

The temperature record from Malargüe Aero is the closest one to the study area in Las Leñas and shows the expected seasonal cycle for midlatitudes. Data from other stations in the region (San Carlos, San Rafael, Rama Caida) exhibit a consistent pattern (with higher temperatures due to lower elevations). At 1425m asl, annual mean temperature in Malargüe is 12.3°C and annual amplitude over 15°C. Thereby, the highest values occur in January (19.8°C) and the lowest ones in July (4.6) (Figure 34 left). By applying the calculated temperature lapse rate of -0.63°C/100m, monthly mean values from Malargüe were reduced to 2050m asl, the base height of the model. The resulting annual mean is 8.32°C (Figure 34 right).

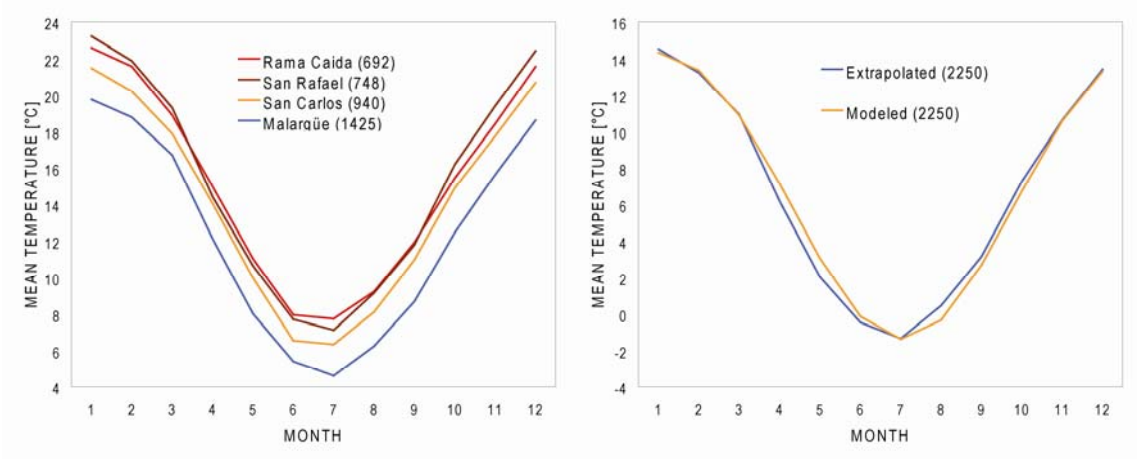

Figure 34: *Left: Monthly mean temperature at several Argentinian stations in the Andean foreland (34°30'-35°60'S). Right: Monthly mean temperature in Las Leñas at 2250m asl when extrapolating the temperature data from Malargüe by applying the calculated temperature lapse rate (description in the text) (Extrapolated) and the modeled monthly mean temperature in the glacier-climate model (Modeled).*

Obviously, this way of evaluating modern temperatures in the study area is very simplistic. However, it is possible to introduce further data from the literature: Mean monthly temperature at the Valle Hermoso meteorological station are known to be below 0°C from June to August (Espizua & Pitte 2009). When reducing temperature from Malargüe to Las Leñas at 2250m, monthly mean temperature is only negative in July. By applying a slightly lower annual mean, monthly mean temperatures are below 0°C from June to August. That way it can be guessed that on-site temperatures are better approximated, at least in winter.

The resulting 0°C isotherm of the mean annual air temperature (MAAT) in Las Leñas is around 3300m asl, which is lower than the 3600m asl estimated from Brenning (2005). However, Brenning's estimation is valid for the Andes of Santiago (~33°S) and the height of the 0°C MAAT decreases towards south (Figure 15). This gives further confidence to the way how air temperature in the study area is modeled.

Figure 35 shows the relative frequency distribution in percentage of the daily amplitude (data for 12/2006 - 11/2007). During this period, a daily amplitude of 12°C was exceeded only on six days. By analyzing other data of the CAND-stations (snow height, wind), and by referring to MODIS pictures, these high values could likely be attributed to changes in the mesoscale airflow (e.g. passages of cold fronts). A maximum potential daily amplitude of 11.43 was calculated by taking the mean of the five highest values below 12°K. This value is close to the daily amplitude of 12°C measured on Cerro Tapado (30°S) (Kull et al. 2002).

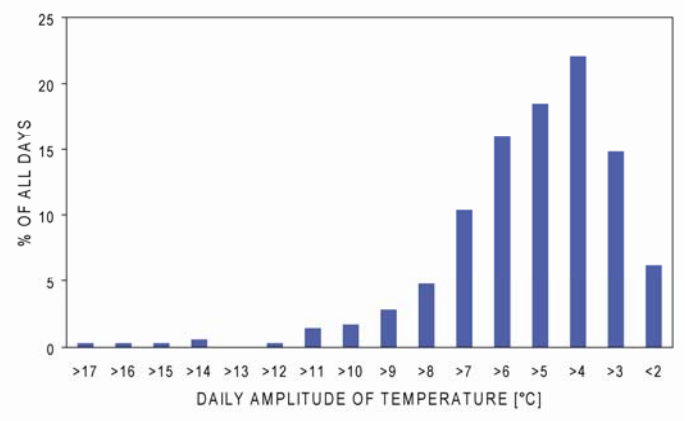

Figure 35: *Frequency distribution in % of the daily amplitude of temperature at CAND2 (12/06-11/07, total 358 days.*

5.2.3 Global shortwave radiation

Global shortwave radiation was modeled for 0 and 35 ka BP, different cloudiness scenarios (0=no cloudiness, A=cloudiness according to modern precipitation, B=cloudiness when doubling modern winter precipitation, C=cloudiness when tripling modern winter precipitation, Table 6) and the two mapping scenarios ELA_2500 and ELA_3000.

All modeling results are summarized in Appendix II. The modeled potential global shortwave radiation for 0 and 35 ka BP and the modeled global shortwave radiation under different cloudiness scenarios for 35 ka BP are shown in Figure 36. As the study area lies out of the tropics, global shortwave radiation exhibits the expected seasonal cycle with a maximum in December. Absolute differences in potential global shortwave radiation between 0 and 35 ka BP are small with annual means of 6.68 (0 ka BP) and 6.58 kwh/m^2*d (35 ka BP). However, there is a difference in the seasonality. At 35 ka BP, perihelion was in June, today (0 ka BP) it is in January. Hence, seasonality was less pronounced on the Southern Hemisphere at 35 ka BP than today 0 ka BP, leading to relatively lower incoming radiation in austral summer and relatively higher incoming radiation in austral winter. This is consistent with reconstructed insolation values (Berger & Loutre 1991).

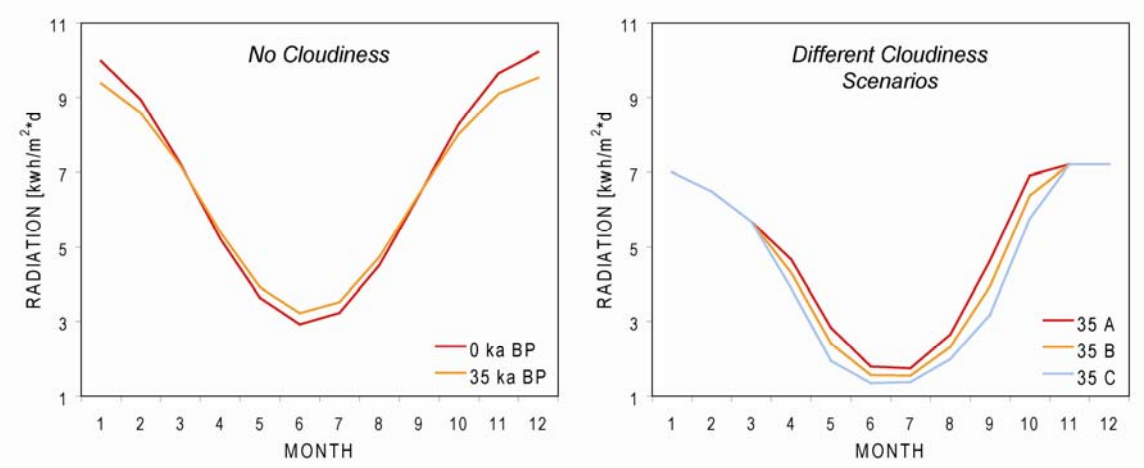

Figure 36: *Monthly averaged modeled global shortwave radiation on the mapped extent of Las Leñas paleoglacier under the mapping scenario ELA_2500. (Left) Potential global shortwave radiation for 0 and 35 ka BP. (Right) Global shortwave radiation under different cloudiness scenarios for 35 ka BP.*

In Figure 37, the modeled global shortwave radiation on the reconstructed glacier surface is shown. The pattern for 0 and 35 ka BP are very similar, with slightly lower values in austral summer for 35 ka

BP than for 0 ka BP. In January, where solar altitude is high, lowest global shortwave radiation values are observed where slope is high (Figure 37 top). In July, where solar altitude is low, lowest global shortwave radiation values are found in southward exposed slopes (Figure 37 center). As expected, the values decrease with increased cloudiness (Figure 37 bottom).

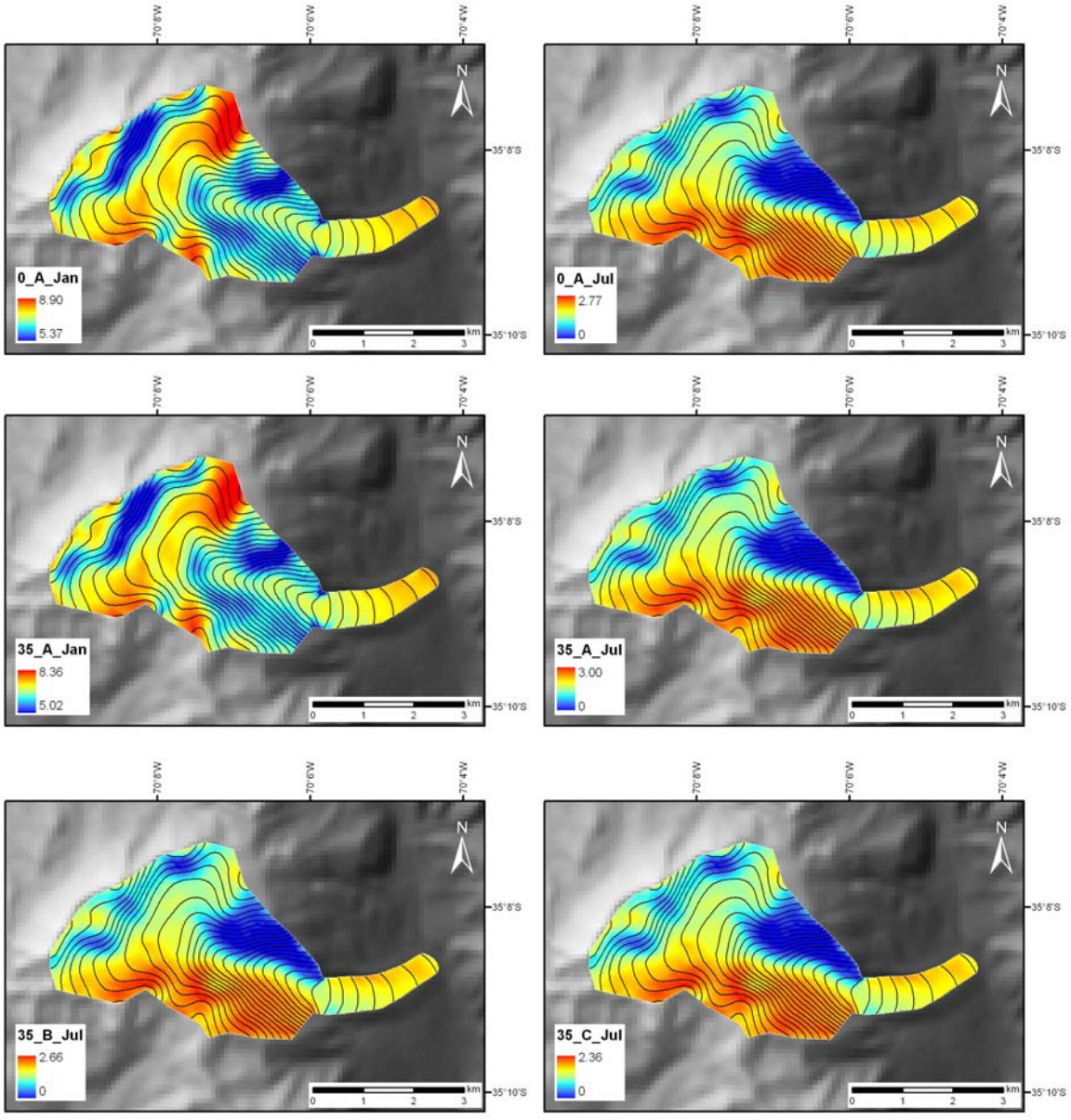

Figure 37: *Global shortwave radiation [kwh/m^2*d] on the reconstructed former glacier surface of Les Leñas paleoglacier. TOP: For 0 ka BP and cloudiness scenario A in January (left) and July (right). CENTER: For 35 ka BP and cloudiness scenario A in January (left) and July (right). BOTTOM: For 35 ka BP and July for cloudiness scenarios B (left) and C (right). Note that the colour ranges of the different pictures is not uniform.*

5.3 Glacier-climate modeling

First, the glacier-climate model is run with modern climate (chapter 5.3.1) data for two reasons: (1) Under modern climate conditions, no glacier exists in the study area that could provide information about modern ELA. By applying the glacier-climate model, the ELA can be modeled; (2) By comparing the modeled ELA with the regional ELA pattern, the suitability of the model can be validated. Under the assumption of the actualistic principle, the model fits to reconstruct paleo glacio-climatological conditions (chapter 5.3.2) if it reasonably reproduces modern glacio-climatological conditions.

5.3.1 Modern glacio-climatological conditions

Annual and seasonal mass balances under best-guess modern local climate conditions are shown in Figure 38. Because the study area is not glaciated today, a modern ELA is only hypothetical. The modeled annual ELA is at ~3950m asl, almost 200m higher than the highest point of the study area. Seasonal ELAs are ~2950m asl in winter and over ~4300m asl in summer. Mass balance gradients in summer are much higher than in winter. The main ablation process in summer up to 4000m asl is melt, which is driven by positive air temperatures.

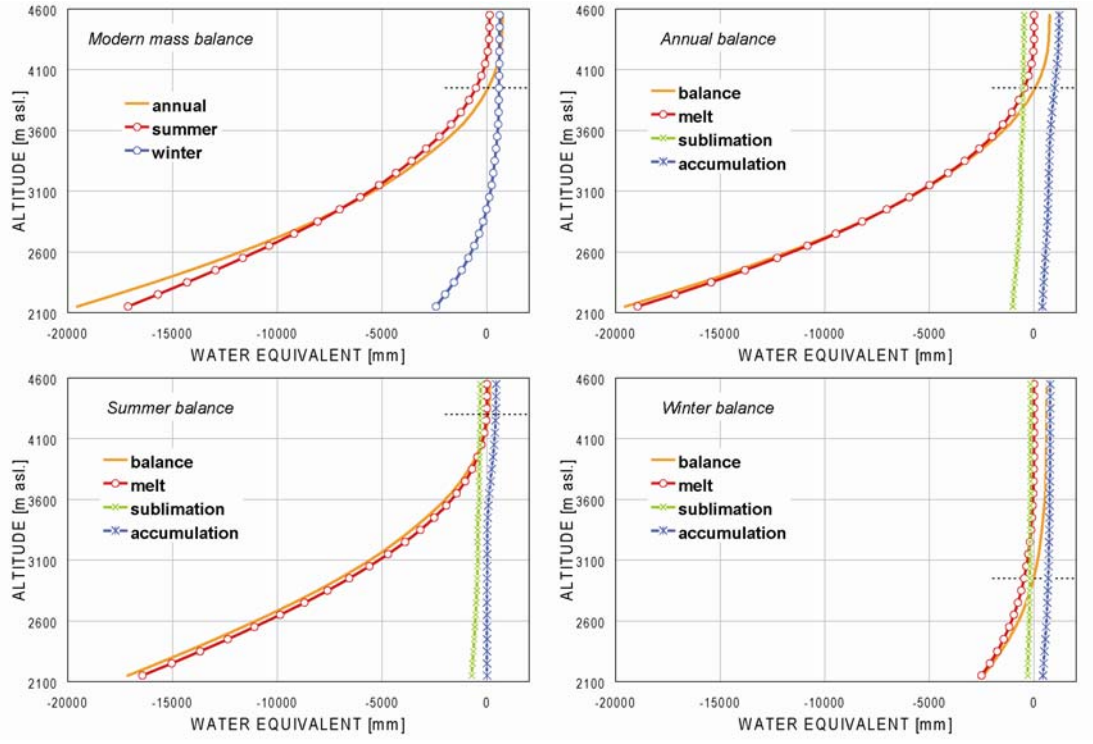

Figure 38: *Modeled annual and seasonal mass balance under modern conditions.*

In winter, melt is only important for the lowest elevations of the study area. Ablation by sublimation is far less important. In summer, only very little accumulation occurs above the 0°C MAAT, around 3300m asl, whereas in winter, accumulation occurs throughout the whole vertical extent of the glacier. In summary, these modeled glacio-climatological conditions fit well to the observations (chapter 2.3.2). Therefore, it can be concluded that the model also fits to investigate paleo glacio-climatological conditions.

5.3.2 Paleo glacio-climatological conditions

5.3.2.1 2D-Modeling

Considering only the surface of the former glacier, equilibrium state is reached if the total averaged annual mass balance over the whole glacier surface is zero (chapter 4.1.4). When tuning only temperature and precipitation, while all other parameters are held constant, several precipitation/temperature (P/T) combinations provide a numerical solution. The resulting combinations of change in precipitation (dP) and change in temperature (dT) (from here on called dP/dT solutions) in the best guess input scenario are shown in Figure 39. dP and dT are related to modern conditions in the study area at 2050m asl (Table 9). Summer precipitation is held constant at the modern level, and the entire possible precipitation increase is due to increased winter precipitation according to the hypothesis of this study.

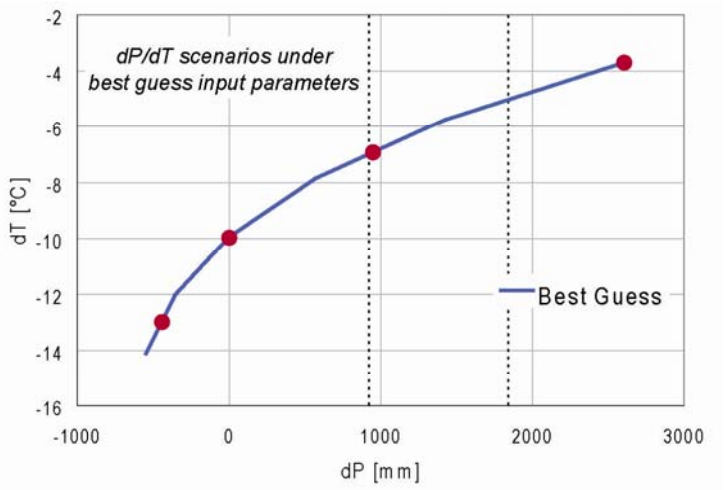

Figure 39: *dP/dT solutions for a glacier in equilibrium state in 2D under best guess input parameters. Any point on the curve represents a theoretically possible solution. The dotted vertical lines indicate where modern precipitation (920mm, dP=0) is doubled (1840mm, dP=920) and tripled (2760mm, dP=1840). The red dots show the dP/dT solutions which are plotted in more detail in Figure 40.*

Obviously, the dP/dT relation is non-linear, and the dP/dT solutions range from extremely cold and dry to temperate and extremely humid. With increasing temperature, precipitation increases disproportionally. Whereas the glacier reacts very sensitively to changes in temperature in a cold-humid climate, precipitation is the stronger driver in a cold-dry climate. The strong temperature depression (dT) needed to reach equilibrium state in 2D is striking. Under modern level precipitation, dT must be ~10°C. When doubling modern precipitation, the dT needed is ~7°C, and still ~5°C when tripling modern precipitation. For the P/T solutions indicating a precipitation increase, one should always keep in mind the importance of redeposition of snow (chapter 2.3.2). While snowdrift is important under modern level precipitation, it can be guessed that it was even more important the higher the effective precipitation was.

Every dP/dT solution lying on the curve in Figure 39 leads to different mass balance/elevation distributions. In Figure 40, they are plotted for four different dP/dT solutions. Highest mass balance gradients in the ablation area of the glacier are observed under temperate and extremely humid conditions (red line) lowest ones in a extremely cold and dry climate (blue line). This is because higher temperatures produce more ablation by melt, which is much more important than ablation by sublimation. The resulting pELA (dashed lines) range between 2880m asl (under extremely cold and dry conditions) to 3080m asl (under temperate and extremely humid conditions), implying a depression of ~870 - 1070m from the modern ELA.

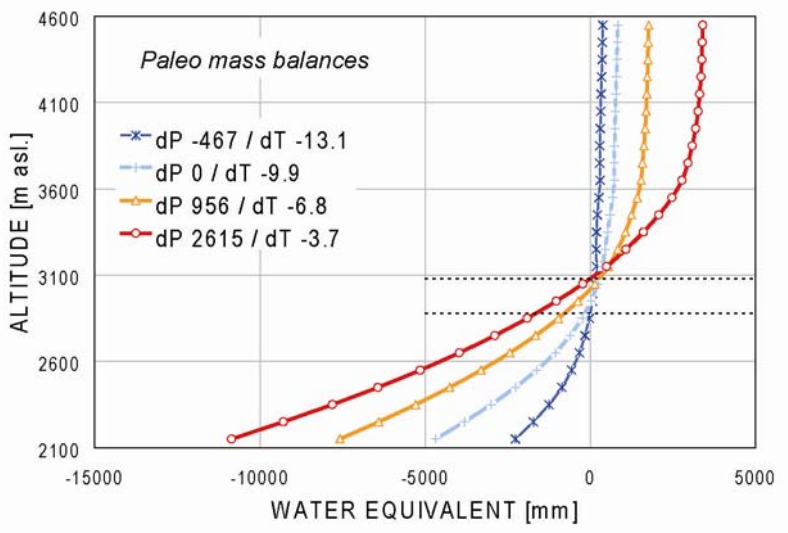

Figure 40: *Mass balance/elevation distribution for four different dP/dT solutions (red dots in Figure 39) ranging from extremely cold and arid (blue) to temperate and extremely humid (red). The dashed horizontal lines indicate the resulting highest and lowest pELA.*

The climatic input parameters were created based on best-guess assumptions, and the corresponding uncertainties are difficult to quantify. To assess the robustness of the results of the best-guess scenario, the model was also run for different scenarios, where in each case one parameter was modified (Figure 41) and compared to the best-guess scenario (*BG*, the blue line all Figures). Results are shown for the alternative mapping scenario (Figure 41A), for scenarios with varied climatic input parameters (Figure 41B-F) and for all scenarios together (Figure 41H). The variation of the climatic input parameters concerns temperature gradients (B), precipitation gradients (C), cloudiness (D), precipitation cooling degrees (E) and degree-day factors (F). The results are also plotted for a varied precipitation source (G), where the entire precipitation (SP_only) or the entire precipitation increase (SP_increase) is attributed to the summer precipitation. All these results are summarized in Appendix III, where not only the dP/dT solutions are listed, but also the attributed absolute precipitation and temperature, the temperature and precipitation at the ELA, the pELA and the corresponding ELA depression, the AAR and the mass balance gradient in the ablation area.

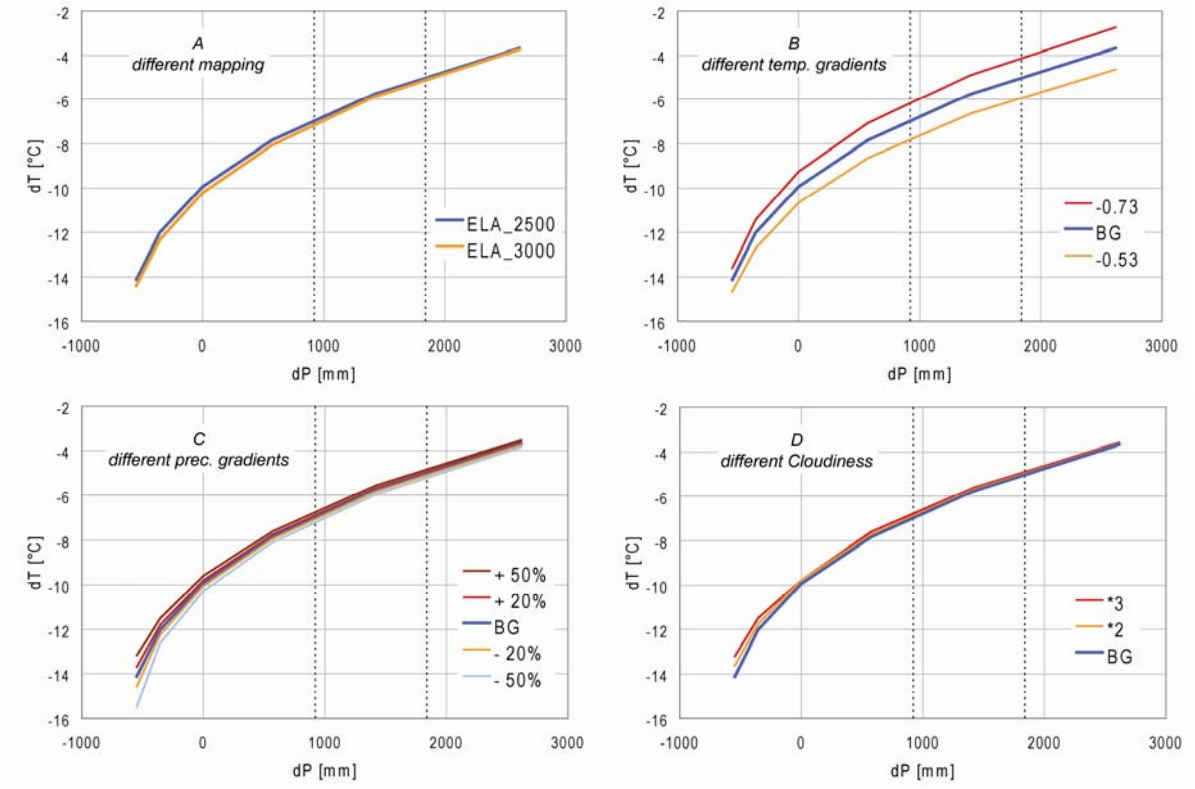

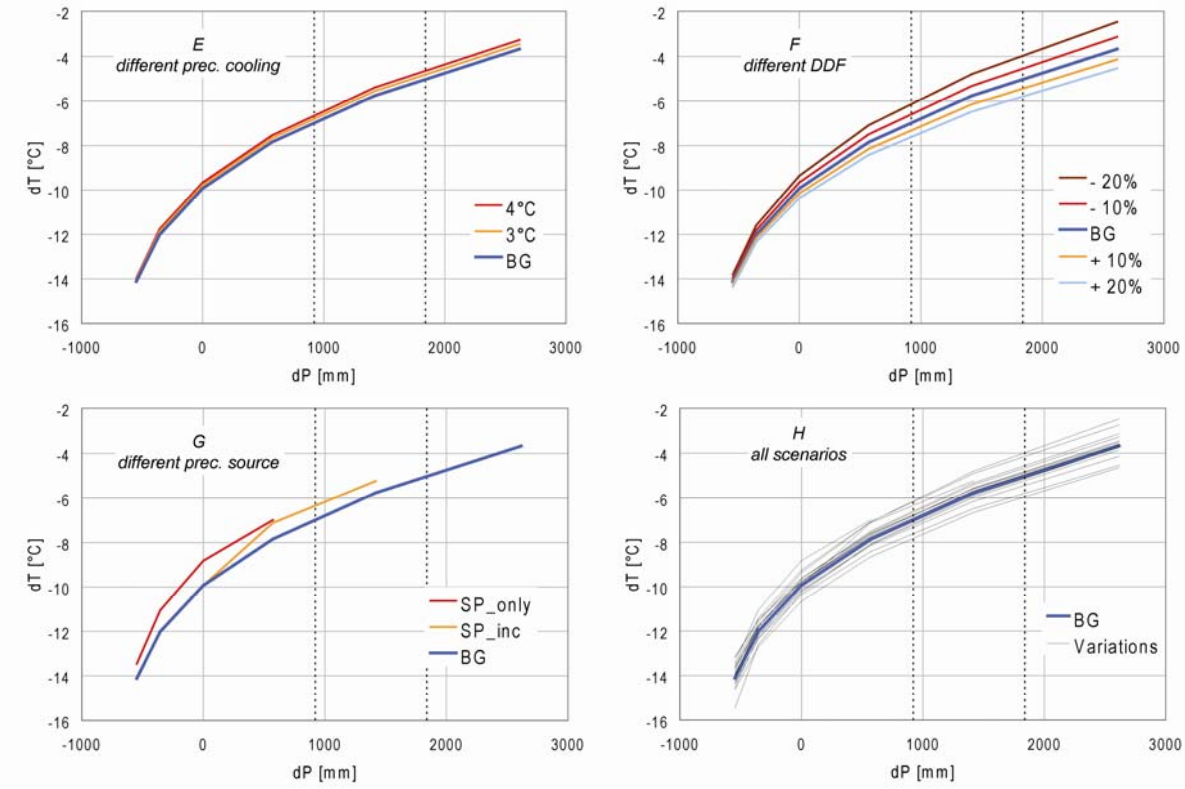

Figure 41: *dP/dT solutions for a glacier in equilibrium state in 2D, when the alternative mapping scenario ELA_3000 is applied (A) and when different climatic input parameters are varied (see description in the text) (B-G). Finally, the best guess scenario is compared with all the scenarios with varied input parameters (H).*

Obviously, the impact resulting from variations of the best-guess scenario differs strongly depending on which parameters are varied. The uncertainties in mapping, cloudiness, precipitation gradients and precipitation cooling are almost negligible. Different temperature gradients and degree-day factors affect the resulting dP/dT solutions more strongly, which is also true for a different precipitation regime. It should be noted that the curves in a scenario with prevailing summer precipitation are limited by the maximal possible summer precipitation, when summer precipitation is parametrized according to Kull (1999).

However, when plotting all the different variations and the best-guess scenario (Figure 41H), a similar pattern of all curves can be distinguished. For all scenarios, a distinctive temperature depression is needed, which attains ~9-10.5°C under modern level precipitation, dropping to ~6-8°C when doubling and ~4-6°C when tripling modern precipitation.

5.3.2.1 3D-Modeling

Despite of the problems encountered during the analysis of the cross sections in the ablation area (chapter 5.1.2), the 3D modeling was tentatively carried out. In Figure 42, the DMM (the difference between mass influx into a cross sections and the total mass balance below the cross section) for the three cross sections are shown as a function of dP resulting from the 2D modeling in the best guess scenario (with polygonic shape and standard flow parameters) are shown. If, in addition to a total averaged mass balance of the glacier (condition 1, 2D modeling), also condition 2 (DMM=0 for at least two cross sections in the ablation area, 3D modeling) should be fulfilled, the DMM values of the cross sections should intersect at DMM = 0.

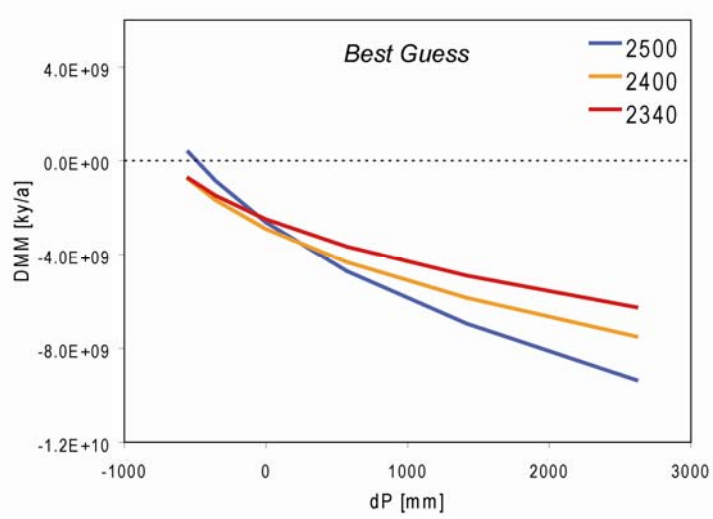

Figure 42: *Best guess ice flow characteristics (DMM) through three cross sections at 2500, 2400 and 2340m asl as a function of the change in precipitation permitting an equal mass balance over the whole glacier surface resulting from the 2D modeling.*

Obviously the resulting DMM values are all negative except for cross section 2500m asl in an extremely cold and dry climate. With increasing precipitation, the DMM values become stronger negative. This is because with increasing precipitation, temperature also increases, leading to higher ablation rates due to higher melt in the lowest part of the glacier. Obviously, the best guess input parameters do not allow a successful 3D modeling. Negative DMM values result from too low mass influx, too high ablation below the cross section or a combination of both aspects. Therefore, the best guess input scenario is varied to increase mass flux or decrease ablation, in order to investigate the sensitivity of the results (Figure 43). Ablation below the cross section can be decreased with (1) lower

sublimation rates due to lower wind speed, lower vapour pressure deficit and lower global shortwave radiation or (2) lower melt rates due to lower temperatures and a lower DDF. As shown in chapter 5.3.1, ablation by sublimation is far less important than ablation by melt. Ablation by melt can only be decreased if a lower DDF is applied, because under lower temperatures (when holding precipitation at the same level), condition 1 (averaged mass balance over the whole glacier area) would not be fulfilled any more. A lower DDF (-20%) was applied. The resulting DMM values show that ablation is slightly decreased but, in general, still far higher than mass influx. An even lower DDF would not be realistic.

As a consequence, mass influx must be enormously increased. This is possible with (1) a higher form correction factor F due to a higher cross section area (or a different shape), higher ice thickness or higher bed slope, or (2) higher than flow parameters. A trapezoidal shape was applied, as well as a very high form correction factor F of 0.9 (the form correction factor must be between 0 and 1). Furthermore, the values of the standard flow parameters were doubled. By varying the mentioned input parameters, the curves are displaced towards more positive (less negative in most cases) DMM values. Nevertheless, DMM values especially for the cross sections at 2400 and 2340 m asl are still negative at almost any dP level, and the different curves do not intersect at DMM = 0. It becomes obvious that the geometrical uncertainties expressed in chapter 5.1.2 impede a successful 3D modeling

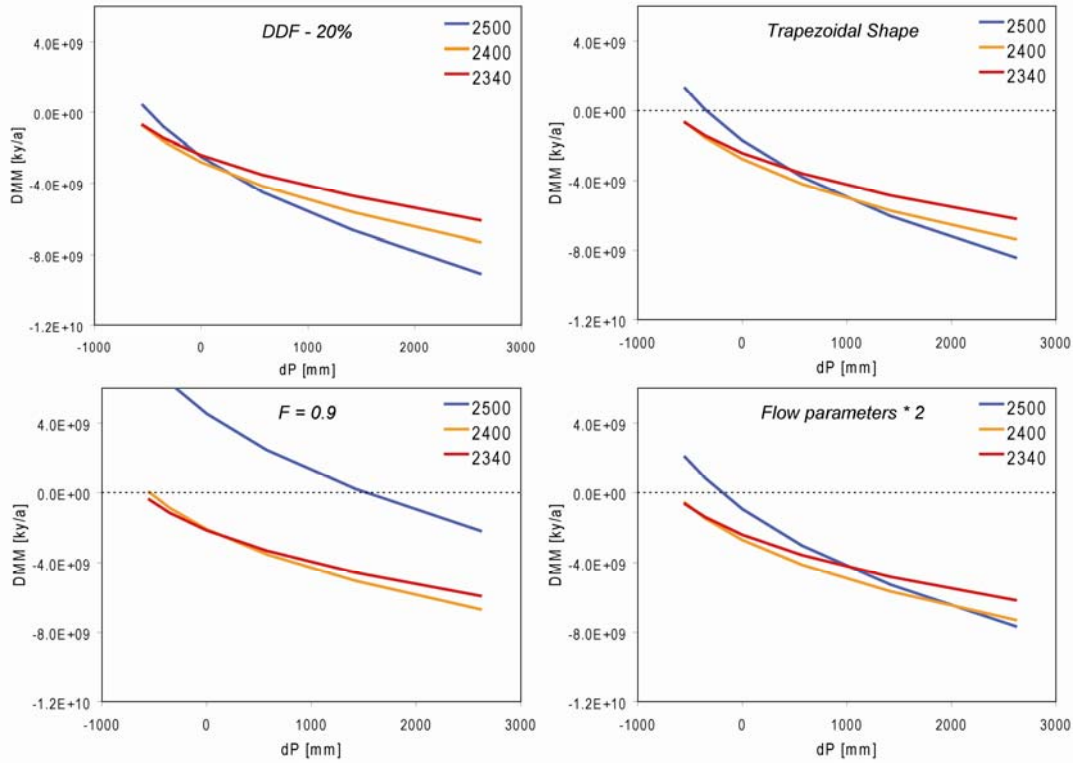

Figure 43: *As Figure 42, but with different mass balance (DDF - 20%) and ice flow scenarios (trapezoidal cross section shape, shape factor = 0.9, flow parameters * 2).*

6 Discussion

Almost all previous studies working with the glacier-climate model from Kull (1999) were situated in regions with prevailing convective summer precipitation, and one of the basic assumptions was that a possible increase in precipitation resulted from intensified convective summer precipitation. The only study in an arid to semiarid winter precipitation regime was located in Northern Chile around 29-30°S (Kull et al. 2002). The empirical-statistical model linking summer precipitation to cloudiness was developed in the arid Central Andes, which is also the case for the empirical-statistical models describing the mass balance terms melt, sublimation and accumulation. By applying the glacier-model to the paleoglacier in Las Leñas (35°S), lying at the edge of the subtropics to midlatitudes in the Southern Central Andes where winter precipitation prevails, the southernmost study site so far has been established in the present study. Only slight adjustments to a semiarid to humid winter precipitation regime turned out to be necessary in the glacier-climate model. They concerned the correction terms for winter precipitation and winter (chapter 4.1.6).

The purpose of this study was (1) to investigate if the glacier-climate model also fits to reconstruct paleo glacio-climatological conditions in a region with prevailing winter precipitation; (2) - if the model is found to be suitable - to determine paleo glacio-climatological conditions in the study area and (3) to discuss the paleoclimatic implications of the findings. This study works with the hypothesis that the LLGM advance in Las Leñas was reached in late Pleistocene, but pre-LGM times around 35 ka BP, and triggered by a humidity pulse from intensified Westerlies in combination with a low temperatures during full glacial times.

In this chapter, the modeling results are discussed. By assessing if modern glacio-climatological conditions are realistically modeled, the suitability of the glacier-climate model for reconstructing paleo glacio-climatological conditions is evaluated (6.1). No 3D modeling could successfully be carried out in the present study, and the 2D modeling indicate that a broad range of P/T solutions could theoretically have produced an equilibrium state of Las Leñas paleoglacier. However, we try to narrow down the theoretically possible to the most probable range of paleoclimatic conditions (6.2). Finally, the resulting paleoclimatic implications are discussed both in respect of glacier chronologies and atmospheric circulation systems during the LLGM in Las Leñas (6.3).

6.1 Modern glacio-climatological conditions

Modern glaciation in the study area is particularly determined by the distribution of incoming solar radiation and the redeposition of snow from the predominant Westerlies. As a consequence, almost all modern glaciers in the study area lie in shadowy steep slopes with S to SE expositions (chapter 2.3.2). The glacier-climate model does account for variations in incoming solar radiation, but not for the redeposition of snow according to the main wind direction. However, it can be argued that the redeposition of snow is also reflected in the local precipitation data used as climatic input parameters in this study.

When parametrized with modern climatic data, the slightly adapted glacier-climate model put the modern annual ELA to ~3950m asl, the winter ELA to ~2950m asl and the summer ELA to over ~4300m asl. As expected, the mass balance modeling shows that ablation by sublimation is far less important than in the previous studies in the subtropics. The dominating ablation process in summer is melt, and this is also true for the lowest elevations of the paleoglacier during winter. While accumulation in winter occurs over the whole area of the paleoglacier, it is only minor in summer, and then restricted to elevations above the elevation of 0°C MAAT, which is modeled to ~3300m asl.

The modeled modern ELA at ~3950m asl in the catchment of the study area fits well into the established regional ELA pattern (chapter 2.3.2), where the local ELA was expected to be between ~3900 - 4100m asl Also the seasonal distribution of the mass balance terms is reasonable for the prevailing climatic conditions in the study area. This gives confidence to the parametrization of the climatic input parameters, but also to the empirical-statistical mass balance models in the glacier-climate model. We note that modern glacio-climatological conditions are suitably reproduced by the glacier climate model and conclude that, according to the actualistic principle, the glacier-climate model is also suitable to investigate paleo glacio-climatological conditions in the study area.

6.2 Paleo glacio-climatological conditions

The geometrical uncertainties did not allow a successful 3D modeling. However, the 2D modeling provides robust results for paleo glacio-climatological conditions even when important input parameters are strongly varied. The dP/dT solutions producing a glacier in equilibrium state in 2D range from extremely cold and dry to temperate and extremely humid conditions. For most of the dP/dT solutions, a distinct temperature depression is indicated. Furthermore, solutions with dT ≥10°C go along with a precipitation increase. From the modeling perspective, it is not possible to exclude that the precipitation increase could also have been caused by increased summer precipitation. However, the exposition of the catchment of Las Leñas paleoglacier implicitly indicates that the Westerlies were

the main precipitation source. Here, we try to locate the most plausible range of dP/dT solutions within all modeled ones by looking at the glacier traces and the modeled geometry, but also by comparing the modeling results to reconstructed late Pleistocene climate conditions from other proxies in the broader region of the study area. For the dP/dT solutions indicating a precipitation increase, one should always keep in mind the importance of redeposition of snow. While this process is important under modern level precipitation falling predominantly from the Westerlies, we speculate that it was even more important the higher the effective precipitation was. However, it is not possible to quantify the importance of snowdrift for local annual precipitation.

6.2.1 Geomorphology and Geometry

The AAR is an important glaciological parameter depending on climate conditions (chapter 3.1). When analyzing AAR values in the present study, one has to keep in mind that there are mapping uncertainties, because the lateral moraines have been eroded above ~2500m asl (chapter 5.1.1). Mapping uncertainties automatically lead to uncertainties in the AAR values. As shown, the AAR for both mapping scenarios are very high and rather unrealistic. Nevertheless, it is proposed that the AARs can provide qualitative information about the prevailing paleoclimatic conditions during the LLGM advance. The pELA and the AAR are plotted against the precipitation change (dP) corresponding to the modeled dP/dT solutions for the best guess scenario (blue curves) together with scenarios with varied temperature gradients (Figure 44 left) and together with the ELA_3000 mapping scenario (Figure 44 right). The plots indicate that, with increasing precipitation within the dP/dT solutions, the ELA raises and the AAR decreases.

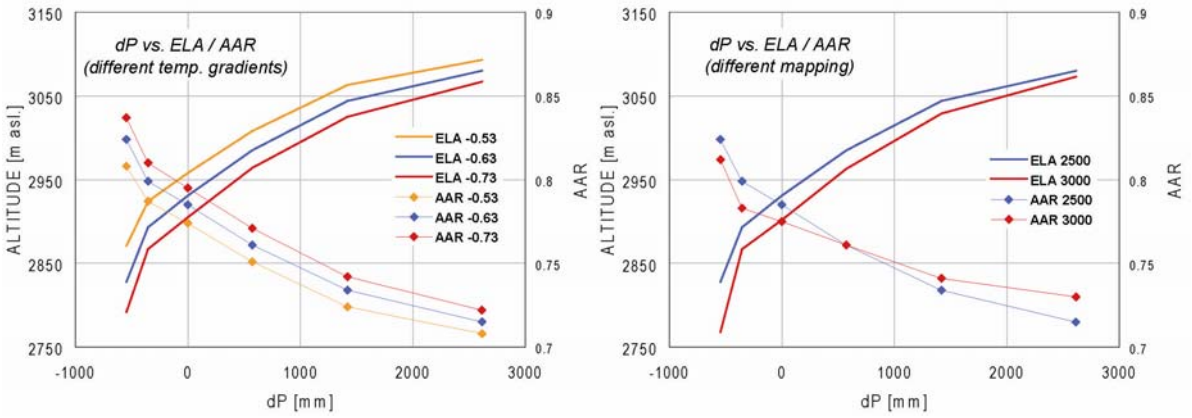

Figure 44: *ELA and AAR for the best guess dP/dT solutions (blue curve) and the dP/dT solutions when varying the temperature gradient (left) or the mapping scenario (right).*

Prima facie, this seems to be in contradiction to the general observation that warm-humid climate conditions produce a low ELA and a high AAR, and that cold-dry climate conditions produce a high ELA and a low AAR. However, as the present study bases on an observed, fixed geometry, higher precipitation and higher temperatures *must* lead to an pELA raise, resulting in a lower AAR. For any scenario with varied input parameters, the resulting pELA is between ~2770 - 3090m asl (Appendix V), implying a depression of ~860 - 1180m from the modern ELA (~3950m asl). This is comparable to the ELA depressions of ~900-1000m from most previous studies in the arid Central Andes (Kull 1999, Kull & Grosjean 2000, Imhof 2006, Schmidhauser 2007) and from the Chilean Lake District (Denton et al. 1999a). As expected, the highest pELA and therefore lowest AAR is found for the climate scenario with the lowest temperature gradient (-0.53°C/100m), where the elevation of the MAAT 0°C is highest. The three scenarios varying only in the temperature gradient show a similar behaviour in the pELA and the AAR (Figure 44). Due to the different area/elevation distribution of the paleoglacier (chapter 5.1.3), this is not the case for the two different mapping scenarios. The alternative mapping scenario ELA_3000 has a lower AAR in cold-dry climates than the best guess scenario ELA_2500, but this pattern reverses in cold-humid climates. However, the values exhibit only minor differences.

Again, all the AAR values are very high compared to the standard values (chapter 3.1). Under cold-dry to cold-humid climate conditions, AAR values higher than ~0.75 are rather unprobable. By plotting the AAR against climate conditions at the ELA, different glaciers can be compared to each other. AAR values attributed to the dP/dT solutions in the best guess scenario are plotted against precipitation (Figure 45 left) and temperature (Figure 45 right) at the ELA (P_ELA and T_ELA) and compared to the paleoglaciers in the arid Central Andes reconstructed in earlier studies (references in chapter 1).

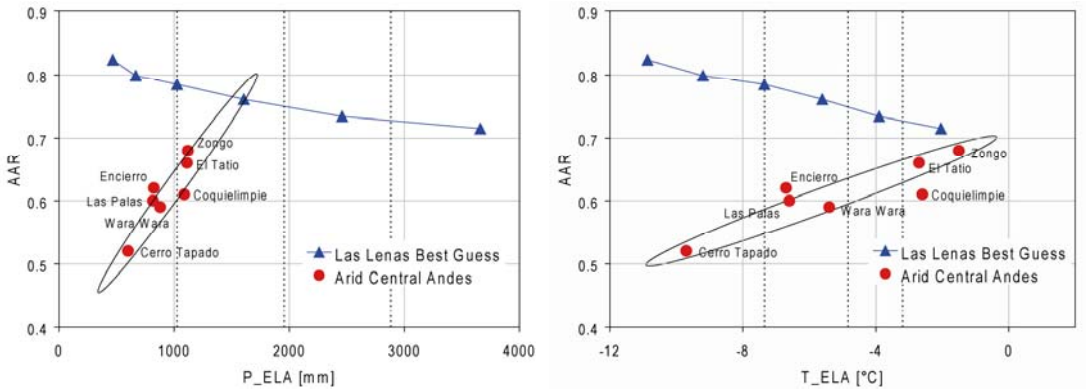

Figure 45: *AAR values depending on precipitation at the ELA (P_ELA) and temperature at the ELA (T_ELA). For the values from previous studies, approximate trends are sketched in (black ellipse). Dashed vertical lines indicate a modern level, a doubling and a tripling of modern level precipitation.*

Results from the previous studies indicate that AAR values increase with increasing precipitation and increasing temperatures. In Figure 45, the corresponding trends are qualitatively sketched in (black ellipse). Again, the AAR values modeled in this study are very high, and again, they run contrary to the trend of the previous studies in the arid Central Andes due to the bond to a fixed geometry. Provided that the qualitative relationships AAR/P_ELA and AAR/T_ELA are also valid for the conditions in Las Leñas, the "correct" dP/dT solution would be where the trends (for both relationships) and the line connecting the modeled AAR values in this study intersect. There is an intersection in the AAR/P_ELA diagram, lying at an AAR level of ~0.76-0.77. The corresponding climate exhibits cold-humid conditions with P_ELA of ~1500-1700mm, implying an increase by more than 50% from modern annual precipitation. On the other hand, there is no intersection in the AAR/T_ELA diagram, but the trend is approached with increasing temperatures. When analyzing these relationships, one has to keep in mind that (1) the present study lies in different precipitation and climate regime; (2) there are mapping uncertainties in the present study and (3) P_ELA and T_ELA are autocorrelated for a fixed extent. Therefore, only qualitative conclusions are derived from Figure 45. Nevertheless, it becomes obvious that the high AAR modeled for extremely cold and arid climatic conditions (below modern precipitation level) are rather unrealistic.

This is also generally supported by the massive moraines found in Las Leñas, which can hardly be attributed to cold glaciers with low mass turnover. From the evidence assembled in this chapter, we follow that an LLGM advance under extremely cold temperatures in combination with precipitation below the modern level are rather unprobable. The LLGM advance was rather triggered by a cold and humid (AAR/P_ELA) to a temperate and extremely humid climate (AAR/T_ELA).

6.2.2 Reconstructed late Pleistocene climate in other proxies

A distinct temperature decrease and a likely humidity pulse in late Pleistocene times as indicated by the geometry in the previous chapter is also found in many proxies from Central Chile. Here, the most important reconstructions of late Pleistocene paleoclimate in Central Chile (as shown in chapter 2.4.3.3) are sketched and then compared to the dP/dT solutions for the LLGM advance in this study.

6.2.2.1 Temperature

A recent modeling study of the Southern Westerlies during LGM (Rojas et al. 2009) indicates a temperature depression of 8-10°C for South America. Paleovegetation studies in Central Chile indicate temperature depressions of ≥7°C (35°S, Heusser 2003), 6-7°C (40°S, Moreno et al. 1999) and 6-8°C (40-43°S, Heusser et al. 1999). After the termination of the last glaciation at ~17-18 cal ka BP, a slightly cooler and wetter than modern climate established, accounting for a total temperature recovery

of >5°C by ~16 cal ka BP. A slightly cooler climate prevailed in the Lateglacial from ~14-11 cal ka BP, but the cooling was minor (≤3°C) (Heusser et al. 1999, Moreno et al. 1999, Moreno et al. 2001). If existing at all, regional temperature reconstructions going further back than the LGM are not precise. However, from the information from polar ice cores on both hemispheres (chapter 2.4.3.3), we conclude that temperature depressions during MIS4 were comparable to MIS2, and that also MIS3 was cold, although exhibiting stronger fluctuations, especially evident in the Greenland cores, but also in Antarctica.

6.2.2.2 Precipitation

The LGM simulation of the Southern Westerlies of Rojas et al. (2009) point to increased storm activity in winter in midlatitudes (25-45°S), and many proxies in central Chile indicate more humid conditions during the last glaciation. However, there is no general agreement about the timing of the humid phases (Figure 46). It must be noted that the studies of Maldonado et al. (2005) and Stuut & Lamy (2004) are located north of 30°S, which is the modern boundary of winter precipitation, and that the study by Moreno (1997) is located south of 40°S, where modern winter precipitation prevails year-round. Hence, this overview especially focuses on the proxies between 30-40°S, but we also note that, according to Zech et al. (2008), the marine cores (Lamy et al. 1999, Stuut & Lamy 2004, Kaiser et al. 2008) are also influenced by marine factors and do not only reflect terrestrial input. Some humid phases are shown in different proxies at the same time, for example during the LGM, but also in pre-LGM times, around 30 ka BP.

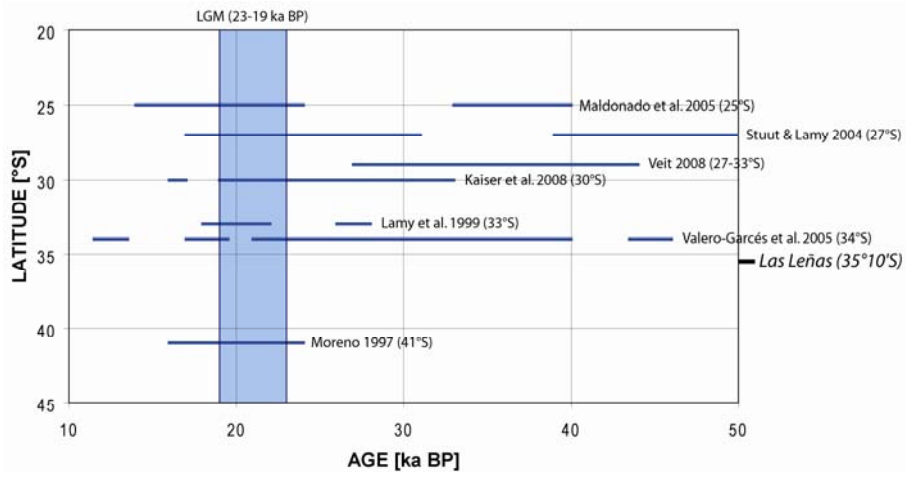

Figure 46: *Generally humid conditions during the late Pleistocene as reported from several studies in Central Chile (blue lines). The global LGM is indicated after Mix et al. (2001). Note that the single studies do not cover the whole time span of the graph. This means that the absence of a blue line does not automatically mean that arid conditions prevailed. Furthermore, no grading of humidity is indicated, meaning that although all blue lines indicate humid conditions, some intervals are reported to be more humid in some studies. More details are given in the text.*

While only generally humid phases are shown in Figure 46, some studies give more detailed information about the humidity increase. Humidity in the record of Stuut & Lamy (2004) culminates at 27 ka BP. The implication of Heusser's (1983) pollen record at Laguna Tagua Tagua (34°S) is an LGM precipitation increase by a factor of 2.5. Furthermore, the highest lake level stands for Tagua Tagua are reported for 40-28 ka (Valero-Garcés et al. 2005). Moreno (1997) reports doubled annual precipitation for 24-16 cal ka BP in the Chilean Lake district (41°S).

6.2.2.3 Comparison with the modeling results

During the last glacial cycle, temperatures were lowest during LGM (MIS2) and MIS4. Regional reconstructed LGM temperature depressions are between 6-8°C (Heusser et al. 1999, Moreno et al. 1999, Heusser 2003); only the values of Rojas et al. (2009) are slightly higher (8-10°C). Hence, we conclude that dP/dT solutions with a temperature depression <10°C are very unrealistic. As only one study showed values >8°C, also a temperature depression >8°C is concluded to be rather unprobable. Regional LGM temperature depression was most probably in the order of ~6-8°C and according to the 2D modeling results, such a cooling would also infer a precipitation increase compared to modern precipitation. Assuming that cooling was strongest during the LGM or MIS4, an LLGM advance in Las Leñas not being synchronous with the LGM (i.e. during MIS3 or the Lateglacial) would have been triggered by a less distinct temperature depression in combination with a stronger precipitation increase.

While the temperature depression for an advance during MIS3 would probably not much lower than for the LGM and, hence, accompanied by an only slightly stronger humidity pulse, dP/dT solutions for a lateglacial advance would be characterized by a much lower temperature depression (~3-4°) in combination with an extreme precipitation increase. While the definition of a maximum plausible temperature depression seems reasonable according to the paleoclimate proxies, it is more difficult to derive a maximum realistic and plausible precipitation increase, mainly (1) because the indications for humidity in other proxies are less precise and (2) also because of the snowdrift issue.

Given that an LGM temperature depression of ~6-8°C is, according to the modeling results, already accompanied by a substantial humidity pulse with, most likely, the Westerlies as main precipitation source, it can be concluded that the LLGM advance in Las Leñas occurred during a phase where humid conditions are reported from Central Chile. There, the strongest reconstructed precipitation increases range from a factor of 2 (Moreno 1997) to a factor of 2.5 (Heusser 2003). It can be concluded that an increase of precipitation by a factor of more than 3 is rather unrealistic for the LLGM in Las Leñas.

6.2.3 Combining evidence

The massive moraines, the modeled AAR values and ELA depressions, but also the comparison with reconstructed paleoclimatic conditions from other proxies indicate that the LLGM advance in Las Leñas was triggered by a cold-humid climate, most probably by a temperature depression of less than 8°C in combination with a more or less substantial increase in precipitation. A temperature depression from ~8-10°C cannot be excluded but is rather unprobable, whereas a temperature depression higher than ~10°C seems to be very unrealistic. It is difficult to define an upper limit of precipitation increase, but an increase by more than a factor of 3 is not indicated by any other proxy. By combining this information, all modeled dP/dT solutions who could have triggered the LLGM advance in Las Leñas are classified in a most probable (white), a rather unprobable (orange) and a very unrealistic (red) range (Figure 47). Most probably, the climatic conditions triggering the LLGM advance in Las Leñas range between dT-8°C/dP+500mm and dT-5°C/dP+1850mm for the scenario with best guess input parameters (Figure 47 left). The most probable range is wider (dT-8°C/dP+300mm to dT-4°C/dP+1850mm) if all other scenarios are taken into account.

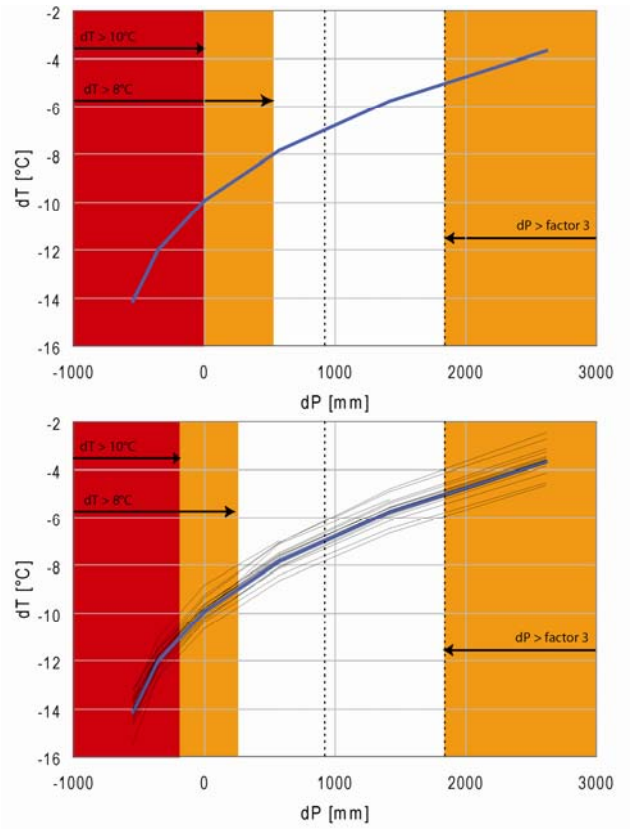

Figure 47: *Very unrealistic (red), rather unprobable (orange) and most probable (white) range within the theoretically possible range of dP/dT solutions resulting from the 2D modeling, for the scenario with best guess input parameters (top) and all scenarios with varied input parameters (bottom).*

6.3 Paleoclimatic implications

Here, the probable timings of the LLGM advance in Las Leñas are discussed (6.3.1). This is done by consulting already established glacier chronologies in the close surroundings of the study area and in regions further north and south, but also by trying to attribute the range of most probable dP/dT solutions to different timings by considering the paleoclimate conditions shown in chapter 6.2. Then, the paleoclimatic implications of the findings are discussed in chapter 6.3.2.

6.3.1 Glacier chronologies

The relative freshness of the moraines and the reconstructed climate conditions for the LLGM in Las Leñas point to an advance during the last glacial cycle. A Holocene advance is very unrealistic not only because of the strong temperature depression indicated by the modeling results. Also the likely humidity pulse would not be in agreement with the general dryer Holocene climate reported from Central Chile. By combining evidence, a rather narrow range of probable dP/dT solutions could be defined. However, this range is still wide enough to impede straight conclusions about the exact timing of the advance, because, as we will see, it supports an advance during LGM, but also during pre-LGM and, less realistic, during lateglacial times.

6.3.1.1 Existing chronologies in the study area

According to Cobos and Boninsegna (1983), the Pleistocene glaciation in the Central Andes of ~34°20S-35°20'S exhibited the character of a continental ice field. The authors called it the Diamante-Atuel glaciation, whose nucleus after the last termination has gradually been transformed into a group of separate glaciers, and some of them still exist today in the western range of the Central Andes (chapter 2.3.2). By now, the only late Pleistocene glacier chronologies in this part of the Central Andes have been established by Espizua (1998, 2004). They all base on relative age-criteria, morphology and ^{14}C dates, but no absolute age control could be obtained. Espizua (2004) identified three late Pleistocene terminal moraines (TM) in the Valle Hermoso (a few km from Las Leñas) and named them, from oldest to youngest, Hermoso I, II and III. However, direct dates could only be obtained for the Hermoso II advance (minimum ages of ~13.6 and ~15.9ka BP). In addition, the Torrecillas moraine (chapter 2.4.2) was minimum-dated to ~10.5 ka BP and tentatively correlated to the Hermoso III advance. Espizua (2004) speculated that the Hermoso I advance could be attributed to early Wisconsinan times (MIS4, ~65 ka BP), the Hermoso II advance to the global LGM, and the Hermoso

III advance to lateglacial times. According to the author, the Hermoso I, II and III advances could probably be correlated with the drifts established in the Rio Mendoza valley.

The LLGM extent of the present study, the hydrologic catchment of the three late Pleistocene advances (Hermoso I, II and III) and the location of Espizua's datings are visualized in Figure 48. The other paleoglacier in the same valley (chapter 5.1.1), a neoglacial advance of Glaciar El Penon (Espizua 2005), and the location of the maximum extent of the controversial neoglacial advance at the Lago Sosneado in the Valle Atuel (Garleff & Stingl 1994) are also shown.

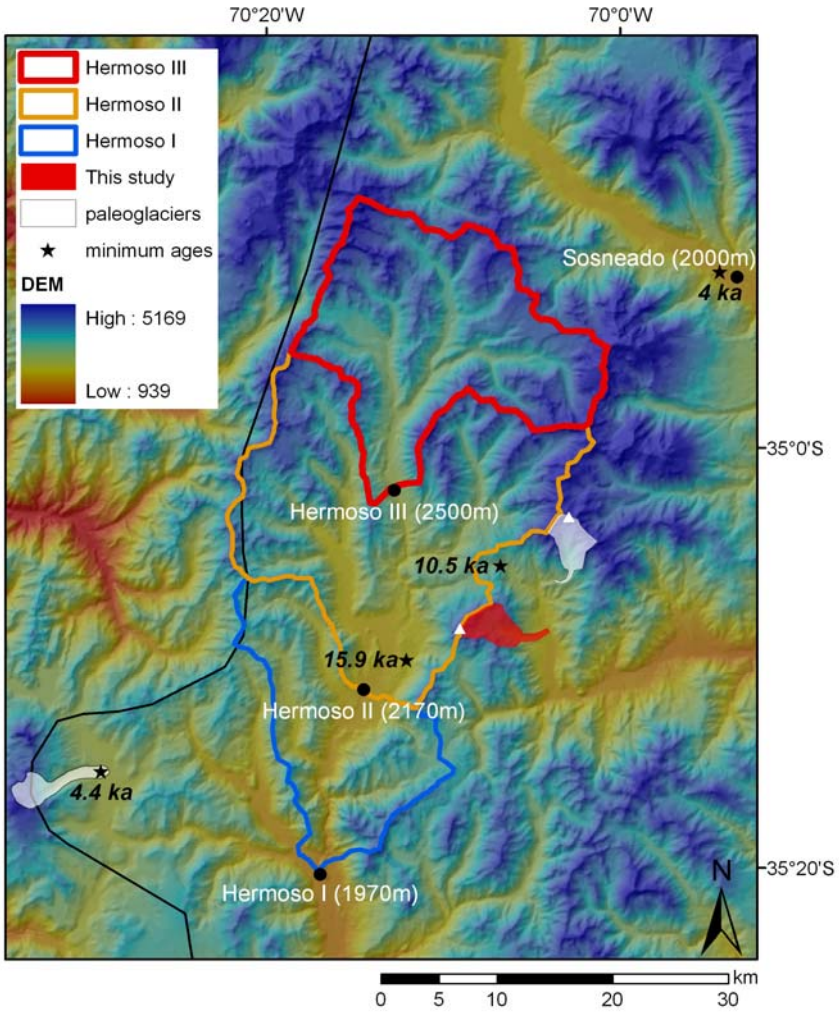

Figure 48: *The present study area, the other paleoglaciers at Co. Las Leñas as mapped with Google Earth imagery, and glacier chronologies available by now. For the Hermoso I, II and III, the hydrologic catchment is plotted, not the effective formerly glaciated area. Also two neoglacial advances are shown, at glaciar El Penon (Espizua 2005), and the location (terminal moraines) of the controversial advance at Lago Sosneado (Garleff & Stingl 1994).*

It must be highlighted (1) that the hydrologic catchment of a bigger advance also compromises the catchments of the smaller ones and (2) that the effective glaciated area during Hermoso I, II and III was certainly smaller than the plotted hydrologic catchments. Nevertheless, it becomes obvious that the glaciation character of the Hermoso advances is very different to the one from Las Leñas paleoglacier. Hermoso I, II and III represent advances pushed by confluences of several outflow glaciers of the Diamante-Atuel ice field. The paleoglacier investigated in this study was not connected with the Diamante-Atuel glaciation and was a typical valley glacier with a single and easy defineable catchment even in late Pleistocene times. This might also be the case for the other paleoglacier mapped a few km NE of Las Leñas. As a consequence, it is not easy to correlate these LLGM advances to one of the Hermoso extents.

It is very unlikely that the LLGM in Las Leñas correlates with the neoglacial advance of glaciar El Peñon, where ELA was depressed by only ≤200m compared to today (Espizua 2005). It is also very unlikely that it corresponds to the neoglacial advance proposed by Garleff & Stingl (1994), for which an ELA depression of 600-800m is proposed. Anyway, when using the best guess climatic input parameters of this study to model an ELA depression in this order, a neoglacial advance of the extent as proposed by Garleff & Stingl (1994) is very unrealistic. An ELA depression of only 600m would need a precipitation increase by a factor of 4.5 (to 4220mm/a) under modern temperatures and still a precipitation increase by a factor of 3.2 (to 2920mm/a) when lowering modern temperatures by 2°C. Such a humidity increase is not corroborated by other proxies. Although climate got more humid in Central Chile after ~5.7 ka BP, modern humid conditions were only reached by ~3.2 ka BP (Valero-Garcés et al. 2005). Provided that the TM of the Hermoso I-III advances are accurately mapped, it is very unlikely that Las Leñas paleoglacier (TM ~2190m asl) reached its LLGM extent synchronously to the Hermoso III advance (TM ~2500m asl). Considering the longitudinal precipitation gradient, it is also rather unlikely that it corresponds to Hermoso II (TM ~2170m asl). From this evidence, it is more probable that the advance investigated in this study occurred together with the Hermoso III advance (TM ~1970m), who probably equates with MIS4 (Espizua 2004). However, the glacial chronology in this region of the Andes bases on poor (absolute) age control. Hence, further evidence and glacier chronologies from a broader region must be consulted to correlate the LLGM advance in Las Leñas to different timings.

6.3.1.2 Probability of different timings

A MIS2 (LGM) advance would indicate temperature depressions in the order of ~6-8°C (Heusser et al. 1999, Moreno et al. 1999, Heusser 2003) and would also infer a humidity pulse. This would be in agreement with the LGM conditions derived in Central Chile by Heusser (2003), the generally humid conditions in Laguna Tagua Tagua between 40-21.5 and 19.5-17 cal ka BP (Valero-Garcés et al. 2005)

and the doubling of annual precipitation in the Chilean Lake District between 24-16 cal ka BP (Moreno 1997). In contrast to drier regions, where precipitation is the crucial parameter for glaciation (Messerli 1973), Kull et al. (2003) showed that Central Andean glaciers in regions with precipitation values above ~800 mm are strongly controlled by temperature. Modern and most probably late Pleistocene precipitation values in Las Leñas are above 800mm, which would support am LGM advance. However, one has to keep in mind that the findings of the arid Central Andes are not transferable without adaptations to different climate conditions in the study area.

Provided that the temperature trend during the last glacial cycle in the Central Andes is (qualitatively) similar to the trend indicated by proxies in Greenland and Antarctica, the modeled dP/dT solutions triggering the LLGM advance in this study would not have differed much for a MIS2, a MIS3 or a MIS4 timing of the advance. A MIS4 (~65ka BP) advance would correlate with the supposed timing of the Hermoso I advance by Espizua (2004), and roughly also with the Laguna Tagua Tagua record indicating humid conditions before 43.5 cal ka BP (Valero-Garcés et al. 2005).

A MIS3 advance during ~40-28 ka BP would be in agreement with deepest lake level stands at Laguna Tagua Tagua and coinciding with the summer insolation minimum on the Southern Hemisphere (Valero-Garcés et al. 2005). It would also be supported by Singer et al. (2000), who suggested an ice retreat between ~25.6-23.3 ka BP at Laguna de Maule (~36°S), by ^{10}Be SED in Valle Rucachoroi (39°S) pointing to an advance at ~35 ka BP (Zech et al. 2008) and by ^{14}C ages indicating that the northern Chilean Lake District reached its LLGM maximum early at ~27 cal ka BP (Denton et al. 1999b, Heusser 2003).

A lateglacial advance would have been triggered by a much less substantial temperature depression in combination with a very extreme humidity increase. In the Chilean Lake District, lateglacial advances are assigned to the so-called Huelmo/Mascardi cold reversal around ~14-12 ka BP, which is evident in many proxies (Ariztegui et al. 1997, Moreno 1997, Moreno et al. 1999, Moreno et al. 2001, Hajdas et al. 2003, Heusser 2003, Heusser et al. 2006, De Batist et al. 2008). This reversal is interpreted as the local counterpart of the northern-hemisphere Younger Dryas, preceding the latter by ~500-1000a (De Batist et al. 2008). A lateglacial advance would be in agreement with the (minimum) basal peat date of ~10.5ka BP behind the Torrecillas moraine in Las Leñas (Espizua 2004). According to Moreno et al. (1999), the temperature depression during the Lateglacial Cold Reversals was below ~5°C compared to modern conditions (-6-7°C depression during the LGM, warming of >5°C during the last termination, followed by a cooling during the cold reversals of ≤2-3°C), and rather around ~3-4°C. According to the 2D modeling results, a temperature depression by ~3-4°C would have involved an extreme increase of modern precipitation by a factor of ~3.5 (for the best guess scenario) and by a

factor >3 (considering all scenarios with varied input parameters). Such a strong increase is not indicated by any proxy.

Therefore, it can be concluded that an LLGM advance in Las Leñas in the Lateglacial is rather unprobable. An advance during MIS4 as proposed by Espizua (2004) for the Hermoso I advance cannot be excluded, but the relative freshness of the moraines suggest a younger age. An advance during MIS2 or MIS3 is most probable. Thereby, a possible MIS3 advance would most probably not have occurred during any interstadial triggered by the DOE and reflected in the Antarctic as warm event, but under normal stadial conditions. The LLGM advance in Las Leñas point to the need of a humidity pulse, and humid conditions are reported for the MIS2 as well as for MIS3. It can be concluded that, as expected in the hypothesis of the present study, the LLGM advance in Las Leñas was most probably triggered by low temperatures in combination with a humidity pulse from Westerlies. These climate conditions are generally attributed to full glacial conditions in Central Chile. When consulting other established glacier chronologies and humidity reconstructions between ~30-40°S, however, there are more arguments for an advance prior to the LGM, around ~40-28 ka BP (MIS3). As a consequence, we cannot approve nor reject that the advance Las Leñas occurred around ~35 ka BP, which was part of the hypothesis underlying the present study. It is also important to note that the present study reconstructs paleoclimate conditions that occurred during only a short period, i.e. the duration of the glacier's response time to mass balance changes (<100a). The reconstructed paleoclimate conditions must therefore be seen as extremes, not as mean conditions that prevailed over several millenia. During the last glacial, the glacier most likely also existed before and after reaching the maximum extent. Suggate & Almond (2005) highlight that in the midlatitudes of 40-44°S of New Zealand, Tasmania and Chile, glaciers experienced advances at ~34-18 ka BP, that did not vary greatly in extent within each region.

6.3.2 Atmospheric circulation

Considering the most probable range of dP/dT solutions, a substantial temperature depression and a more or less significant humidity pulse was needed to trigger the LLGM advance in Las Leñas. This humidity pulse is most probably attributed to increased winter precipitation from Westerlies. The redeposition of snow from the predominant Westerlies determines that the eastern watershed of the Andes around Las Leñas is much more glaciated than the western one, and the east-exposed catchment of Las Leñas paleoglacier *per se* indicates that the Westerlies were the main precipitation source during the LLGM advance. This is also supported by the fact that the nearby paleoglacier at Co. Las Leñas, which is located 10km NE of the present study site and whose southward exposed catchment is

less favorable for accumulation by snowdrift, most probably not advanced as far down as Las Leñas paleoglacier.

The debate if the westerly belt was shifted equatorward or poleward during the late Pleistocene is still controversial (chapter 2.4.3.2). However, an intensified westerly circulation in late Pleistocene times is indicated by many proxies in Central Chile (e.g. Heusser 2003, Stuut & Lamy 2004, Valero-Garcés et al. 2005), but some of them are rather attributed to LGM than pre-LGM times. Modeling studies indicate rather a poleward displacement of the Southern Westerlies, but show significant regional differences (Valdes 2000, Wyrwoll et al. 2000) and only small changes (Valdes 2000). The most recent modeling study with four coupled ocean-atmosphere simulations (Rojas et al. 2009) found no significant changes in the latitudinal position of the jet stream, but indicates increased storm activity in winter in midlatitudes (25-45°S).

Increased winter precipitation is also supported by the present study indicating a very probable humidity pulse needed to trigger the LLGM advance in Las Leñas. Located just south of 34°S, where winter precipitation is dominant and regular, whereas north of 34°S, winter precipitation only occurs episodically (Valero-Garcés et al. 2005), Las Leñas is a suitable to discuss eventual latitudinal shifts of the westerly belt. An argument against a poleward shift of the westerly belt is that reduced evaporation due to lower temperatures could not account for the dramatic increase in moisture as found in different sedimentological records at Laguna Tagua Tagua (Valero-Garcés et al. 2005). This is particularly true for the humidity pulse indicated by this modeling study. The importance of snowdrift for the modern glaciations around the study area clearly shows that a large fraction of the effective (solid) precipitation is transported from strong Westerlies. A poleward shift and a decrease in the intensity of the Westerlies would have completely altered the precipitation regime in Las Leñas, which is not corroborated by the results of this study.

With respect to interannual variability of precipitation in the region of the study area and its impact on glacier mass balance (chapter 2.2.2.3), also the ENSO-phenomenon during late Pleistocene times claims attention. Knowledge about the paleo ENSO record is poor, but has increased in the past decades (Cane 2005). Tudhope et al. (2001) suggest that the ENSO is dampened during glacial conditions and forced by precessional orbital variations. In summary, they propose that ENSO has been a persistent component of the climate system during the past 130 ka, that ENSO might be stronger today than at any other time in the past 150 ka, that ENSO was weak during the early and mid-Holocene, and that ENSO was clearly operating also during much colder glacial times, e.g. around 38-42 ka BP. Hence, it is likely that ENSO also influenced interannual variability of winter precipitation (and therefore mass balance) during the LLGM. However, by now, no quantitative conclusions about the ENSO impact on late Pleistocene humidity in Central Chile can be derived.

7 Conclusions and Outlook

Paleoclimatic conditions during the LLGM advance in Las Leñas (35°S) were investigated by applying the glacier-climate model from Kull (1999). The model was originally built to investigate glacio-climatological conditions in regions with prevailing summer precipitation. Regarding the methodology used, the present study has established the southernmost study site so far and the first lying in midlatitudes with dominant and regular winter precipitation from the Westerlies. Lying between the arid to semiarid conditions in the Andes of Cuyo and the humid conditions of Patagonia, the location of the present study is particularly interesting.

Only slight adjustments turned out to be necessary to fit the model to a regime with regular winter precipitation. According to the actualistic principle, the model was found to be suitable to investigate paleo glacio-climatological as it reasonably reproduced modern glacio-climatological conditions in the study area.

No 3D modeling could successfully be carried out in the present study, but the 2D modeling provides robust results even when important input parameters are strongly varied. The possible climate conditions producing a glacier in equilibrium state range from extremely cold and dry to temperate and extremely humid. However, by evaluating the glacier geometry and by consulting reconstructed late Pleistocene climatic conditions in the broader region of the study area, a rather narrow range of most probable precipitation/temperature solutions could be defined. This range implies that the LLGM in Las Leñas was triggered in a cold-humid climate. The associated best guess climatic conditions range from a temperature depression of 8°C (in combination with a precipitation increase of 500mm) to a temperature depression of 5°C (in combination with a precipitation increase of 1840mm). The precipitation increase can most probably be attributed to increased winter precipitation from Westerlies. The redeposition of snow from the predominant Westerlies determines that the eastern watershed of the Andes around Las Leñas is much more glaciated than the western one, and the east-exposed catchment of Las Leñas paleoglacier *per se* indicates that the Westerlies were the main precipitation source during the LLGM advance. This is also corroborated by many proxies from Central Chile, who suggest increased winter precipitation during late Pleistocene times. As a

consequence, we support the first part of our hypothesis that the LLGM in Las Leñas was triggered by a strong temperature decrease in combination with a humidity pulse from intensified Westerlies.

The reconstructed cold-humid paleoclimate in this study points to an LLGM advance in Las Leñas during full glacial times. A lateglacial advance is very unprobable. However, ultimate constraints about the exact timing during the last glacial cycle are not possible. Still, a MIS4 advance is less probable due to the relative freshness of the moraines. Several periods during LGM (MIS2) and MIS3 would fulfill a strong temperature depression and humid conditions in Central Chile. When consulting other established glacier chronologies and humidity reconstructions between ~30-40°S, however, there are more arguments for an advance prior to the LGM, around ~40-28 ka BP (MIS3). Nevertheless, it is not possible to approve nor reject the second part of our hypothesis that the LLGM in Las Leñas occurred during pre LGM times at ~35 ka BP. During the field campaign in December 2008, our group sampled several boulders from the same moraines as used for the mapping in this study. The corresponding ^{10}Be surface exposure dates will shortly be available and are expected to bring the timing issue forward.

8 Bibliography

Ammann C. (1996): Climate change in den trockenen Anden: Aktuelle Niederschlagsmuster. Geographica Bernensia G 46: 81–127.

Ammann C., Jenny B., Kammer K., Messerli B. (2001): Late Quaternary Glacier response to humidity changes in the arid Andes of Chile (18-29°S). Palaeogeography, Palaeoclimatology, Palaeoecology 172: 313-326.

Ariztegui D., Bianchi M., Masaferro J., Lafargue E., Niessen F. (1997): Interhemispheric synchrony of Late-glacial climatic instability as recorded in proglacial Lake Mascardi, Argentina. Journal of Quaternary Science 12(4): 333-338.

Arnold N., van Andel T., Valen V. (2002): Extent and dynamics of the Scandinavian Ice Sheet during oxygen isotope stage 3 (65,000–25,000 yr BP). Quaternary Research 57: 38-48.

Baker P., Seltzer G., Fritz S., Dunbar R., Grove M., Tapia P., Cross S., Rowe H., Broda J. (2001): The History of South American Tropical Precipitation for the Past 25,000 Years. Science 291: 640-643.

Benn D., Evans D. (1998): Glaciers and Glaciation. Oxford University Press Inc., New York.

Bentley M. (1997): Relative and radiocarbon chronology of two former glaciers in the Chilean Lake District. Journal of Quaternary Science 12(1): 25-33.

Berger A., Loutre M. (1991): Insolation values for the climate of the last 10 million years. Quaternary Science Reviews 10(4): 297-317.

Blatter H., Funk M., Ohmura A. (1984): Atlas of Solar Climate for the period from 200'000 B.P to 20'000 A.P. Zürcher Geographische Schriften 10. Geographisches Institut, Eidgenössische Technische Hochschule Zürich.

Blunier T., Chappellaz J., Schwander J., Dällenbach A., Stauffer B., Stocker T., Raynaud D., Jouzel J., Clausen H., Hammer C. (1998): Asynchrony of Antarctic and Greenland climate change during the last glacial period. Nature 394: 739-743.

Brenneis J. (2002): Bergtouren Jürgen Brenneis. Available online at http://freenet-homepage.de/thehighrisepages/jotbe/, Access 1.4.2009.

Brenning A. (2005): Climatic and geomorphological controls of rock glaciers in the Andes of Central Chile. Combining statistical modelling and field Mapping. Dissertation. Mathematisch-Naturwissenschaftliche Fakultät II, Humboldt Universität zu Berlin.

Budd W. (1969): The dynamics of ice masses. Australian National Antarctic Research Expeditions Scientific Report 108.

Budyko M. (1974): Climate and Life. Academic Press. New York.

Buttstädt M., Möller M., Iturraspe R., Schneider C. (2009): Mass balance evolution of Martial Este Glacier, Tierra del Fuego (Argentina) for the period 1960-2099. Advances in Geosciences, accepted.

Calpal (2007): The Calpal Online. Cologne Radiocarbon Calibration & Paleoclimate Research. Available online at http://www.calpal-online.de, Access: 17.9.2009.

Cane M. (2005): The evolution of El Niño, past and future. Earth and Planetary Science Letters 230: 227-240.

Clapperton C., Clayton J., Benn D., Marden C., Argollo J. (1997): Late Quaternary glacier advances and palaeolake highstands in the Bolivian Altiplano. Quaternary International 38/39: 49-59.

Clayton J., Clapperton C. (1997): Broad synchrony of a Late-glacial glacier advance and the highstand of palaeolake Tauca in the Bolivian Altiplano. Journal of Quaternary Science 12(3): 169-182.

Cobos D., Boninsegna J. (1983): Fluctuations of some glaciers in the upper Atuel River basin, Mendoza, Argentina. Quaternary of South America and Antarctic Peninsula 1: 61-82.

Cruz F., Burns S., Karmann I., Sharp W., Vuille M., Cardoso A., Ferrari J., Dias P., Viana O. (2005): Insolation-driven changes in atmospheric circulation over the past 116,000 years in subtropical Brazil. Nature 434: 63-66.

De Batist M., Fagel N., Loutre M., Chapron E. (2008): A 17,900-year multi-proxy lacustrine record of Lago Puyehue (Chilean Lake District): introduction. Journal of Paleolimnology 39: 151-161.

Denton G., Lowell T., Heusser C., Moreno P., Andersen B., Heusser L., Schlüchter C., Marchant D. (1999a): Interhemispheric linkage of paleoclimate during the last glaciation. Geografiska Annaler. Series A. Physical Geography: 107-153.

Denton G., Lowell T., Heusser C., Schluechter C., Andersen B., Heusser L., Moreno P., Marchant D. (1999b): Geomorphology, stratigraphy, and radiocarbon chronology of Llanquihue drift in the area of the southern Lake District, Seno Reloncavi, and Isla Grande de Chiloe, Chile. Geogr. Ann. 81 A(2): 167–229.

Douglass D., Singer B., Kaplan M., Mickelson D., Caffee M. (2006): Cosmogenic nuclide surface exposure dating of boulders on last-glacial and late-glacial moraines, Lago Buenos Aires, Argentina: Interpretive strategies and paleoclimate implications. Quaternary Geochronology 1: 43-58.

EPICA community members (2004): Eight glacial cycles from an Antarctic ice core. Nature 429(6992): 623-628.

EPICA community members (2006): One-to-one coupling of glacial lcimate variability in Greenland and Antarctica. Nature 444: 195-198.

Espizua L. (1993): Quaternary glaciations in the Rio Mendoza Valley, Argentine Andes. Quaternary Research 40: 150-162.

Espizua L. (1999): Chronology of Late Pleistocene glacier advances in the Rio Mendoza Valley, Argentina. Global and Planetary Change 22: 193-200.

Espizua L. (2004): Pleistocene glaciations in the Mendoza Andes, Argentina. In: Quaternary Glaciations: Extent and Chronology. Part III: South America, Asia, Africa, Australasia, Antarctica, Ehlers, J., Gibbard, P. (eds.). Elsevier: Cambridge, MA; 69-73.

Espizua L. (2005): Holocene glacier chronology of Valenzuela Valley, Mendoza Andes, Argentina. The Holocene 15(7): 1079-1085.

Espizua L., Pitte P. (2009): The Little Ice Age glacier advance in the Central Andes (35°S), Argentina. Palaeogeography, Palaeoclimatology, Palaeoecology, in press.

Farber D., Hancock G., Finkel R., Rodbell D. (2005): The age and extent of tropical glaciation in the Cordillera Blanca, Peru. Journal of Quaternary Science 20: 759-776.

Garleff K., Stingl H. (1984): Neue Befunde zur Jungquartären Vergletscherung in Cuyo und Patagonien. Berliner Geogr. Abh. 36: 105-112.

Garleff K., Stingl H. (1994): Reply to Gosse & Evenson: reinterpretation of the evidence for a significant neoglacial advance in the Rio Atuel valley, Mendoza province, Argentina. Zeitschrift für Geomorphologie 38: 339-342.

Garreaud R., Aceituno P. (2007): Atmospheric circulation and climatic variability. In: The physical geography of South America, Veblen, T., Young, K., Orme, A. (eds.). Oxford University Press, Inc., New York.

Garreaud R., Vuille M., Clement A. (2003): The climate of the Altiplano: observed current conditions and mechanisms of past changes. Palaeogeography, Palaeoclimatology, Palaeoecology 194: 5-22.

Garreaud R.D., Vuille M., Compagnucci R., Marengo J. (2008): Present-day South American climate. Palaeogeography, Palaeoclimatology, Palaeoecology, in press.

Geyh M., Grosjean M., Núñez L., Schotterer U. (1999): Radiocarbon reservoir effect and the timing of the Late-Glacial / Early Holocene Humid Phase in the Atacama Desert (northern Chile). Quaternary Research 52: 143-153.

Gosse J., Evenson E. (1994): Reinterpretation of the evidence for a significant mid-holocene ice advance in the Rio Atuel valley, Mendoza Province, Argentina. Zeitschrift fur Geomorphologie 38: 327-338.

Grosjean M., Santoro C., Thompson L., Núnez L., Standen V. (2007): Mid-Holocene climate and culture change in the South Central Andes. In: Climate change and cultural dynamics: A global perspective on mid Holocene transitions, Anderson D., Maasch, K., Sandweiss, D (eds.). Elsevier Inc.

Grosjean M., van Leeuwen J., Van Der Knaap W., Geyh M., Ammann B., Tanner W., Messerli B., Nunez L., Valero-Garces B., Veit H. (2001): A 22,000 14C year BP sediment and pollen record of climate change from Laguna Miscanti (23 S), northern Chile. Global and Planetary Change 28(1-4): 35-51.

Häberli W. (2004): Gletscher im Umweltkontext (Teil 1: Paläoglaziologie). Vorlesungsskript der Geographischen Instituts der Universität Zürich.

Häberli W., Hoelzle M., Fischer U., Vonder Mühll D. (2005): Gletscher und Permafrost. Vorlesungsskript des Geographischen Instituts der Universität Zürich.

Hajdas I., Bonani G., Moreno P., Ariztegui D. (2003): Precise radiocarbon dating of Late-Glacial cooling in mid-latitude South America. Quaternary Research 59: 70-78.

Harrison S. (2004): The Pleistocene glaciations of Chile. In: Quaternary Glaciations: Extent and Chronology. Part III: South America, Asia, Africa, Australasia, Antarctica, Ehlers, J., Gibbard, P. (eds.). Elsevier: Cambridge, MA; 89-103.

Hastenrath S. (1978): Heat-budget measurements on the Quelccaya ice cap, Peruvian Andes. Journal of Glaciology 20(82): 85–97.

Hastenrath S. (1984): The glaciers of equatorial East Africa. D. Reidel Publishing Company. Dordrecht / Boston / Lancaster.

Heusser C. (1983): Quaternary pollen record from Laguna de Tagua Tagua, Chile. Science 219: 1429-1432.

Heusser C. (1990): Ice age vegetation and climate of subtropical Chile. Palaeogeography, Palaeoclimatology, Palaeoecology 80(2): 107-127.

Heusser C. (2003): Ice Age Southern Andes: A Chronicle of Paleoecological Events. Elsevier. Amsterdam.

Heusser C., Heusser L., Lowell T. (1999): Paleoecology of the southern Chilean Lake District-Isla Grande de Chiloé during middle-Late Llanquihue glaciation and deglaciation. Geografiska Annaler. Series A. Physical Geography 81(2): 231-284.

Heusser C., Lowell T., Heusser L., M. A., M. S. (2000): Pollen sequence from the Chilean Lake District during the Llanquihue glaciation in marine Oxygen Isotope Stages 4-2. Journal of Quaternary Science 15(2): 115-125.

Heusser L., Heusser C., Pisias N. (2006): Vegetation and climate dynamics of southern Chile during the past 50,000 years: results of ODP Site 1233 pollen analysis. Quaternary Science Reviews 25: 474-485.

Hock R. (2003): Temperature index melt modelling in mountain areas. Journal of Hydrology 282: 104-115.

Huss M. (2009): Past and Future Changes of Glacier Mass Balance. Mitteilungen 213 der Versuchsanstalt für Wasserbau, Hydrologie und Glaziologie (VAW).

Imhof S. (2006): Gletscher-Klima-Modellierung in der Cordillera Cochabamba, Bolivien. Diplomarbeit. Geographisches Institut der Universität Bern.

Indermühle A., Monnin E., Stauffer B., Stocker T., Wahlen M. (2000): Atmospheric CO 2 concentration from 60 to 20 kyr BP from the Taylor Dome ice core, Antarctica. Geophys. Res. Lett 27(5): 735–738.

Iqbal M. (1983): An introduction to solar radiation. Academic Press. Ontario.

Jenny B., Kammer K. (1996): Climate change in den trockenen Anden: Jungquartäre Vergletscherungen. Geographica Bernensia G 46: 1–80.

Kaiser J., Schefuß E., Lamy F., Mohtadi M., Hebbeln D. (2008): Glacial to Holocene changes in sea surface temperature and coastal vegetation in north central Chile: high versus low latitude forcing. Quaternary Science Reviews 27: 2064-2075.

Kaser G., Georges C. (1999): On the mass balance of low latitude glaciers with particular consideration of the Peruvian Cordillera Blanca. Geogr. Ann. 81 A(4): 643-651.

Kaser G., Osmaston H. (2002): Tropical glaciers. In: International Hydrological Series. University Press. Cambridge.

Klein A., Seltzer G., Isacks B. (1999): Modern and last local glacial maximum snowlines in the Central Andes of Peru, Bolivia, and Northern Chile. Quaternary Science Reviews 18(1): 63-84.

Kottek M., Grieser J., Beck C., Rudolf B., Rubel F. (2006): World map of the Koppen-Geiger climate classification updated. Data available online at http://koeppen-geiger.vu-wien.ac.at/, Access: 23.7.2009. Meteorologische Zeitschrift 15(3): 259-263.

Kull C. (1999): Modellierung paläoklimatischer Verhältnisse basierend auf der jungpleistozänen Vergletscherung in Nordchile - Ein Fallbeispiel aus den Nordchilenischen Anden. Zeitschrift für Gletscherkunde und Glazialgeologie 35(1): 35–64.

Kull C., Grosjean M. (2000): Late Pleistocene climate conditions in the north Chilean Andes drawn from a climate-glacier model. Journal of Glaciology 46(155): 622-632.

Kull C., Grosjean M., Veit H. (2002): Modeling Modern and Late Pleistocene Glacio-Climatological Conditions in the North Chilean Andes (29–30°). Climatic Change 52: 359-381.

Kull C., Hänni F., Grosjean M., Veit H. (2003): Evidence of an LGM cooling in NW-Argentina (22°S) derived from a glacier climate model. Quaternary International 108: 3-11.

Kull C., Imhof S., Grosjean M., Zech R., Veit H. (2008): Late Pleistocene glaciation in the Central Andes: Temperature versus humidity control - A case study from the eastern Bolivian Andes (17°S) and regional synthesis. Global and Planetary Change 60: 148-164.

Lamy F., Hebbeln D., Wefer G. (1999): High-resolution marine record of climatic change in mid-latitude Chile during the last 28,000 years based on terrigenous sediment parameters. Quaternary Research 51(1): 83-93.

Lemke P., Ren J., Alley R., Allison I., Carrasco J., Flato G., Fujii Y., Kaser G., Mote P., Thomas R., Zhang T. (2007): Observations: changes in snow, ice and frozen ground. In: Climate Change 2007: The Physical Science basis. Contribution of Working Group I to the Fourth Assessment Report of the Intergovernmental Panel on Climate Change. Solomon, S., D. Qin, M. Manning, Z. Chen, M. Marquis, K.B. Averyt, M. Tignor and H.L. Miller (eds.). Cambridge University Press, Cambridge, United Kingdom and New York, NY, USA., 337-383.

Lowell T., Heusser C., Andersen B., Moreno P., Hausser A., Heusser L., Schlüchter C., Marchant D., Denton G. (1995): Interhemispheric correlation of Late Pleistocene climate events. Science 269: 1541–1549.

Lynch-Stieglitz J. (2004): Hemispheric Asynchrony of Abrupt Climate Change. Science 304: 1919-1920.

Maldonado A., Betancourt J., Latorre C., Villagrán C. (2005): Pollen analyses from a 50'000-yr rodent midden series in the southern Atacama Desert (25°30'S). Journal of Quaternary Science 20: 493-507.

Marengo J., Soares W., Saulo C., Nicolini M. (2004): Climatology of the low-level jet east of the Andes as derived from the NCEP - NCAR reanalyses: Characteristics and temporal variability. Journal of Climate 17: 2261-2280.

Markgraf V. (1989): Reply to CJ Heusser's Southern westerlies during the last glacial maximum. Quaternary Research 31: 426–432.

Markgraf V., Dodson J., Kershaw A., McGlone M., Nicholls N. (1992): Evolution of late Pleistocene and Holocene climates in the circum-South Pacific land areas. Climate Dynamics 6: 193-211.

Masiokas M., Villalba R., Luckman B., Le Quesne C., Aravena J. (2006): Snowpack variations in the central Andes of Argentina and Chile, 1951–2005: Large-scale atmospheric influences and implications for water resources in the region. Journal of Climate 19: 6334-6352.

May J., Zech R., Veit H. (2008): Late Quaternary paleosol-sediment-sequences and landscape evolution along the Andean piedmont, Bolivian Chaco. Geomorphology 98(1-2): 34-54.

McCulloch R., Bentley M., Purves R., Hulton N., Sugden D., Clapperton C. (2000): Climatic inferences from glacial and palaeoecological evidence at the last glacial termination, southern South America. Journal of Quaternary Science 15(4): 409-417.

McCulloch R., Fogwill C., Sugden D., Bentley M., Kubik P. (2005): Chronology of the last glaciation in central Strait of Magellan and Bahía Inútil, southernmost South America. Geogr. Ann. 87 A(2): 289-312.

Messerli B. (1973): Problems of vertical and horizontal arrangement in the high mountains of the extreme arid zone (Central Sahara). Arctic and Alpine Research 5: 139-147.

Messerli B., Grosjean M., Bonani G., Bürgi A., Geyh M., Graf K., Ramseyer K., Romero H., Schotterer U., Schreier H. (1993): Climate change and natural resource dynamics of the Atacama Altiplano during the last 18,000 years: A preliminary synthesis. Mountain Research and Development 13: 117-127.

Mix A., Bard E., Schneider R. (2001): Environmental processes of the ice age: land, oceans, glaciers (EPILOG). Quaternary Science Reviews 20(4): 627-657.

Mölg T. (2002): Modellierung der kurzwelligen Einstrahlung mit GIS am Beispiel eines tropischen Hochgebirges. Beiträge zum AGIT-Symposium Salzburg 2002. 347-356

Mölg T., Georges C., Kaser G. (2003): The contribution of increased incoming shortwave radiation to the retreat of the Rwenzori Glaciers, East Africa, during the 20th century. International Journal of Climatology 23: 291-303.

Moreno P. (1997): Vegetation and climate near Lago Llanquihue in the Chilean Lake District between 20'200 and 9'500 14C yr BP. Journal of Quaternary Science 12(6): 485-500.

Moreno P., Jacobson G., Lowell T., Denton G. (2001): Interhemispheric climate links revealed by a late-glacial cooling episode in southern Chile. Nature 409: 804-808.

Moreno P., Lowell T., Jacobson Jr G., Denton G. (1999): Abrupt vegetation and climate changes during the last glacial maximum and last termination in the Chilean Lake District: A case study from Canal de la Puntilla (41°S). Geogr. Ann. 81 A(2): 285-311.

NASA Visible Earth - A catalog of NASA images and animations of our home planet. Available online at http://visibleearth.nasa.gov/view_rec.php?id=36, Access 1.9.2009.

Nesje A. (1992): Topographical effects on the equilibrium-line altitude on glaciers. GeoJournal 27(4): 383-391.

New M., Lister D., Hulme M., Makin I. (2002): A high-resolution data set of surface climate over global land areas. Climate Research 21: 1-25.

North Greenland Ice Core Project members (2004): High-resolution record of Northern Hemisphere climate extending into the last interglacial period. Nature 431: 147-151.

Oerlemans J. (1997): A flowline model for Nigardsbreen, Norway: projection of future glacier length based on dynamic calibration with the historic record. Annals of Glaciology 24: 382-389.

Ohmura A., Kasser P., Funk M. (1992): Climate at the equilibrium line of glaciers. Journal of Glaciology 38(130): 397-411.

Orme A. (2007a): The Tectonic Framework of South America. In: The physical geography of South America, Veblen, T., Young, K., Orme, A. (eds.). Oxford University Press, Inc., New York.

Orme A. (2007b): Tectonism, Climate, and Landscape Change. In: The physical geography of South America, Veblen, T., Young, K., Orme, A. (eds.). Oxford University Press, Inc., New York.

Paterson W. (1994): The physics of glaciers. Pergamon, Oxford.

Petit J., Jouzel J., Raynaud D., Barkov N., Barnola J., Basile I., Bender M., Chappellaz J., Davis M., Delaygue G. (1999): Climate and atmospheric history of the past 420'000 years from the Vostok ice core, Antarctica. Nature 399: 429-436.

Pidwirny M. (2006): Net Radiation and the Planetary Energy Balance. Fundamentals of Physical Geography, 2nd Edition. Date. Available online at http://www.physicalgeography.net/fundamentals/7i.html. Access: 14.9.2009.

Placzek C., Quade J., Patchett P. (2006): Geochronology and stratigraphy of late Pleistocene lake cycles on the southern Bolivian Altiplano: Implications for causes of tropical climate change. Bulletin of the Geological Society of America 118: 515-532.

Press F., Siever R. (1995): Allgemeine Geologie, eine Einführung. Spektrum Akademischer Verlag, Heidelberg/Berlin/Oxford

Rodbell D., Smith J., Mark B. (2009): Glaciation in the Andes during the Lateglacial and Holocene. Quaternary Science Reviews 28: 2165-2212.

Rojas M., Moreno P., Kageyama M., Crucifix M., Hewitt C., Abe-Ouchi A., Ohgaito R., Brady E., Hope P. (2009): The Southern Westerlies during the last glacial maximum in PMIP2 simulations. Climate Dynamics 32: 525-548.

Rundel P., Villagra P., Dillon M., Roig-Junent S., Debandi G. (2007): Arid and semi-arid ecosystems. In: The physical geography of South America, Veblen, T., Young, K., Orme, A. (eds.). Oxford University Press, Inc., New York.

Sailer R., Kerschner H., Heller A. (1999): Three-dimensional reconstruction of Younger Dryas glaciers with a raster-based GIS. Glacial Geology and Geomorphology. Available online at http://boris.qub.ac.uk/papers/full/1999/rp011999/rp01.html, Access 20.9.2009.

Saillard M., Hall S., Audin L., Farber D., Hérail G., Martinod J., Regard V., Finkel R., Bondoux F. (2009): Non-steady long-term uplift rates and Pleistocene marine terrace development along the Andean margin of Chile (31°S) inferred from 10Be dating. Earth and Planetary Science Letters 277: 50-63.

Saulo A., Nicolini M., Chou S. (2000): Model characterization of the South American low-level flow during the 1997–1998 spring–summer season. Climate Dynamics 16: 867-881.

Schaefer J., Denton G., Barrell D., Ivy-Ochs S., Kubik P., Andersen B., Phillips F., Lowell T., Schlüchter C. (2006): Near-synchronous interhemispheric termination of the Last Glacial Maximum in mid-latitudes. Science 312: 1510-1513.

Schmidhauser A. (2007): Modelling glacier-climate interaction in the Central Andean Sierra del Quilmes, NW-Argentina. Diplomarbeit. Geographisches Institut der Universität Bern.

Schneider C., Kilian R., Glaser M. (2007): Energy balance in the ablation zone during the summer season at the Gran Campo Nevado Ice Cap in the Southern Andes. Global and Planetary Change 59: 175-188.

Sevruk B. (1985): Schneeanteil am Monatsniederschlag. Beiträge zur Geologie der Schweiz-Hydrologie 31: 127–137.

Sevruk B. (2004): Niederschlag Als Wasserkreislaufelement–Theorie und Praxis der Niederschlagsmessung. Eidgenössische Technische Hochschule, Zürich

Singer B., Hildreth W., Vincze Y. (2000): 40Ar/39Ar evidence for early deglaciation of the central Chilean Andes. Geophysical Research Letters 27: 1663-1666.

Smith J., Seltzer G., Farber D., Rodbell D., Finkel R. (2005): Early local last glacial maximum in the tropical Andes. Science 308: 678-681.

Stuut J., Lamy F. (2004): Climate variability at the southern boundaries of the Namib (southwestern Africa) and Atacama (northern Chile) coastal deserts during the last 120'000 yr. Quaternary Research 62: 301-309.

Stuut J., Marchant M., Kaiser J., Lamy F., Mohtadi M., Romero O., Hebbeln D. (2006): The late Quaternary paleoenvironment of Chile as seen from marine archives. Geographica Helvetica 61: 135-151.

Sugden D., Bentley M., Fogwill C., Hulton N., McCulloch R., Purves R. (2005): Late-glacial glacier events in southernmost South America: a blend of 'northern' and 'southern' hemispheric climatic signals? Geogr. Ann. 87 A(2): 273-288.

Sugden D., John B. (1976): Glaciers and landscape. Edward Arnold, London.

Suggate R., Almond P. (2005): The last glacial maximum (LGM) in western South Island, New Zealand: implications for the global LGM and MIS 2. Quaternary Science Reviews 24: 1923-1940.

Tudhope A., Chilcott C., McCulloch M., Cook E., Chappell J., Ellam R., Lea D., Lough J., Shimmield G. (2001): Variability in the El Niño-Southern Oscillation through a glacial-interglacial cycle. Science 291: 1511-1517.

Valdes P. (2000): South American palaeoclimate model simulations: how reliable are the models? Journal of Quaternary Science 15: 357-368.

Valero-Garcés B., Jenny B., Rondanelli M., Delgado-Huertas A., Burns S., Veit H., Moreno A. (2005): Palaeohydrology of Laguna de Tagua Tagua (34°30' S) and moisture fluctuations in Central Chile for the last 46'000 yr. Journal of Quaternary Science 20(7-8): 625–641.

Vandergoes M., Newnham R., Preusser F., Hendy C., Lowell T., Fitzsimons S., Hogg A., Kasper H., Schlüchter C. (2005): Regional insolation forcing of late Quaternary climate change in the Southern Hemisphere. Nature 436: 242-245.

Veit H. (2008): The Southern Westerlies in Central Chile (Norte Chico) during the Upper Quaternary as documented in Paleosols. Poster session of the 4th Alexander von Humboldt International Conference. Santiago / Chile, 24-28 November 2008.

Viale M., Norte F. (2009): Strong Cross-Barrier Flow under Stable Conditions producing Intense Winter Orographic Precipitation: A Case Study over the Subtropical Central Andes. Weather and Forecasting 24(4): 1009-1031.

Vuille M. (1996): Zur raumzeitlichen Dynamik von Schneefall und Ausaperung im Bereich des südlichen Altiplano, Südamerika. Geographica Bernensia G 45: 1-118.

Vuille M., Ammann C. (1997): Regional snowfall patterns in the high, arid Andes. Climatic Change 36(3): 413-423.

Watanabe O., Jouzel J., Johnsen S., Parrenin F., Shoji H., Yoshida N. (2003): Homogeneous climate variability across East Antarctica over the past three glacial cycles. Nature 422: 509-512.

WGMS(ICSI-IAHS) (various years-a): Fluctuations of Glaciers. World Glacier Monitoring Service, Zurich.

WGMS(ICSI-IAHS) (various years-b): Mass balance bulletin. World Glacier Monitoring Service, Zurich.

Whiteman C. (2000): Mountain meteorology: fundamentals and applications. Oxford University Press.

Winkler S. (2009): Gletscher und ihre Landschaften. Wissenschaftliche Buchgesellschaft, Darmstadt.

Wyrwoll K., Dong B., Valdes P. (2000): On the position of southern hemisphere westerlies at the Last Glacial Maximum: an outline of AGCM simulation results and evaluation of their implications. Quaternary Science Reviews 19: 881-898.

Zech J., Zech R., Kubik P.W., Veit H. (resubmitted): Glacier and climate reconstruction at Tres Lagunas, NW Argentina, based on 10 Be surface exposure dating and lake sediment analyses. Palaeogeography, Palaeoclimatology, Palaeoecology.

Zech R., Kull C., Kubik P., Veit H. (2007a): Exposure dating of Late Glacial and pre-LGM moraines in the Cordon de Doña Rosa, northern Chile (~31°S). Climate of the Past 3: 1-14.

Zech R., Kull C., Kubik P., Veit H. (2007b): LGM and Late Glacial glacier advances in the Cordillera Real and Cochabamba (Bolivia) deduced from 10 Be surface exposure dating. Climate of the Past 3: 623-635.

Zech R., Kull C., Veit H. (2006): Late Quaternary glacial history in the Encierro Valley, northern Chile (29° S), deduced from 10Be surface exposure dating. Palaeogeography, Palaeoclimatology, Palaeoecology 234(2-4): 277-286.

Zech R., May J.-H., Kull C., Ilgner J., Kubik P.W., Veit H. (2008): Timing of the late Quaternary glaciation in the Andes from ~15 to 40° S. Journal of Quaternary Science 23(6-7): 635-647.

9 Appendices

Appendix I. Climate station data considered in this study

Station	m asl	Lat/Long	Period	Analyzed +	Derived +	Source
CAND1 wind	4515	33°05'S 70°15'W	04/06-10/08 *	T,W,RH		pers. comm. M. Zimmerli, Sensalpin GmbH, 2008
CAND2 snowdrift	3760	33°05'S 70°15'W	04/06-10/08 *	T,W,RH,Snow	T(Da)	pers. comm. M. Zimmerli, Sensalpin GmbH, 2008
CAND3 snow	4205	33°05'S 70°15'W	04/06-10/08 *	T,W,RH		pers. comm. M. Zimmerli, Sensalpin GmbH, 2008
CAND4 snowdrift	4425	33°05'S 70°15'W	04/06-10/08 *	T,W,RH	W(Ym,Ya)	pers. comm. M. Zimmerli, Sensalpin GmbH, 2008
Antofagasta	137	23°40'S 70°15'W	2000-2007	T(grad)		IGRA (NCDC)
Santo Domingo	75	33°35'S 71°35'W	1994-95,1998	T(grad)	T(grad)	IGRA (NCDC)
Mendoza	705	32°50'S 68°50'W	2002-2007	T(grad)		IGRA (NCDC)
Puerto Montt	90	41°30'S 72°50'W	2000-2007	T(grad)		IGRA (NCDC)
Punta Arenas	43	53°10'S 70°55'W	2000-2007	T(grad)		IGRA (NCDC)
Malargüe Aero	1425	35°58'S 69°44'W	1956-2008	T	T(Ym,Ya)	pers. comm. R. Neukom, GIUB, 2009
San Carlos	940	33°46'S 69°02'W	1956-2007	T	T(Ya)	pers. comm. R. Neukom, GIUB, 2009
San Rafael Aero	748	34°35'S 68°24'W	1967-2007	T	T(Ya)	pers. comm. R. Neukom, GIUB, 2009
Rama Caida	692	34°40'S 68°23'W	1969-1989	T	T(Ya)	pers. comm. R. Neukom, GIUB, 2009
Malargüe	1425	35°58'S 69°44'W	1993-2004	P	P(Ya)	GHCN (Peterson & Vose 1997)
San Carlos	940	33°46'S 69°02'W	1976-1998	P		GHCN (Peterson & Vose 1997)
San Rafael	748	34°35'S 68°24'W	1984-2000	P		GHCN (Peterson & Vose 1997)
Rama Caida	692	34°40'S 68°23'W	1986-2000	P		pers. comm. R. Neukom, GIUB, 2009
El Manzano	574	34°57'S 70°54'W	1976-2006	P	P(Ya)	pers. comm. R. Neukom, GIUB, 2009
Los Queñes	668	34°59'S 70°48'W	1976-2006	P	P(Ya)	pers. comm. R. Neukom, GIUB, 2009
Hornillo	810	35°52'S 71°07'W	1961-2007	P		pers. comm. R. Neukom, GIUB, 2009
Las Trancas	1200	36°54'S 71°30'W	1961-2007	P		pers. comm. R. Neukom, GIUB, 2009
San Lorenzo	850	36°58'S 71°31'W	1961-2007	P		pers. comm. R. Neukom, GIUB, 2009

* with interruptions

+ Abbreviations of the parameters according to chapter 4.1.1 (except snow)

Appendix II. AML Script for the modeling of global shortwave radiation

```
/* AML Script
/* Calculates global shortwave radiaton on Las Lenas paleoglacier.
/* Month: January / Scenario A: modern precipitation (920mm @ 2050m).
/* Calculation of the Ephemerides and the Declination for 35 ka BP.
/* Authors: T. Mölg, Mai 2001. Update: S. Imhof, 2005, P. Wäger, 2009.
/* workspace d:\masterarbeit\data\mod_shortwave_rad\Input_new_Rek_dem\35_B

grid
&setvar dem = d:\Masterarbeit\Data\mod_recglsurf\10453\15m\dere_10453_15
&setvar sloperad = d:\Masterarbeit\Data\mod_recglsurf\10453\15m\sloperad_dere
mape %dem%


/* STEP A: Definition of Constants
/* Pi, Latitude, Conversion factor RAD > DEG
&setvar pi = 3.1415926
&setvar lat = -35
&setvar radingrad = 180 / %pi%
&setvar obli = 22.75
&setvar oblirad = [angrad %obli%]


/* STEP B: Topography Analysis
/* Calculation of aspect south for shading analysis
as1 = aspect(%dem%)
DOCELL
as2 = 180 - as1
asud = asuedrad = as2 * 2 * %pi% / 360
END


/* Start LOOP 1. Day X to Day Y (z-steps)
&DO n = 1 &TO 31 &BY 1


/* STEP C: Definition of variables with seasonality:
/* Day angle, eccentricity correction factor, declination
/* Day angle. tau0@35 ka BP = Day angle 03.06. (timing of pericenter t0))
&setvar tau0 = 2.633773567
&setvar tau = 2 * %pi% * [calc %n% - 1] / 365
&type %tau%
&setvar 2tau = 2 * %tau%
&setvar 3tau = 3 * %tau%

/* kla = bracket term for calculation of solar declination after
/* Perrin de Brichambaut (Iqbal 1983:10)
&setvar kla = 360 / 365 * [calc %n% + 284]
&type %kla%

/* dtau = tau - tau0 = day angle - day angle @ perihel.
/* Needed for the calculation of the eccentric anomaly
&setvar dtau = [calc %tau% - %tau0%]
&type %dtau%

/* Eccentric anomaly (mean + amplitude)
```

```
&setvar ex = 1.00009158 + 0.03059718 * [cos %dtau%]

/* Solar declination in RAD
&setvar dekrad = %oblirad% * [sin [angrad %kla%]]
&type %ex%

/* Solar declination in DEG
&setvar dek = %dekrad% * %radingrad%


/* Start LOOP 2: stw = hour angle of the sun. sunrise to sunset (angle).
/* Steps: 7.5 degree / 0.5h
&DO stw = 101.25 &TO -101.25 &BY -7.5


/* STEP D: Definition of variables with diurnal cycles.
/* "bez" stands for "Bezeichnung" as "." is not valid in Gridname
/* Sinus of solar altitude in RAD
&setvar sinh = [sin [angrad %dek%]] * [sin [angrad %lat%]] + [cos [angrad
%dek%]] * [cos [angrad %lat%]] * [cos [angrad %stw%]]
&setvar h = [asin %sinh%] * %radingrad%
&type solar altitude done

/* Solar azimuth after Iqbal (1983, eq. 1.5.2b) (south=0, east=pos, west=neg)
&setvar sinaz = [cos[angrad %dek%]] * [sin [angrad %stw%]] / [cos [angrad %h%]]
&setvar az = 180 - [asin %sinaz%] * %radingrad%
&setvar bez = %stw% * 100
&type solar azimuth done

&type Shading for %n% / %stw% is being calculated...
schatjan = HILLSHADE(%dem%, %az%, %h%, shadow, 1)

&type Global radiation for day %n% / hour angle %stw% is being calculated...
/* Step 1: a Grid with the cos of the zenith distance of the sun
/* is produced for every cell (depending on time of day)
/* Step 2: the formula for global radiation is applied on the bright cells

coszdjan = (cos(%sloperad%) * [sin [angrad %lat%]] - [cos [angrad %lat%]] *
cos(asuedrad) * sin(%sloperad%)) * [sin [angrad %dek%]] + ([sin [angrad %lat%]]
* cos(asuedrad) * sin(%sloperad%) + cos(%sloperad%) * [cos [angrad %lat%]]) *
[cos [angrad %dek%]] * [cos [angrad %stw%]] + sin(asuedrad) * sin(%sloperad%) *
[cos [angrad %dek%]] * [sin [angrad %stw%]]


/* STEP E: Cloudiness
/* Match day and hours of Kull to day and hours of Mölg
/* Hour angles Mölg: noon = 0; Kull: midnight=0. Day consists of 24h
&setvar sth = 12 * %stw% / 180 + 12

/* Days Mölg: 1-365. Kull: 0-364 (with days as multiples of 24 hours
&setvar d = [calc %n% - 1] * 24

/* nt = Tag
&setvar t = [calc %d% + %sth%]
&setvar nt = [calc %t% / 24 * 0.98901 - 1]

/* Cloudiness as used in Kull's glacier-glimate model
/* Annual Mean and amplitude
&setvar JB = 5
&setvar JBa = 5

/* Second maximum
```

```
&setvar Wb = 10
&setvar WS = 65
&setvar Bg = 0.84

/* Definition of diurnal cycle
&setvar bta = 129
&setvar BTA1t = %bta% * [cos [angrad [calc 0.75 * %nt% - 15 * 360 / 365]]]
&setvar BTA2t = %bta% * [cos [angrad [calc 0.75 * %nt% - 375 * 360 / 365]]]

/* Summer cloudiness
&type Summer cloudiness for day %n%, hour %sth% is being calculated
&setvar wmax = [calc %t% + 5.5] / 0.0666667
&setvar sb1a = [calc %JB% + %JBa% * [cos [angrad [calc 0.5 * %nt% - 15 * 360 /
365]]]]
&setvar sb1b = %BTA1t% * [cos [angrad %wmax%]]
&type sb1a and sb1b done
&setvar sb2a = [calc %JB% + %JBa% * [cos [angrad [calc 0.5 * %nt% - 375 * 360 /
365]]]]
&setvar sb2b = %BTA2t% * [cos [angrad %wmax%]]
&type sb2a and sb2b done

DOCELL

sb1%n%z%bez% = %sb1a% + %sb1b%
&type sb1 done
sb2%n%z%bez% = %sb2a% + %sb2b%
&type sb2 done
sb%n%z%bez% = con(%t% lt 2521, sb1%n%z%bez%, con(%t% gt 6912, sb2%n%z%bez%, 0))
&type sb done
SBWt%n%z%bez% = con(sb%n%z%bez% gt 100, 100, con(sb%n%z%bez% lt 0, 0, con(%t% le
6912 & %t% ge 2521, 0, sb%n%z%bez%)))
&type SBWt > Summer cloudiness done

/* Winter cloudiness
&type Winter cloudiness for day %n%, hour %sth% is being calculated
wb%n%z%bez% = %Wb% + %WS% * [sin [angrad [calc %nt% - 105 * 360 / 365]]]
&type wbt done

WBWt%n%z%bez% = con(wb%n%z%bez% gt 100, 100, con(wb%n%z%bez% lt 0, 0, con(%t% le
6912 & %t% ge 2521, wb%n%z%bez%, 0)))
&type WBWt > Winter Cloudiness done

/* Annual cloudiness = summer + winter cloudiness
Bt%n%z%bez% = (WBWt%n%z%bez% + SBWt%n%z%bez%)DIV 100
A%n%z%bez% = con(Bt%n%z%bez% gt 100, 100, con(Bt%n%z%bez% lt 0, 0, Bt%n%z%bez%))
&type Bt > Annual Cloudiness (in percent) for Scenario A done


/* STEP F: Global shw radiation with cloudiness (only lighted cells considered)
if (coszdjan > 0)
 if (schatjan == 1)
      A%n%z%bez% = (1 - 0.68 * A%n%z%bez%) * 1438.5 * %ex% * coszdjan *
      (pow(0.907 DIV pow(%sinh%, 0.018), 1.3 DIV %sinh%))
 else
 A%n%z%bez% = 0
 else
 A%n%z%bez% = 0

END
&type shortwave global radiation (cloudiness Scenario A included) done
```

```
kill sb1%n%z%bez% all
kill sb2%n%z%bez% all
kill sb%n%z%bez% all
kill SBWt%n%z%bez% all
kill wb%n%z%bez% all
kill WBWt%n%z%bez% all
kill schatjan all
kill coszdjan all
kill Bt%n%z%bez% all

&END

/* Daily mean global shw radiation
&type shortwave radiation mean for day %n% / jan is being calculated...
A%n% = mean (A%n%z-10125, A%n%z-9375, A%n%z-8625, A%n%z-7875, A%n%z-7125, A%n%z-
6375, A%n%z-5625, A%n%z-4875, A%n%z-4125, A%n%z-3375, A%n%z-2625, A%n%z-1875,
A%n%z-1125, A%n%z-375, A%n%z375, A%n%z1125, A%n%z1875, A%n%z2625, A%n%z3375,
A%n%z4125, A%n%z4875, A%n%z5625, A%n%z6375, A%n%z7125, A%n%z7875, A%n%z8625,
A%n%z9375, A%n%z10125)

&type specifinc hourly grids for day %n% / jan are being deleted...
&DO bez = -10125 &TO 10125 &BY 750
kill A%n%z%bez% all

&END
&END

/* Monthly mean global shw radiation
&type shortwave radiation mean for jan / scenario A is being calculated...

jan_A_w = mean (A1, A2, A3, A4, A5, A6, A7, A8, A9, A10, A1, A12, A13, A14, A15,
A16, A17, A18, A19, A20, A21, A22, A23, A24, A25, A26, A27, A28, A29, A30, A31)

&type specific daily grids for jan /scenario B are being deleted...
&DO n = 1 &TO 31 &BY 1
kill A%n% all
&END

/* Conversion
&type Conversion W/m^2 to kWh/m^2
jan_35_A = jan_A_w / 1000 * 14
kill jan_A_w all

&type Calculation for jan: completed!
q
&return
```

Appendix III. AML Script for the reconstruction of the former glacier surface

```
/* AML Script
/* Calculates ice thickness in the ablation area of Las Lenas paleoglacier.
/* Author: R. Sailer, 1999.
/* workspace d:\masterarbeit\data\mod_recglsurf


/* Definition of constants
&setvar ro = 900
&setvar g = 9.81
&setvar pi = 3.14159265
&setvar tau = 104000

grid

DOCELL

/* Calculating ice thickness by using the statistical relationship between
/* surface and bed slope established on the Gepatschferner in Austria
ll_ice_ak_104 = %tau% / (%ro% * %g% * sin ((slope_deg_akk + 4.34 - 0.82 *
slope_deg_akk) * %pi% / 180))

END

/* New DEM = Basis DEM plus ice thickness
ll_of_akk_fmx = ll_ice_ak_104 + ll_dem_akk

/* Smoothing
ll_of_akk_fm1 = focalmean(ll_of_akk_fmx, rectangle, 5, 5)
ll_of_akk_fm2 = focalmean(ll_of_akk_fm1, rectangle, 5, 5)

kill ll_of_akk_fmx
kill ll_of_akk_fm1 all

DOCELL
if (ll_dem_akk ge 1000)
ll_rec_104_55 = ll_of_akk_fm2
END

kill ll_of_akk_fm2 all
hs_rec_104_55 = hillshade(ll_rec_104_55)

q
&return
```

Appendix IV. Modeled global shortwave global radiation [kwh/m^2*d]

Scenario (Timing_Cloudiness)	m asl	h	jan	feb	mrz	apr	may	jun	jul	aug	sep	okt	nov	dez
0_0	2150	1	10.48	9.49	7.81	5.81	4.23	3.52	3.81	5.08	6.97	8.85	10.19	10.71
	2250	2	10.47	9.60	8.01	6.07	4.51	3.79	4.10	5.36	7.19	8.97	10.19	10.70
	2350	3	10.42	9.48	7.86	5.89	4.29	3.54	3.86	5.16	7.03	8.87	10.10	10.61
	2450	4	10.31	9.30	7.57	5.52	3.90	3.16	3.48	4.79	6.71	8.65	10.00	10.53
	2550	5	10.12	9.10	7.34	5.24	3.58	2.84	3.16	4.49	6.47	8.43	9.81	10.36
	2650	6	9.82	8.80	7.05	5.00	3.36	2.62	2.94	4.27	6.19	8.14	9.48	10.01
	2750	7	9.63	8.63	6.93	4.91	3.32	2.60	2.92	4.20	6.09	7.99	9.32	9.84
	2850	8	9.47	8.49	6.86	4.89	3.32	2.62	2.92	4.18	6.04	7.87	9.15	9.66
	2950	9	9.47	8.52	6.92	4.97	3.38	2.66	2.98	4.26	6.12	7.91	9.17	9.66
	3050	10	9.46	8.49	6.89	4.97	3.41	2.69	3.01	4.27	6.10	7.88	9.15	9.65
	3150	11	9.56	8.53	6.89	4.95	3.39	2.67	2.99	4.25	6.08	7.90	9.23	9.77
	3250	12	10.07	9.00	7.30	5.34	3.77	3.04	3.36	4.63	6.48	8.34	9.73	10.31
	3350	13	10.21	9.12	7.41	5.45	3.88	3.17	3.48	4.75	6.59	8.46	9.87	10.47
	3450	14	10.11	9.01	7.27	5.30	3.74	3.03	3.34	4.59	6.44	8.34	9.76	10.36
	3550	15	10.00	8.82	7.01	5.01	3.47	2.79	3.08	4.31	6.17	8.13	9.63	10.26
	3650	16	10.00	8.69	6.73	4.63	3.06	2.39	2.68	3.91	5.85	7.94	9.59	10.28
	3750	17	10.24	8.93	6.96	4.81	3.20	2.51	2.81	4.08	6.06	8.19	9.84	10.54
0_A	2150	1	8.22	7.55	6.48	5.11	3.05	1.96	1.89	2.84	5.04	7.78	8.45	8.51
	2250	2	8.07	7.49	6.53	5.30	3.25	2.11	2.03	2.99	5.19	7.83	8.31	8.36
	2350	3	7.88	7.25	6.30	5.10	3.10	1.97	1.91	2.89	5.08	7.69	8.09	8.12
	2450	4	7.66	7.00	5.97	4.76	2.82	1.75	1.72	2.68	4.85	7.45	7.89	7.92
	2550	5	7.46	6.81	5.75	4.50	2.59	1.58	1.56	2.51	4.68	7.24	7.69	7.75
	2650	6	7.26	6.60	5.53	4.29	2.43	1.46	1.46	2.39	4.48	6.99	7.44	7.51
	2750	7	7.09	6.44	5.42	4.21	2.40	1.44	1.44	2.35	4.40	6.85	7.29	7.35
	2850	8	6.89	6.25	5.30	4.17	2.40	1.46	1.45	2.34	4.37	6.71	7.07	7.11
	2950	9	6.89	6.27	5.35	4.24	2.45	1.48	1.48	2.38	4.42	6.75	7.08	7.12
	3050	10	6.86	6.24	5.32	4.24	2.47	1.49	1.49	2.39	4.41	6.72	7.05	7.09
	3150	11	6.98	6.30	5.34	4.23	2.45	1.49	1.48	2.38	4.40	6.75	7.15	7.21
	3250	12	7.62	6.89	5.85	4.63	2.72	1.69	1.66	2.59	4.68	7.24	7.80	7.90
	3350	13	7.84	7.08	6.02	4.76	2.81	1.76	1.72	2.65	4.76	7.38	8.02	8.13
	3450	14	7.74	6.99	5.91	4.62	2.70	1.69	1.65	2.57	4.65	7.28	7.93	8.04
	3550	15	7.34	6.56	5.49	4.30	2.51	1.55	1.53	2.41	4.46	6.99	7.53	7.63
	3650	16	7.22	6.35	5.18	3.95	2.21	1.33	1.33	2.19	4.23	6.78	7.37	7.52
	3750	17	7.65	6.75	5.52	4.16	2.32	1.40	1.39	2.29	4.38	7.07	7.80	7.97
0_A ELA_3000	2150	1	8.22	7.55	6.47	5.10	3.05	1.95	1.88	2.84	5.03	7.77	8.44	8.51
	2250	2	8.07	7.49	6.53	5.30	3.25	2.11	2.03	2.99	5.19	7.83	8.31	8.36
	2350	3	7.88	7.25	6.30	5.10	3.10	1.97	1.91	2.89	5.08	7.69	8.09	8.12
	2450	4	7.66	7.00	5.97	4.76	2.82	1.75	1.72	2.68	4.85	7.45	7.89	7.92
	2550	5	7.36	6.74	5.74	4.53	2.62	1.60	1.59	2.54	4.69	7.29	7.67	7.68
	2650	6	7.29	6.62	5.54	4.28	2.42	1.45	1.45	2.38	4.46	6.97	7.45	7.54
	2750	7	7.23	6.55	5.48	4.27	2.46	1.50	1.49	2.39	4.46	6.95	7.38	7.47
	2850	8	6.98	6.29	5.27	4.12	2.35	1.42	1.41	2.31	4.38	6.64	7.04	7.16
	2950	9	7.29	6.58	5.53	4.25	2.33	1.35	1.38	2.35	4.48	6.77	7.32	7.46
	3050	10	7.10	6.31	5.20	3.95	2.17	1.25	1.28	2.18	4.22	6.26	6.89	7.17
	3150	11	7.13	6.34	5.24	4.03	2.26	1.34	1.35	2.23	4.25	6.42	7.02	7.25
	3250	12	7.81	7.03	5.93	4.64	2.70	1.67	1.65	2.58	4.69	7.25	7.90	8.06
	3350	13	7.94	7.17	6.09	4.79	2.82	1.77	1.73	2.66	4.78	7.43	8.11	8.23
	3450	14	7.74	6.99	5.92	4.64	2.72	1.70	1.66	2.58	4.66	7.30	7.95	8.05
	3550	15	7.33	6.55	5.48	4.30	2.51	1.55	1.53	2.41	4.46	6.98	7.52	7.62
	3650	16	7.22	6.35	5.17	3.94	2.21	1.33	1.33	2.19	4.23	6.77	7.37	7.51
	3750	17	7.64	6.75	5.52	4.15	2.31	1.39	1.39	2.28	4.38	7.07	7.80	7.97
35_0	2150	1	9.84	9.13	7.75	6.01	4.54	3.85	4.13	5.32	7.01	8.57	9.62	10.01
	2250	2	9.86	9.23	7.95	6.28	4.83	4.15	4.44	5.61	7.23	8.69	9.62	10.01
	2350	3	9.81	9.11	7.81	6.09	4.61	3.89	4.18	5.41	7.07	8.59	9.54	9.92
	2450	4	9.69	8.94	7.51	5.71	4.20	3.47	3.79	5.02	6.74	8.37	9.44	9.84
	2550	5	9.51	8.74	7.28	5.42	3.86	3.14	3.45	4.71	6.50	8.16	9.25	9.68
	2650	6	9.22	8.45	7.00	5.17	3.63	2.91	3.22	4.48	6.22	7.88	8.94	9.35
	2750	7	9.05	8.28	6.88	5.08	3.59	2.88	3.19	4.41	6.12	7.73	8.79	9.19
	2850	8	8.90	8.15	6.81	5.06	3.58	2.90	3.20	4.39	6.07	7.62	8.63	9.02
	2950	9	8.90	8.19	6.87	5.14	3.65	2.95	3.26	4.47	6.15	7.66	8.65	9.03
	3050	10	8.89	8.16	6.85	5.15	3.68	2.98	3.29	4.48	6.13	7.63	8.63	9.01
	3150	11	8.98	8.19	6.84	5.12	3.66	2.96	3.27	4.46	6.11	7.65	8.70	9.12
	3250	12	9.46	8.64	7.25	5.53	4.06	3.35	3.66	4.86	6.51	8.08	9.17	9.62
	3350	13	9.59	8.76	7.36	5.64	4.18	3.49	3.78	4.97	6.62	8.18	9.30	9.77
	3450	14	9.50	8.65	7.22	5.48	4.02	3.34	3.63	4.81	6.47	8.07	9.20	9.67
	3550	15	9.39	8.47	6.96	5.18	3.74	3.08	3.36	4.52	6.20	7.86	9.07	9.56
	3650	16	9.37	8.33	6.68	4.79	3.31	2.65	2.93	4.11	5.88	7.68	9.02	9.58
	3750	17	9.61	8.57	6.91	4.98	3.46	2.78	3.07	4.29	6.09	7.91	9.26	9.82

Appendix IV. Modeled global shortwave global radiation [kwh/m^2*d] (continuation)

Scenario (Timing_Cloudiness)	m asl	h	jan	feb	mrz	apr	may	jun	jul	aug	sep	okt	nov	dez
35_A	2150	1	7.72	7.26	6.43	5.28	3.28	2.14	2.05	2.97	5.06	7.53	7.98	7.96
	2250	2	7.60	7.21	6.49	5.48	3.48	2.31	2.20	3.13	5.21	7.59	7.85	7.82
	2350	3	7.42	6.97	6.26	5.28	3.32	2.16	2.07	3.02	5.10	7.45	7.65	7.59
	2450	4	7.20	6.73	5.93	4.92	3.03	1.93	1.88	2.81	4.87	7.21	7.45	7.41
	2550	5	7.02	6.54	5.71	4.66	2.79	1.74	1.71	2.64	4.69	7.01	7.25	7.24
	2650	6	6.82	6.34	5.50	4.44	2.63	1.61	1.60	2.51	4.49	6.77	7.02	7.01
	2750	7	6.67	6.19	5.38	4.36	2.59	1.60	1.58	2.47	4.42	6.63	6.87	6.86
	2850	8	6.48	6.00	5.26	4.32	2.59	1.61	1.58	2.46	4.39	6.50	6.67	6.64
	2950	9	6.48	6.03	5.31	4.39	2.64	1.64	1.61	2.50	4.44	6.54	6.68	6.65
	3050	10	6.45	5.99	5.28	4.39	2.66	1.66	1.63	2.51	4.43	6.51	6.65	6.62
	3150	11	6.56	6.05	5.30	4.38	2.64	1.64	1.62	2.49	4.41	6.54	6.75	6.73
	3250	12	7.16	6.62	5.81	4.79	2.93	1.86	1.81	2.72	4.70	7.00	7.36	7.37
	3350	13	7.37	6.81	5.98	4.92	3.02	1.94	1.87	2.78	4.78	7.14	7.56	7.59
	3450	14	7.28	6.71	5.86	4.78	2.91	1.85	1.80	2.69	4.67	7.04	7.47	7.51
	3550	15	6.89	6.30	5.45	4.46	2.70	1.71	1.66	2.53	4.48	6.76	7.10	7.12
	3650	16	6.77	6.09	5.14	4.09	2.39	1.47	1.45	2.30	4.25	6.56	6.94	7.00
	3750	17	7.17	6.48	5.48	4.31	2.50	1.54	1.52	2.40	4.40	6.84	7.34	7.43
35_A ELA_3000	2150	1	7.72	7.26	6.43	5.27	3.27	2.14	2.04	2.97	5.05	7.53	7.97	7.96
	2250	2	7.60	7.21	6.49	5.48	3.48	2.30	2.20	3.13	5.21	7.59	7.85	7.82
	2350	3	7.42	6.97	6.26	5.27	3.32	2.16	2.07	3.02	5.10	7.45	7.64	7.59
	2450	4	7.20	6.73	5.93	4.92	3.03	1.93	1.87	2.81	4.86	7.21	7.45	7.41
	2550	5	6.93	6.48	5.70	4.69	2.83	1.77	1.73	2.66	4.71	6.97	7.16	7.12
	2650	6	6.86	6.36	5.50	4.43	2.61	1.61	1.59	2.49	4.48	6.77	7.06	7.07
	2750	7	6.80	6.29	5.44	4.42	2.66	1.65	1.62	2.51	4.48	6.75	7.00	7.00
	2850	8	6.56	6.04	5.24	4.27	2.54	1.57	1.55	2.43	4.40	6.58	6.76	6.75
	2950	9	6.85	6.32	5.49	4.40	2.53	1.51	1.51	2.47	4.50	6.77	7.05	7.05
	3050	10	6.66	6.05	5.16	4.09	2.35	1.40	1.41	2.29	4.23	6.48	6.83	6.88
	3150	11	6.69	6.08	5.20	4.17	2.44	1.49	1.48	2.35	4.27	6.50	6.86	6.89
	3250	12	7.34	6.75	5.89	4.80	2.91	1.85	1.80	2.70	4.71	7.08	7.53	7.56
	3350	13	7.46	6.89	6.05	4.95	3.03	1.94	1.88	2.79	4.80	7.19	7.65	7.69
	3450	14	7.28	6.72	5.88	4.80	2.92	1.87	1.81	2.70	4.68	7.04	7.47	7.51
	3550	15	6.88	6.29	5.44	4.45	2.70	1.71	1.66	2.53	4.47	6.76	7.09	7.11
	3650	16	6.77	6.09	5.14	4.09	2.39	1.47	1.45	2.30	4.25	6.55	6.94	7.00
	3750	17	7.17	6.48	5.47	4.30	2.50	1.54	1.52	2.40	4.40	6.84	7.34	7.43
35_B	2150	1	7.72	7.26	6.43	4.88	2.79	1.87	1.82	2.60	4.30	6.96	7.98	7.96
	2250	2	7.60	7.21	6.49	5.05	2.96	2.02	1.95	2.74	4.43	7.00	7.85	7.82
	2350	3	7.42	6.97	6.26	4.87	2.83	1.89	1.84	2.64	4.34	6.87	7.65	7.59
	2450	4	7.20	6.73	5.93	4.54	2.58	1.69	1.66	2.45	4.14	6.65	7.45	7.41
	2550	5	7.02	6.54	5.71	4.30	2.37	1.52	1.52	2.30	3.99	6.47	7.25	7.24
	2650	6	6.82	6.34	5.50	4.10	2.23	1.41	1.42	2.19	3.82	6.25	7.02	7.01
	2750	7	6.67	6.19	5.38	4.02	2.21	1.40	1.40	2.16	3.76	6.11	6.87	6.86
	2850	8	6.48	6.00	5.26	3.98	2.20	1.41	1.41	2.15	3.73	6.00	6.67	6.64
	2950	9	6.48	6.03	5.31	4.05	2.24	1.44	1.43	2.19	3.77	6.03	6.68	6.65
	3050	10	6.45	5.99	5.28	4.05	2.26	1.45	1.45	2.19	3.76	6.00	6.65	6.62
	3150	11	6.56	6.05	5.30	4.04	2.25	1.44	1.44	2.18	3.75	6.03	6.75	6.73
	3250	12	7.16	6.62	5.81	4.42	2.49	1.63	1.61	2.37	4.00	6.46	7.36	7.37
	3350	13	7.37	6.81	5.98	4.54	2.56	1.69	1.66	2.43	4.06	6.59	7.56	7.59
	3450	14	7.28	6.71	5.86	4.41	2.47	1.62	1.60	2.35	3.97	6.50	7.47	7.51
	3550	15	6.89	6.30	5.45	4.11	2.29	1.50	1.48	2.21	3.81	6.24	7.10	7.12
	3650	16	6.77	6.09	5.14	3.77	2.03	1.29	1.29	2.01	3.61	6.05	6.94	7.00
	3750	17	7.17	6.48	5.48	3.98	2.13	1.35	1.35	2.10	3.74	6.32	7.34	7.43
35_C	2150	1	7.72	7.26	6.43	4.41	2.25	1.61	1.61	2.24	3.47	6.29	7.98	7.96
	2250	2	7.60	7.21	6.49	4.56	2.39	1.74	1.73	2.35	3.57	6.32	7.85	7.82
	2350	3	7.42	6.97	6.26	4.39	2.28	1.62	1.63	2.27	3.50	6.20	7.65	7.59
	2450	4	7.20	6.73	5.93	4.10	2.08	1.45	1.48	2.11	3.34	6.00	7.45	7.41
	2550	5	7.02	6.54	5.71	3.88	1.91	1.31	1.35	1.98	3.22	5.84	7.25	7.24
	2650	6	6.82	6.34	5.50	3.70	1.80	1.22	1.26	1.88	3.08	5.64	7.02	7.01
	2750	7	6.67	6.19	5.38	3.63	1.78	1.21	1.25	1.85	3.03	5.52	6.87	6.86
	2850	8	6.48	6.00	5.26	3.59	1.77	1.21	1.25	1.84	3.01	5.41	6.67	6.64
	2950	9	6.48	6.03	5.31	3.65	1.81	1.24	1.27	1.88	3.04	5.44	6.68	6.65
	3050	10	6.45	5.99	5.28	3.65	1.82	1.25	1.28	1.88	3.03	5.41	6.65	6.62
	3150	11	6.56	6.05	5.30	3.64	1.81	1.24	1.27	1.87	3.03	5.44	6.75	6.73
	3250	12	7.16	6.62	5.81	3.99	2.01	1.40	1.43	2.04	3.22	5.84	7.36	7.37
	3350	13	7.37	6.81	5.98	4.10	2.07	1.46	1.48	2.09	3.28	5.95	7.56	7.59
	3450	14	7.28	6.71	5.86	3.99	1.99	1.40	1.42	2.02	3.20	5.87	7.47	7.51
	3550	15	6.89	6.30	5.45	3.71	1.85	1.29	1.31	1.90	3.07	5.63	7.10	7.12
	3650	16	6.77	6.09	5.14	3.41	1.64	1.11	1.15	1.73	2.91	5.46	6.94	7.00
	3750	17	7.17	6.48	5.48	3.60	1.71	1.16	1.20	1.80	3.02	5.71	7.34	7.43

Appendix V. 2D Modeling results

PRECIPITATION		Best Guess	Temp. Gradient		Cloudiness		Degree Day Factor				Prec. Gradient				Prec. Cooling		Mapping	Prec. Source		< Parameter varied
P [mm]	dP [mm]	Best Guess	-0.53	-0.73	*2	*3	*1.2	*1.1	*0.9	*0.8	*1.5	*1.2	*0.8	*0.5	4°C	3°C	ELA3000	SP_inc	SP_only	< Variation
3535	2615	4.4	3.5	5.4	4.5	4.5	3.6	4.0	5.0	5.7	4.6	4.5	4.4	4.3	4.9	5.0	4.4			
2339	1419	2.4	1.5	3.2	2.4	2.5	1.7	2.0	2.8	3.3	2.6	2.4	2.3	2.2	2.7	3.0	2.2	2.9		
1492	572	0.3	-0.5	1.1	0.4	0.5	-0.3	0.0	0.6	1.0	0.5	0.4	0.2	0.0	0.6	0.9	0.1	1.0	1.1	TEMP
920	0	-1.8	-2.5	-1.1	-1.6	-1.6	-2.2	-2.0	-1.5	-1.2	-1.5	-1.7	-1.9	-2.2	-1.5	-1.1	-2.1	-1.8	-0.7	at 2050m asl. [°C]
565	-355	-3.9	-4.6	-3.3	-3.6	-3.4	-4.2	-4.1	-3.7	-3.5	-3.4	-3.7	-4.1	-4.5	-3.6	-3.1	-4.2		-2.9	
373	-547	-6.0	-6.5	-5.5	-5.5	-5.1	-6.2	-6.1	-5.8	-5.7	-5.0	-5.6	-6.4	-7.4	-5.8	-5.2	-6.3		-5.3	
3535	2615	-3.7	-4.6	-2.7	-3.6	-3.6	-4.5	-4.1	-3.1	-2.5	-3.5	-3.6	-3.7	-3.9	-3.3	-3.5	-3.7			
2339	1419	-5.8	-6.7	-4.9	-5.7	-5.6	-6.5	-6.1	-5.3	-4.8	-5.6	-5.7	-5.8	-6.0	-5.4	-5.6	-5.9	-5.2		
1492	572	-7.8	-8.6	-7.1	-7.7	-7.6	-8.4	-8.1	-7.5	-7.1	-7.6	-7.7	-7.9	-8.1	-7.5	-7.7	-8.1	-7.1	-7.0	TEMP
920	0	-9.9	-10.7	-9.3	-9.8	-9.8	-10.4	-10.2	-9.7	-9.4	-9.6	-9.8	-10.1	-10.3	-9.7	-9.8	-10.2	-9.9	-8.8	DEPRESSION at
565	-355	-12.0	-12.7	-11.4	-11.8	-11.5	-12.3	-12.2	-11.8	-11.6	-11.5	-11.8	-12.2	-12.6	-11.8	-11.9	-12.3		-11.0	2050m asl. [°C]
373	-547	-14.1	-14.6	-13.6	-13.6	-13.2	-14.4	-14.2	-13.9	-13.8	-13.2	-13.7	-14.6	-15.5	-14.0	-14.0	-14.4		-13.5	
3535	2615	-2.0	-2.0	-2.0	-2.0	-1.9	-2.9	-2.5	-1.5	-0.9	-1.9	-2.0	-2.1	-2.2	-1.6	-1.8	-2.1			
2339	1419	-3.9	-3.9	-3.9	-3.8	-3.8	-4.5	-4.2	-3.5	-3.0	-3.7	-3.8	-4.0	-4.1	-3.4	-3.6	-3.9	-3.4		
1492	572	-5.6	-5.6	-5.6	-5.5	-5.4	-6.1	-5.9	-5.3	-4.9	-5.4	-5.5	-5.7	-5.8	-5.2	-5.3	-5.7	-4.9	-4.8	TEMP
920	0	-7.4	-7.3	-7.4	-7.2	-7.1	-7.8	-7.6	-7.1	-6.8	-7.1	-7.2	-7.5	-7.6	-7.1	-7.2	-7.4	-7.4	-6.2	at ELA [°C]
565	-355	-9.2	-9.1	-9.3	-9.0	-8.7	-9.5	-9.4	-9.0	-8.8	-8.8	-9.0	-9.4	-9.7	-9.1	-9.2	-9.4		-8.1	
373	-547	-10.9	-10.9	-10.9	-10.6	-10.2	-11.0	-11.0	-10.8	-10.7	-10.3	-10.7	-11.2	-10.9	-10.9	-10.9	-10.9		-10.1	
3535	2615	3659	3661	3658	3659	3659	3658	3659	3659	3660	3722	3684	3634	3597	3658	3659	3658			
2339	1419	2459	2461	2457	2459	2459	2457	2458	2460	2460	2519	2483	2435	2399	2456	2457	2457	2460		
1492	572	1605	1608	1602	1605	1606	1604	1604	1606	1606	1661	1627	1582	1548	1602	1603	1602	1606	1606	PREC.
920	0	1026	1029	1023	1027	1027	1026	1026	1026	1027	1080	1048	1005	973	1027	1026	1023	1026	1026	at ELA [mm]
565	-355	667	670	664	667	668	667	667	667	667	720	688	646	615	671	669	664		661	
373	-547	467	472	463	470	472	465	466	468	468	523	490	447	407	470	469	460		465	
3535	2615	3080	3093	3067	3080	3067	3073	3077	3082	3083	3084	3081	3078	3076	3073	3079	3073			
2339	1419	3044	3063	3025	3045	3025	3031	3038	3051	3057	3047	3046	3043	3041	3017	3031	3029	3045		
1492	572	2985	3008	2964	2988	2964	2976	2980	2992	2999	2988	2987	2984	2983	2963	2970	2963	2995	3000	ELA
920	0	2931	2958	2905	2934	2905	2928	2929	2932	2935	2939	2934	2928	2922	2941	2929	2902	2931	2925	[m asl.]
565	-355	2893	2924	2867	2898	2867	2893	2894	2894	2893	2909	2901	2886	2872	2925	2910	2867		2864	
373	-547	2828	2871	2792	2856	2792	2812	2821	2837	2841	2883	2861	2810	2605	2853	2843	2768		2815	
3535	2615	-844	-831	-857	-844	-857	-851	-847	-842	-841	-840	-843	-846	-848	-851	-845	-851			
2339	1419	-880	-861	-899	-879	-899	-893	-886	-873	-867	-877	-878	-881	-883	-907	-893	-895	-879		
1492	572	-939	-916	-960	-936	-960	-948	-944	-932	-925	-936	-937	-940	-941	-961	-954	-961	-929	-924	ELA
920	0	-993	-966	-1019	-990	-1019	-996	-995	-992	-989	-985	-990	-996	-1002	-983	-995	-1022	-993	-999	DEPRESSION
565	-355	-1031	-1000	-1057	-1026	-1057	-1031	-1030	-1030	-1031	-1015	-1023	-1038	-1052	-999	-1014	-1057		-1060	[m]
373	-547	-1096	-1053	-1132	-1068	-1132	-1112	-1103	-1087	-1083	-1041	-1063	-1114	-1319	-1071	-1081	-1156		-1109	
3535	2615	0.72	0.71	0.72	0.72	0.72	0.72	0.72	0.71	0.71	0.71	0.71	0.72	0.72	0.72	0.72	0.73			
2339	1419	0.73	0.72	0.74	0.73	0.73	0.74	0.74	0.73	0.73	0.73	0.73	0.73	0.74	0.75	0.74	0.74	0.73		
1492	572	0.76	0.75	0.77	0.76	0.76	0.77	0.76	0.76	0.76	0.76	0.76	0.76	0.76	0.77	0.77	0.76	0.76	0.75	AAR
920	0	0.79	0.77	0.80	0.78	0.78	0.79	0.79	0.78	0.78	0.78	0.78	0.79	0.79	0.78	0.79	0.78	0.79	0.79	
565	-355	0.80	0.79	0.81	0.80	0.80	0.80	0.80	0.80	0.80	0.79	0.80	0.80	0.81	0.79	0.79	0.78		0.81	
373	-547	0.82	0.81	0.84	0.81	0.81	0.83	0.83	0.82	0.82	0.80	0.81	0.83	0.89	0.82	0.82	0.81		0.83	
3535	2615	12.5	10.6	14.5	12.6	12.8	13.0	12.8	12.3	12.2	12.8	12.6	12.4	12.2	13.3	12.9	12.4			
2339	1419	10.5	8.5	12.2	10.7	10.8	11.1	10.8	9.8	9.5	10.9	10.7	10.4	10.2	11.2	10.9	10.4	11.6		Ablation area
1492	572	8.2	6.9	9.6	8.4	8.6	8.7	8.5	8.0	7.8	8.6	8.4	8.1	7.8	8.6	8.5	8.0	9.1	9.5	Mass balance
920	0	6.4	4.9	7.5	6.6	6.8	6.7	6.6	6.2	6.0	6.9	6.6	6.2	5.9	6.5	6.5	6.1	6.4	7.7	gradient
565	-355	4.1	3.3	4.9	4.4	4.7	4.3	4.2	4.0	3.9	4.7	4.4	3.8	3.3	4.0	4.0	3.7		4.8	
373	-547	2.3	1.6	2.9	2.5	2.9	2.5	2.4	2.3	2.2	3.1	2.5	1.9	1.4	1.9	2.2	2.1		2.7	[$kgm^{-2}m^{-1}$]

Appendix VI. 3D Modeling results

DMM Values with polygonic cross section shape (positive values gray shaded)

	Mass balance scenario >		Best Guess						GTF - 20%					
		P[mm] >	3535	2339	1492	920	565	373	3535	2339	1492	920	565	373
	Cross Section	dP[mm] >	2615	1419	572	0	-355	-547	2615	1419	572	0	-355	-547
	2500	Total mass	-1.1E+10	-8.6E+09	-6.4E+09	-4.3E+09	-2.5E+09	-1.3E+09	-1.1E+10	-8.3E+09	-6.2E+09	-4.2E+09	-2.5E+09	-1.3E+09
	2400	balance below	-7.7E+09	-6.0E+09	-4.5E+09	-3.1E+09	-1.9E+09	-9.8E+08	-7.5E+09	-5.8E+09	-4.4E+09	-3.0E+09	-1.8E+09	-9.5E+08
	2340	cross section	-6.3E+09	-5.0E+09	-3.7E+09	-2.6E+09	-1.6E+09	-8.3E+08	-6.2E+09	-4.8E+09	-3.6E+09	-2.5E+09	-1.5E+09	-8.0E+08
Ice flow scenario	Cross Section (polygonic)	Mass influx into cross section	DMM (Difference between mass influx and total mass balance below the cross section) Best Guess mass balance scenario						DMM (Difference between mass influx and total mass balance below the cross section) DDF -20% mass balance scenario					
Best Guess	2500	1.68E+09	-9.3E+09	-7.0E+09	-4.7E+09	-2.6E+09	-8.6E+08	3.7E+08	-9.1E+09	-6.6E+09	-4.5E+09	-2.5E+09	-7.9E+08	4.1E+08
	2400	1.97E+08	-7.5E+09	-5.9E+09	-4.3E+09	-2.9E+09	-1.7E+09	-7.9E+08	-7.3E+09	-5.6E+09	-4.2E+09	-2.8E+09	-1.6E+09	-7.5E+08
	2340	8.42E+07	-6.2E+09	-4.9E+09	-3.7E+09	-2.5E+09	-1.5E+09	-7.5E+08	-6.1E+09	-4.7E+09	-3.5E+09	-2.4E+09	-1.4E+09	-7.2E+08
flow parameters *2	2500	3.37E+09	-7.7E+09	-5.3E+09	-3.0E+09	-9.4E+08	8.3E+08	2.0E+09	-7.4E+09	-5.0E+09	-2.8E+09	-8.2E+08	8.9E+08	2.1E+09
	2400	3.94E+08	-7.3E+09	-5.7E+09	-4.1E+09	-2.7E+09	-1.5E+09	-5.9E+08	-7.1E+09	-5.4E+09	-4.0E+09	-2.6E+09	-1.4E+09	-5.5E+08
	2340	1.68E+08	-6.2E+09	-4.8E+09	-3.6E+09	-2.4E+09	-1.4E+09	-6.6E+08	-6.0E+09	-4.6E+09	-3.4E+09	-2.3E+09	-1.4E+09	-6.3E+08
flow parameters *4	2500	6.73E+09	-4.3E+09	-1.9E+09	3.4E+08	2.4E+09	4.2E+09	5.4E+09	-4.0E+09	-1.6E+09	5.6E+08	2.6E+09	4.3E+09	5.5E+09
	2400	7.88E+08	-6.9E+09	-5.3E+09	-3.7E+09	-2.3E+09	-1.1E+09	-2.0E+08	-6.7E+09	-5.0E+09	-3.6E+09	-2.2E+09	-1.0E+09	-1.6E+08
	2340	3.37E+08	-6.0E+09	-4.6E+09	-3.4E+09	-2.2E+09	-1.2E+09	-4.9E+08	-5.8E+09	-4.5E+09	-3.3E+09	-2.2E+09	-1.2E+09	-4.6E+08
slope = 0.12	2500	1.68E+09	-9.3E+09	-7.0E+09	-4.7E+09	-2.6E+09	-8.6E+08	3.7E+08	-9.1E+09	-6.6E+09	-4.5E+09	-2.5E+09	-7.9E+08	4.1E+08
	2400	5.60E+08	-7.1E+09	-5.5E+09	-4.0E+09	-2.5E+09	-1.3E+09	-4.2E+08	-6.9E+09	-5.3E+09	-3.8E+09	-2.4E+09	-1.3E+09	-3.9E+08
	2340	2.39E+08	-6.1E+09	-4.7E+09	-3.5E+09	-2.3E+09	-1.3E+09	-5.9E+08	-5.9E+09	-4.6E+09	-3.4E+09	-2.3E+09	-1.3E+09	-5.6E+08
F = 0.9	2500	8.85E+09	-2.2E+09	2.1E+08	2.5E+09	4.5E+09	6.3E+09	7.5E+09	-1.9E+09	5.3E+08	2.7E+09	4.7E+09	6.4E+09	7.6E+09
	2400	1.00E+09	-6.7E+09	-5.0E+09	-3.5E+09	-2.1E+09	-8.7E+08	1.7E+07	-6.5E+09	-4.8E+09	-3.4E+09	-2.0E+09	-8.2E+08	5.3E+07
	2340	4.20E+08	-5.9E+09	-4.6E+09	-3.3E+09	-2.2E+09	-1.1E+09	-4.1E+08	-5.8E+09	-4.4E+09	-3.2E+09	-2.1E+09	-1.1E+09	-3.8E+08

Appendix VI. 3D Modeling (continuation).

DMM Values with trapezoidal cross section shape (positive values gray shaded)

	Mass balance scenario >		Best Guess						GTF - 20%					
		P[mm] >	3535	2339	1492	920	565	373	3535	2339	1492	920	565	373
	Cross Section	dP[mm] >	2615	1419	572	0	-355	-547	2615	1419	572	0	-355	-547
	2500	Total mass	-1.1E+10	-8.6E+09	-6.4E+09	-4.3E+09	-2.5E+09	-1.3E+09	-1.1E+10	-8.3E+09	-6.2E+09	-4.2E+09	-2.5E+09	-1.3E+09
	2400	balance below	-7.7E+09	-6.0E+09	-4.5E+09	-3.1E+09	-1.9E+09	-9.8E+08	-7.5E+09	-5.8E+09	-4.4E+09	-3.0E+09	-1.8E+09	-9.5E+08
	2340	cross section	-6.3E+09	-5.0E+09	-3.7E+09	-2.6E+09	-1.6E+09	-8.3E+08	-6.2E+09	-4.8E+09	-3.6E+09	-2.5E+09	-1.5E+09	-8.0E+08
Ice flow scenario	Cross Section (trapezoid)	Mass influx into cross section	DMM (Difference between mass influx and total mass balance below the cross section) Best Guess mass balance scenario						DMM (Difference between mass influx and total mass balance below the cross section) DDF -20% mass balance scenario					
Best Guess	2500	2.60E+09	-8.4E+09	-6.0E+09	-3.8E+09	-1.7E+09	5.9E+07	1.3E+09	-8.1E+09	-5.7E+09	-3.6E+09	-1.6E+09	1.2E+08	1.3E+09
	2400	3.22E+08	-7.4E+09	-5.7E+09	-4.2E+09	-2.8E+09	-1.5E+09	-6.6E+08	-7.2E+09	-5.5E+09	-4.0E+09	-2.7E+09	-1.5E+09	-6.3E+08
	2340	1.41E+08	-6.2E+09	-4.8E+09	-3.6E+09	-2.4E+09	-1.4E+09	-6.9E+08	-6.0E+09	-4.7E+09	-3.5E+09	-2.3E+09	-1.4E+09	-6.6E+08
flow parameters *2	2500	5.20E+09	-5.8E+09	-3.4E+09	-1.2E+09	8.9E+08	2.7E+09	3.9E+09	-5.5E+09	-3.1E+09	-9.8E+08	1.0E+09	2.7E+09	3.9E+09
	2400	6.43E+08	-7.0E+09	-5.4E+09	-3.9E+09	-2.5E+09	-1.2E+09	-3.4E+08	-6.8E+09	-5.2E+09	-3.7E+09	-2.4E+09	-1.2E+09	-3.1E+08
	2340	2.82E+08	-6.1E+09	-4.7E+09	-3.5E+09	-2.3E+09	-1.3E+09	-5.5E+08	-5.9E+09	-4.5E+09	-3.3E+09	-2.2E+09	-1.2E+09	-5.2E+08
flow parameters *4	2500	1.04E+10	-6.4E+08	1.8E+09	4.0E+09	6.1E+09	7.9E+09	9.1E+09	-3.5E+08	2.1E+09	4.2E+09	6.2E+09	7.9E+09	9.1E+09
	2400	1.29E+09	-6.4E+09	-4.8E+09	-3.2E+09	-1.8E+09	-5.9E+08	3.0E+08	-6.2E+09	-4.5E+09	-3.1E+09	-1.7E+09	-5.3E+08	3.4E+08
	2340	5.65E+08	-5.8E+09	-4.4E+09	-3.2E+09	-2.0E+09	-1.0E+09	-2.7E+08	-5.6E+09	-4.2E+09	-3.0E+09	-1.9E+09	-9.6E+08	-2.4E+08
slope = 0.12	2500	2.60E+09	-8.4E+09	-6.0E+09	-3.8E+09	-1.7E+09	5.9E+07	1.3E+09	-8.1E+09	-5.7E+09	-3.6E+09	-1.6E+09	1.2E+08	1.3E+09
	2400	9.14E+08	-6.8E+09	-5.1E+09	-3.6E+09	-2.2E+09	-9.6E+08	-7.0E+07	-6.6E+09	-4.9E+09	-3.4E+09	-2.1E+09	-9.1E+08	-3.5E+07
	2340	4.01E+08	-5.9E+09	-4.6E+09	-3.3E+09	-2.2E+09	-1.2E+09	-4.3E+08	-5.8E+09	-4.4E+09	-3.2E+09	-2.1E+09	-1.1E+09	-4.0E+08
F = 0.9	2500	6.76E+09	-4.3E+09	-1.9E+09	3.6E+08	2.4E+09	4.2E+09	5.4E+09	-4.0E+09	-1.6E+09	5.8E+08	2.6E+09	4.3E+09	5.5E+09
	2400	6.97E+08	-7.0E+09	-5.4E+09	-3.8E+09	-2.4E+09	-1.2E+09	-2.9E+08	-6.8E+09	-5.1E+09	-3.7E+09	-2.3E+09	-1.1E+09	-2.5E+08
	2340	2.74E+08	-6.1E+09	-4.7E+09	-3.5E+09	-2.3E+09	-1.3E+09	-5.6E+08	-5.9E+09	-4.5E+09	-3.3E+09	-2.2E+09	-1.3E+09	-5.3E+08

Declaration

under Art. 28 Para. 2 RSL 05

Last, first name: Wäger, Philippe

Matriculation number: 03-719-473

Programme: Master in Climate Sciences

Thesis title: Glacier-climate modeling in Las Leñas, Central Andes of Argentina

Thesis supervisor: Supervisor: Prof. Dr. Heinz Veit

Advisor: Dr. Christoph Kull

I hereby declare that this submission is my own work and that, to the best of my knowledge and belief, it contains no material previously published or written by another person, except where due acknowledgement has been made in the text. In accordance with academic rules and ethical conduct, I have fully cited and referenced all material and results that are not original to this work. I am well aware of the fact that, on the basis of Article 36 Paragraph 1 Letter o of the University Law of 5 September 1996, the Senate is entitled to deny the title awarded on the basis of this work if proven otherwise.

Bern, 27.9.2009

Place, date

.....

Signature